

**MOTION CONTROL, PLANNING AND  
MANIPULATION OF NANOWIRES UNDER  
ELECTRIC-FIELDS IN FLUID SUSPENSION**

**By  
KAIYAN YU**

**A dissertation submitted to the  
School of Graduate Studies  
Rutgers, The State University of New Jersey  
In partial fulfillment of the requirements  
For the degree of  
Doctor of Philosophy  
Graduate Program in Mechanical and Aerospace Engineering**

**Written under the direction of  
Jingang Yi**

**And approved by**

---

---

---

---

---

**New Brunswick, New Jersey**

**October, 2017**

**© 2017**

**Kaiyan Yu**

**ALL RIGHTS RESERVED**

## **ABSTRACT OF THE DISSERTATION**

# **Motion Control, Planning and Manipulation of Nanowires under Electric-Fields in Fluid Suspension**

**by KAIYAN YU**

**Dissertation Director:**

**Jingang Yi**

Automated manipulation of nanowires and nanotubes would enable the scalable manufacturing of nanodevices for a variety of applications. However, two fundamental challenges still remain: (i) placement of nanostructures such as nanowires or nanotubes in precise locations, and (ii) automated scalable characterization, manipulation and assembly of nanostructures into nanodevices. Overcoming these challenges could enable further potential capacities of assembling and manufacturing functional nanodevices. In this dissertation, we present an electric-field-based automated system to motion plan and control of individual and simultaneous multiple nanowires in liquid suspension with a simple, generic set of electrodes. The proposed robust motion control has been proved to be stable, and various motion planning algorithms significantly reduce the computational complexity while maintaining sub-optimal performance. Extensive experimental results confirm the analysis and the design of the nanowire motion control, planning, and manipulation scheme. Finally, we propose a fully automated procedure of solution based online characterization, manipulation, and assembly of nanowires.

Proof-of-concept silicon nanowire field-effect transistors (FETs) with selected electrical conductivities are fabricated and assembled using the proposed procedure. The device testing results confirm the feasibility and effectiveness of the intergraded scheme.

In order to address those fundamental challenges, in the first part of this dissertation, we summarize the lowest-order electric field induced forces acting on a particle in suspension and present a dynamic model of nanowires under electrophoretic force. We then propose a micro-fluidic device design that is actuated by a simple, scalable and generic set of electrodes to precisely generate controllable electric fields. With symmetric properties of the designed electrode arrays, a superposition approach is developed to efficiently compute electric-field distribution on the micro-fluidic device.

With the proper approach to actuate the motion of nanoparticles, in the second part, we propose a novel electric-field-based single-nanowire motion planning and control scheme. A vision-based motion control of nanowire in dilute suspension is designed to precisely control the motion of individual nanowires using the independently controlled electrode arrays. The motion planning of a nanowire from one position to the target location is NP-hard due to the nature of combinatorial optimization. Two heuristic algorithms are presented to generate sub-optimal motion trajectory. In addition, we demonstrate a single, integrated process to position, orient and deposit multiple nanowires sequentially onto the substrate of the microfluidic device.

In order to facilitate the manipulation and assembly, we introduce motion-planning and control algorithms for simultaneously steering multiple nanowires in the third part of the dissertation. A motion-control algorithm is presented to simultaneously steer multiple nanowires along different desired trajectories under controlled electrophoretic forces. We provide the control-system properties that capture the relationship between the maximum number of the simultaneously controllable nanowires and the given number of actuated electrodes. A two-stage motion-planning algorithm is then presented to generate the desired trajectories for multiple nanowires with minimum total traveling distances. We demonstrate the simultaneous motion control and planning of multiple

nanowires to form various geometric patterns and track different trajectories. However, the shortest distance trajectories do not result in the fastest manipulation. To improve the efficiency of the simultaneous manipulation and assembly of nanowires, we present online time-optimal motion-planning and control algorithms for effectively steering multiple nanowires simultaneously in liquid suspension. The motion planner, called SRRT\*, is an improved sparse structure Rapidly-exploring Random Tree Star (RRT\*)-based motion-planning algorithm. The SRRT\* guarantees the asymptotically near time-optimal trajectories of multiple nanowires. Moreover, unlike the two-stage algorithm, the maximum number of nanowires that can be simultaneously controlled is not restricted explicitly. All of the above-mentioned motion control and planning strategies are validated through extensive experiments and simulations.

In the last part of the dissertation, we propose an integrated procedure of online automated characterization, manipulation, and assembly of nanowires to build functional nanodevices. Particularly, we separate and assemble silicon nanowires according to their electrical conductivities into FETs. The characteristic measurements of the FETs confirm the feasibility and effectiveness of the integrated characterization, manipulation and assembly procedure. The discussion of future research directions is also included at the end of the dissertation.

## **Acknowledgements**

Firstly, I would like to express my deepest gratitude and appreciation to my advisor Prof. Jingang Yi for all of his support, encouragement, and guidance. He has helped me with numerous advice, patience, motivation, and immense knowledge in shaping my research and technical skills as a graduate student, as well as my skills and attitudes for my future career. I am deeply grateful to him for all his efforts, help and suggestions to encourage me to pursue a career in academia. His enthusiasm and love for research and teaching are contagious. Also, his insightful comments and constructive criticisms at different stages of my doctoral studies were thought-provoking and they helped me formulate and develop my ideas. I am grateful to him for holding me to a high research standard and teaching me how to conduct innovative research. I have been amazingly fortunate to have an advisor who supported me technically, emotionally and spiritually throughout my years study at Rutgers, and also provided me with the guidance to overcome many difficulties when my steps faltered.

My co-advisor, Prof. Jerry W. Shan, has been always there to listen and give me advice. I am sincerely thankful to him for inspiring me to think critically and conduct rigorous experiments. I am also grateful to him for all the encouragement and practical advice, as well as helpful suggestions on my career development. I am indebted to him for his continuous guidance and carefully reading and commenting on countless revisions of my writings, commenting on my views and helping me understand and enrich research ideas.

Thanks also go to my committee members Prof. Qingze Zou, Prof. Kostas Bekris, and Prof. Yicheng Lu for thoroughly reviewing my dissertation and providing their feedback with constructive comments and suggestions. I am also grateful to all my

labmates at Robotics, Automation and Mechatronics Laboratory, including Pengheng Wang, Kuo Chen, Mitja Trkov, Aliasghar Arab, Yizhai Zhang, Fei Liu and others for all helpful discussions and sharing their knowledge throughout years at Rutgers. Special thanks go to Xin Liu, Jack Zheng, Joseph Sherba and Prof. Jeff Zahn in the Department of Biomedical Engineering, Cevat Akin, Rick Castellano, Wuhan Yuan and Gabriel Giraldo in the Department of Mechanical and Aerospace Engineering, Wen-Chiang Hong, Guangyuan Li and Yuxuan Li in the Department of Electrical and Computer Engineering of Rutgers University, and Xiang Lu of Nankai University in China, with all of whom I had a chance to collaborate closely and have unselfishly shared their knowledge, helps and experiences that has helped me to expand my research and improve my ideas.

Most importantly, none of this would have been possible without the love and patience of my parents. My parents to whom this dissertation is dedicated to, have been a constant source of love, concern, support, and strength all these years. I would like to express my heartfelt gratitude to my parents, and warmly appreciate the generosity and understanding of my parents.

Finally, I appreciate the financial support from the Chinese Scholarship Council (CSC) that partially supported my doctoral research at Rutgers University.

## **Dedication**

*This dissertation is dedicated to my beloved parents.*



# Table of Contents

<b>Abstract</b> . . . . .	ii
<b>Acknowledgements</b> . . . . .	v
<b>Dedication</b> . . . . .	vii
<b>List of Tables</b> . . . . .	xii
<b>List of Figures</b> . . . . .	xiii
<b>1. Introduction</b> . . . . .	1
1.1. Motivation . . . . .	1
1.2. Background . . . . .	4
1.2.1. Nanomanipulation . . . . .	5
1.2.2. Electric-field based nanomanipulation . . . . .	6
1.2.2.1. EP based nanomanipulation . . . . .	7
1.2.2.2. DEP based nanomanipulation . . . . .	7
1.2.2.3. EO based nanomanipulation . . . . .	8
1.2.3. Motion planning of nanowires . . . . .	9
1.3. Dissertation outline and contributions . . . . .	12
<b>2. Electric-Field Based Nanowire Manipulation Modeling and Configuration</b>	17
2.1. Introduction . . . . .	17
2.2. System configuration . . . . .	17
2.3. EP-based nanowire motion model . . . . .	20
2.4. Electric-field modeling . . . . .	21

2.5. Conclusion . . . . .	24
<b>3. Motion Control, Planning and Manipulation of Individual Nanowires under Electric-Fields in Fluid Suspension . . . . .</b>	<b>25</b>
3.1. Introduction . . . . .	25
3.2. Problem formulation . . . . .	26
3.3. Nanowire motion control . . . . .	27
3.4. EP-based nanowire motion planning . . . . .	30
3.4.1. Optimal trajectory property . . . . .	30
3.4.2. Motion-planning algorithms . . . . .	35
3.4.2.1. Heuristic algorithm – AllPower . . . . .	35
3.4.2.2. Heuristic algorithm – MinCost . . . . .	36
3.4.2.3. $A^*$ pruning . . . . .	36
3.4.2.4. Breadth-first search (BFS)-based planning . . . . .	37
3.4.2.5. RRT pruning . . . . .	37
3.5. Experimental results . . . . .	37
3.5.1. Experimental setup . . . . .	37
3.5.2. Nanowire motion-control results . . . . .	40
3.5.3. Motion-planning results . . . . .	42
3.5.4. Steering and manipulating nanowires . . . . .	46
3.6. Conclusion . . . . .	49
<b>4. Simultaneous Multiple-Nanowire Motion Control, Minimum Distance Planning and Manipulation under Electric-Fields in Fluid Suspension . . . . .</b>	<b>51</b>
4.1. Introduction . . . . .	51
4.2. Problem formulation . . . . .	52
4.3. Motion control of multiple nanowires . . . . .	54
4.4. Multiple nanowire motion planning . . . . .	60

4.4.1.	First-stage planning . . . . .	61
4.4.2.	Second stage planning . . . . .	64
4.5.	Simulation and experimental results . . . . .	65
4.5.1.	Simulation results . . . . .	66
4.5.2.	Experimental results . . . . .	71
4.6.	Conclusion . . . . .	76
<b>5.</b>	<b>Time-Optimal Simultaneous Motion Planning and Manipulation of Multiple Nanowires under Electric-Fields in Fluid Suspension . . . . .</b>	<b>77</b>
5.1.	Introduction . . . . .	77
5.2.	Problem formulation . . . . .	78
5.3.	Motion control of multiple nanowires . . . . .	79
5.4.	Multiple nanowire motion planning . . . . .	81
5.4.1.	Roadmap formulation . . . . .	81
5.4.2.	The SRRT* algorithm . . . . .	82
5.4.3.	Heuristic sampling . . . . .	84
5.4.4.	Steering and rewiring . . . . .	85
5.5.	Simulation and experimental results . . . . .	87
5.5.1.	Simulation results . . . . .	88
5.5.2.	Experimental results . . . . .	91
5.6.	Conclusion and future work . . . . .	94
<b>6.</b>	<b>Automated Characterization, Manipulation, and Assembly of Nanowires . . . . .</b>	<b>96</b>
6.1.	Introduction . . . . .	96
6.2.	Automated characterization of multiple nanowires using electro-orientation spectroscopy . . . . .	99
6.2.1.	Contactless and solution-based EOS (CS-EOS) . . . . .	100
6.2.2.	Simultaneous multiple-nanowire CS-EOS . . . . .	101

6.3. Automated characterization, manipulation, and assembly of nanowires (ACMAN) . . . . .	103
6.4. Automated assembly of SiNW-based FETs using ACMAN . . . . .	106
6.4.1. Microfluidic device and SiNW FET fabrication . . . . .	107
6.4.2. Characteristics and performance of assembled SiNW FETs . .	112
6.5. Summary . . . . .	123
<b>7. Conclusions and Future Work . . . . .</b>	<b>124</b>
7.1. Conclusions . . . . .	124
7.2. Future work . . . . .	127
<b>References . . . . .</b>	<b>130</b>

## **List of Tables**

3.1. Performance comparisons for the example shown in Figure 3.9 . . . .	44
5.1. Traveling time (s) comparison between the SRRT* and TwoStage algorithms. . . . .	93
6.1. Performance comparisons for the FETs fabricated using the ACMAN process and DEP only method. . . . .	122

## List of Figures

1.1.	Nanowire based functional nanodevices. (a) Nanowire based functional logic gate; a logic AND gate is shown as an example [40]; the scale bar is 1 $\mu\text{m}$ . (b) An all-optical nanowire NAND gate; the scale bar is 5 $\mu\text{m}$ [41]. (c) Figure A shows a silicon nanowire (SiNW) based field-effect transistor (FET) with metal source and drain electrodes on the surface of $\text{SiO}_2/\text{Si}$ substrate. (inset) High-resolution transmission electron micrograph of a 5 nm-diameter SiNW; the scale bar is 5 nm. Figure B shows scanning electron micrograph of a SiNW FET device; the scale bar is 500 nm [42]. (d) Contact length scaling of molybdenum end-contacted quasiballistic single-walled carbon nanotube transistors [43]. (e) A rotating nanowire based nanomotor powered by a rotating electrical field [1]. (f) Delivery of functional tumor necrosis factor alpha ( $\text{TNF}\alpha$ ) by nanowires. Two $\text{TNF}\alpha$ -coated nanowires that contact and stimulate the wild-type HeLa cell (left); Nanowire delivery to pre-selected cells, and the overlay of a time series of phase contrast images showing delivery of a single nanowire to the cell; the scale bar is 20 $\mu\text{m}$ [44] (right). . . . .	2
2.1.	Schematic of microfluidic device with $N \times N$ electrodes. (a) 3D view of micro-fluidic device with $N \times N$ independently actuated electrodes on a bottom substrate, with a common top electrode. (b) Top view of the motion trajectories of nanowires induced by the electrode array. . . . .	18
2.2.	A schematic of an electric-field-based nanowires motion control, planning and manipulation scheme. . . . .	18

2.3.	Prolate spheroid nanowire with major radius $a$ and minor radius $b$ . . .	20
2.4.	(a) A schematic of an atomic and basic areas around nanowire $P$ . (b) An illustrative schematic diagram to compute the electric field by turning on one electrode. . . . .	22
3.1.	Illustrative schematic of the trajectory search area. . . . .	32
3.2.	Schematic of time-equivalent trajectory within $\mathcal{A}_m$ . (a) Vertex $B$ with 135-deg inner angle. (b) Vertex $B$ with 90-deg inner angle. (c) Vertex $B$ with 45-deg inner angle. . . . .	33
3.3.	The experimental setup. (a) The inverted microscope setup with em- bedded control systems and vision-based nanowire motion feedback. (b) The glass microfluidic device is mounted on a PCB for testing and a top coverslip coated with an indium tin oxide (ITO) layer is placed to cover the device. (c) The top view of the microfluidic device with $2 \times 3$ electrode arrays. . . . .	38
3.4.	(a) SEM image of as-grown silicon nanowires used in experiments. (b) The nanowire image under microscope and the processed contour for positioning feedback. . . . .	39
3.5.	Comparison of estimated and measured values of zeta-potential among a total of 35 silicon nanowires. . . . .	39
3.6.	Trajectory tracking performance. (a) EP model-based nanowire mo- tion control of a straight-line trajectory without disturbance compensa- tion. (b) Disturbance-compensated following a straight-line path. (c) Disturbance-compensated following a circular path. (d) Disturbance- compensated following an “R”-shape path. In all plots, the triangular and empty circular marks indicate the starting and ending points, re- spectively, of the nanowire trajectory. . . . .	40
3.7.	Trajectory-tracking errors. (a) Errors for a straight-line trajectory. (b) Errors for a circular trajectory. (c) Errors for an “R”-shape trajectory. .	41

3.8. Performance comparison among various motion planning algorithms on an $N \times N$ electrode array. (a) Computation time (mean and standard derivation). (b) Nanowire travel time. (c) RMSE (benchmarked with the BFS results). . . . .	42
3.9. Comparison of the nanowire trajectories under different motion planning algorithms using a $4 \times 4$ electrode array. . . . .	44
3.10. Experimental silicon nanowire trajectories under BFS and AllPower. Note that the straight-line trajectories shown for comparison is not the minimum-time trajectory. . . . .	45
3.11. (a) Velocity profiles corresponding to the ALLPOWER and the straight-line trajectories. (b) Normalized distance from target point corresponding to the ALLPOWER and the straight-line trajectories. . . . .	46
3.12. Vertical positioning and deposition of a single nanowire on the device substrate. (a) nanowire at location <i>A</i> . (b) Nanowire is steered to location <i>B</i> by AllPower algorithm. (c) Using the top ITO electrode, the nanowire was aligned along the vertical direction and steered to touch the bottom surface. (d) By turning the electrode again, the nanowire was re-orient and deposited on the substrate surface with the desired orientation. (e) Overlay trajectory of the entire nanowire motion. The triangular and empty circular marks indicate the starting and ending points of the nanowire. . . . .	47
3.13. Electric-field-based steering and manipulation of three nanowires to form a straight-line on the device substrate. (a) Initial positions of the three nanowires. (b) Final positions of these three nanowires after re-positioning and depositing to align into a straight-line. . . . .	48
3.14. Electric-field-based steering and manipulation of multiple nanowires to form (a) a straight-line, (b) hexagonal and (c) three cross-shape patterns on the device substrate. . . . .	49



4.1.	A schematic of an atomic and basic areas around nanowire $P_i$ with a re-indexed electrode order (as one-dimensional array). . . . .	54
4.2.	Schematic of the capacity $U_{ij}$ calculation and <i>CoverCell</i> $\mathcal{C}_{cov}$ illustration as the shaded cells across $\overline{\mathcal{ST}}$ . . . . .	63
4.3.	(a) Simultaneous motion control of 8 nanowires to form an RU trajectory in the presence of random fluid disturbances. The total travelling time is 26 s. (b) Simultaneous motion control of 3 nanowires to track a circular shape trajectory. The total travelling time is 877 s. The “*” markers indicate the position of the random starting points, the “▷” and “○” markers are the starting and ending points of each trajectory segment, respectively. The solid lines are the actual trajectories and the dashed lines are the desired trajectories. . . . .	67
4.4.	(a) Motion planning and control of 10 nanowires simultaneously to form an equally spaced crossed-line trajectory. The total travelling time is 664.5 s. (b) Simultaneously direct motion control of 10 nanowires try to form the same cross line trajectory as (a) without motion planning and path tracking, but fail due to collision. The total travelling time is 111.4 s. The “*” markers indicate the position of the random starting points and the “○” markers are the ending points of each desired trajectory segment. The solid lines represent the actual trajectories and the dashed lines are the desired trajectories. . . . .	68
4.5.	Simulation of simultaneous motion planning and control of different numbers of nanowires. (a) 18 nanowires in a $6 \times 6$ electrode array with the total travelling time 858 s. (b) 30 nanowires in a $8 \times 8$ electrode array with the total travelling time 1386 s. (c) 40 nanowires in a $9 \times 9$ electrode array with the total travelling time 1826 s. . . . .	69

4.6.	Run-time comparison between the TwoStage and the RRT* algorithms with different numbers of nanowires in a $6 \times 6$ electrode array. The numbers on each data point show the success rates for both the TwoStage and the RRT* algorithms. The last five data points for the RRT* algorithm are clamped to $10^4$ s due to reaching the maximum running time limit. . . . .	70
4.7.	Comparison of the maximum number of nanowires that can be simultaneously controlled in different numbers of atomic cells between the original electric field and SVD-truncated electrical field. . . . .	70
4.8.	(a) The micro-fluidic device mounted on a PCB testing board. (b) The top view of the micro-fluidic device with $4 \times 4$ electrode arrays. . . .	71
4.9.	(a) A schematic of the geometry design of the micro-fluid reservoir. The shaded areas show the common electrical ground on the bottom substrate. (b) Sample electric-field distribution when a voltage with a magnitude of 10 V is applied to only one electrode marked as the red color and other electrodes are grounded. The red arrows show the direction of the electric field and the color legend shows the magnitude of the electric field. . . . .	71
4.10.	Overlaid nanowire trajectories to form different geometric patterns. All pictures are obtained by taking and overlaying the nanowire images at a series of time snapshots. All background images are removed to clearly present the nanowire trajectories. The “▷” and “○” marks indicate the nanowires’ initial and final positions, respectively. (a) A straight-line with the total travelling time 66.3 s. (b) A square with the total travelling time 222 s. c) A circle with one nanowire at the center with the total travelling time 338.6 s. (d) Simultaneous tracking control of three nanowires to form a circle. The total travelling time is 253 s. (e) An equilateral triangle with the total traveling time 172.4 s. . . . .	72

4.11. Motion planning and control for three nanowires simultaneously guided from three different initial atomic cells to form an equally spaced horizontal line. The total travelling time is 1086.1 s. The “▷” and “◦” marks indicate the nanowires’ initial and final positions, respectively. .	75
4.12. Overlaid nanowire trajectories and formation control of three nanowires without compensation for EO background flow. The total travelling time is 401.7 s. . . . .	75
5.1. An example of Best_Near parent node selection and drain pruning. A tree structure with witness area $\mathcal{B}_1(\mathbf{q}, \delta_s)$ is centered at the yellow dot with grid length $\delta_s$ . The nodes of the tree are the shadowed dots (blue, grey and red dots), and the arrow lines indicate the tree edges. The blue dots are witnesses, the grey dot is the inactive node, and the red dots show the nodes that are pruned in drain. All nodes $\mathbf{q} \in \mathcal{B}_2(\mathbf{q}_{\text{rand}}, \delta_{bn})$ and $\mathbf{q} \in V_{\text{act}}$ are checked to find $\mathbf{q}_{\text{parent}}$ , which node has the lowest-cost ( $2\Delta t$ ) from root $\mathcal{S}$ . After steering from $\mathbf{q}_{\text{parent}}$ , a new state $\mathbf{q}_{\text{new}}$ is added into tree with cost $6\Delta t$ . A feasible solution is also generated and <i>MinCost</i> is updated as $6\Delta t$ . Any leaf node is iteratively pruned along the tree path until reaching any witness node with cost less than <i>MinCost</i> . In this case, the red nodes, the grey node and the dashed edges are removed. . . . .	84
5.2. Run-time comparison among SRRT*, TwoStage and RRT* with different numbers of nanowires in a $6 \times 6$ electrode array. The last five data points for the RRT* algorithm are clamped to $10^4$ s due to reaching the maximum computation time limit. . . . .	89
5.3. Travel-time comparison among the minimum-time RRT* algorithm, the SRRT* algorithm, and the TwoStage algorithms with different numbers of nanowires in a $6 \times 6$ electrode array. . . . .	90

5.4.	Simulated trajectories for motion-planning and control of (a) 4 nanowires in opposite target directions, (b) 8 nanowires in twisted target directions, and (c) 9 nanowires from one atomic cell to different target directions. The “*” and “o” markers indicate the nanowires initial and final positions, respectively. . . . .	91
5.5.	Experimental comparison between SRRT* and TwoStage trajectories for motion planning and control of one nanowire crossing an atomic-cell boundary. The overlaid nanowire trajectories are obtained by using SRRT* algorithm and overlaying the nanowire images evenly spaced every 5 seconds. The total traveling times are (a) SRRT* : 40.8s and shortest path: 157.2s. (b) SRRT* : 137.2s and shortest path: 345.7s. (c) SRRT* : 89.1s and shortest path: 158.7s. The “▷” and “o” marks indicate the nanowires’ initial and final positions, respectively. . . . .	92
5.6.	Experimental motion-trajectory comparison between the SRRT* and TwoStage planners for steering two nanowires simultaneously from the same initial and ending locations. The overlaid nanowire trajectories are obtained by using SRRT* algorithm and overlaying the nanowire images evenly spaced every 1 seconds, and the TwoStage trajectories are marked evenly spaced every 10 seconds. The “▷” and “o” marks indicate the nanowires’ initial and final positions, respectively. . . . .	94

6.1.	The schematic for automated characterization, manipulation, and assembly of SiNWs into FETs with different electric properties. First, nanowires are steered from their starting location to the characterization region (a $150\text{ }\mu\text{m} \times 150\text{ }\mu\text{m}$ square region in the center marked by the red dash line). Simultaneous multiple-nanowire CS-EOS is used to measure the electrical conductivities of multiple nanowires in the characterization region. Meanwhile, the motion control, planning, and manipulation of nanowires strategies are used to keep the targeted nanowires inside the characterization region with uniform AC electric field. After characterization, those nanowires are separated according to their conductivities, driven to the assembly areas (blue dash line), and finally deposited between the source and drain electrodes to form FET nanodevices. . . . .	104
6.2.	Fabrication schematic of the SiNW-based bottom-gate FET using photolithography process. . . . .	107
6.3.	Overlaid nanowire trajectories for simultaneously automated characterization, manipulation, and assembly of two SiNWs by their electrical conductivities. The less conductive SiNW ( $\sigma_{LC} = 0.045\text{ S/m}$ ) is placed between the right pair of contact electrodes, while the higher conductive SiNW ( $\sigma_{HC} \geq 0.46\text{ S/m}$ ) is placed between the left pair of contact electrodes. The star and ellipse marks represent the starting and target locations of each nanowire. The figure shows overlaid center-of-mass trajectories of the two simultaneous nanowires. . . . .	110
6.4.	Measured alignment rates of two simultaneous SiNWs in Figure 6.3 with respect to applied electric field frequency. The solid lines are curve fit of the form $\Omega = 1/[1 + (\omega/\omega_c)^2]$ , from which the crossover frequency and hence the nanowire conductivity can be extracted. . . .	111

6.5. Overlaid nanowire motion trajectories in the automated characterization, manipulation, and assembly of SiNWs as thin-film FETs. Less conductive SiNWs ( $\sigma_p < 0.2$ S/m) are placed between the right pair of contact electrodes, while higher conductive SiNWs ( $\sigma_p \geq 0.2$ S/m) are placed between the left pair of contact electrodes. The star and ellipse marks represent the starting and target locations of each nanowire. The figure shows overlaid trajectories of the center of mass of 14 nanowires and their deposit locations. . . . .	112
6.6. Device Charact. 1: A proof-of-concept demonstration of the integrated automated characterization, manipulation, and assembly of 24 SiNWs as FET devices. 12 nanowires (NWs) were characterized and deposited on each side. After the wrap-around electrode fabrication, the resulting FETs have 10 NWs on each side, showing N-type characteristics. (a) Transfer characteristics in logarithmic scale showing the drain current per nanowire at source-to-drain voltage $V_{DS} = 1$ V for the two N type FETs after separation. (inset) The transfer characteristics in linear scale. (b) Measured conductivity distribution against the number of characterized nanowires by CS-EOS. (c) Output characteristics of the FETs showing the drain current per nanowire in less conductive side at gate voltage $V_G = 0$ to 20 V in 5 V steps. (d) Output characteristics of the FETs showing the drain current per nanowire in conductive side at $V_G = 0$ to 20 V in 5 V steps. . . . .	114

6.7. Device Charact. 2: A proof-of-concept demonstration of the integrated automated characterization, manipulation, and assembly of 16 SiNWs as FET devices. 8 NWs were characterized and deposited on each side. After the wrap-around electrode fabrication, the resulting FETs have 3 NWs on each side. The FET assembled with less conductive SiNWs shows P-type characteristics while the FET assembled with conductive SiNWs shows N-type characteristics. (a) Transfer characteristics in logarithmic scale showing the drain current per nanowire at $V_{DS} = 1$ V for the P type and N type FETs after separation. (inset) The transfer characteristics in linear scale. (b) Measured conductivity distribution against the number of characterized nanowires by CS-EOS. (c) Output characteristics of the FETs showing the drain current per nanowire in less conductive side at $V_G = 0$ to $-20$ V. (d) Output characteristics of the FETs showing the drain current per nanowire in conductive side at $V_G = 0$ to $20$ V. . . . .	115
---	-----

- 6.8. Device Charact. 3: A proof-of-concept demonstration of the integrated automated characterization, manipulation, and assembly of 20 SiNWs as FET devices. 10 NWs were characterized and deposited on each side. After the wrap-around electrode fabrication, the resulting FETs have 3 NWs on each side. The FET assembled with less conductive SiNWs shows P-type characteristics while the FET assembled with conductive SiNWs shows N-type characteristics. (a) Transfer characteristics in logarithmic scale showing the drain current per nanowire at  $V_{DS} = 1$  V for the P type and N type FETs after separation. (inset) The transfer characteristics in linear scale. (b) Measured conductivity distribution against the number of characterized nanowires by CS-EOS. (c) Output characteristics of the FETs showing the drain current per nanowire in less conductive side at  $V_G = 0$  to  $-25$  V in  $-5$  V steps. (d) Output characteristics of the FETs showing the drain current per nanowire in conductive side at  $V_G = 0$  to  $25$  V in  $5$  V steps. . . . . 117
- 6.9. Device Charact. 4: A proof-of-concept demonstration of the integrated automated characterization, manipulation, and assembly of 20 SiNWs as FET devices. 10 NWs were characterized and deposited on each side. After the wrap-around electrode fabrication, 9 NWs remain on the less-conductive-side FET, and the conductive-side FET has 7 NWs left, both showing N-type characteristics. (a) Transfer characteristics in logarithmic scale showing the drain current per nanowire at  $V_{DS} = 1$  V for the two N type FETs after separation. (inset) The transfer characteristics in linear scale. (b) Measured conductivity distribution against the number of characterized nanowires by CS-EOS. . . . . 118



6.10. Device DEP only: SiNWs were collected at different DEP frequencies. 2 MHz and 20 kHz frequencies and 50 V <sub>peak-to-peak</sub> AC fields are used to fabricate the conductive and less conductive FETs, respectively, which are the same fields as used in the deposition step to trap nanowires for Device Charact. 1 to 4 in the ACMAN scheme. After the wrapping electrode fabrication, the resulting DEP only FETs have 3 NWs on each side, both showing P-type characteristics. . . . .	119
6.11. Graphical presentation of the sub-threshold swing (s-s), on/off current ( $I_{ON/OFF}$ ) and transconductance $g_m$ using the less conductive FET measurement data of Device Charact. 3 as shown in Figure 6.8(a). . . . .	119
6.12. The on-current (the absolute value $ I_{on} $ ) comparison of the FET Devices Charact. 1 to 4. and the DEP only assembled devices. . . . .	120
6.13. The sub-threshold swing (s-s) and traps density ( $N_{trap}$ ) for Device Charact. 1 to 4 and the DEP only assembled devices. The transfer characteristics of the SiNW FETs shown in Figures 6.6 (a) to 6.9 (a) and 6.10 are used for the extraction of s-s of the assembled devices, respectively.	121
6.14. Mobility comparison for Device Charact. 1 to 4 and the DEP only assembled devices. . . . .	121
7.1. Schematic of the patterned micro/nano-tubes based axonal guidance. .	129

# Chapter 1

## Introduction

### 1.1 Motivation

A wide variety of nanoscale materials with well-defined geometry have been explored in recent years for their unique and often enhanced properties [1]. One-dimensional (1D) nano-materials, i.e., large-aspect-ratio nano-materials such as nanowires, nanotubes, and nanorods, have attracted increasing interests for the past two decades due to the numerous potentials offered by their nanoscale sizes and various physical properties. 1D nano-materials have the properties of small diameters, large surface areas, as well as smooth surfaces, and those factors result in a large variety of novel functional properties [2]. Especially, extensive work has shown that nanowires or nanotubes can display unique electronic [3–11], optical [12, 13], thermophysical [14–16], magnetic [17, 18], and mechanical properties [19–23]. Nanowires based functional nanodevices have been numerous investigated, including nanowire based functional electronics [24–26], optoelectronics [27], photonics [28, 29], batteries [30–32], solar-cells [33–35], chemical/biological/biomedical sensors [36–39] and many other applications.

Figure 1.1 illustrates a few example of nanowire based functional nanodevices. Figure 1.1(a) shows a logic AND gate as an example of nanowire based functional logic circuits [40], while an all-optical nanowire NAND gate is shown in Figure 1.1(b) [41]. Figure 1.1(c) shows a silicon nanowire (SiNW) based field-effect transistor (FET) with metal source and drain electrodes on  $\text{SiO}_2/\text{Si}$  substrate [42]. A contact length scaling of molybdenum (Mo) end-contacted quasiballistic single-walled carbon nanotube

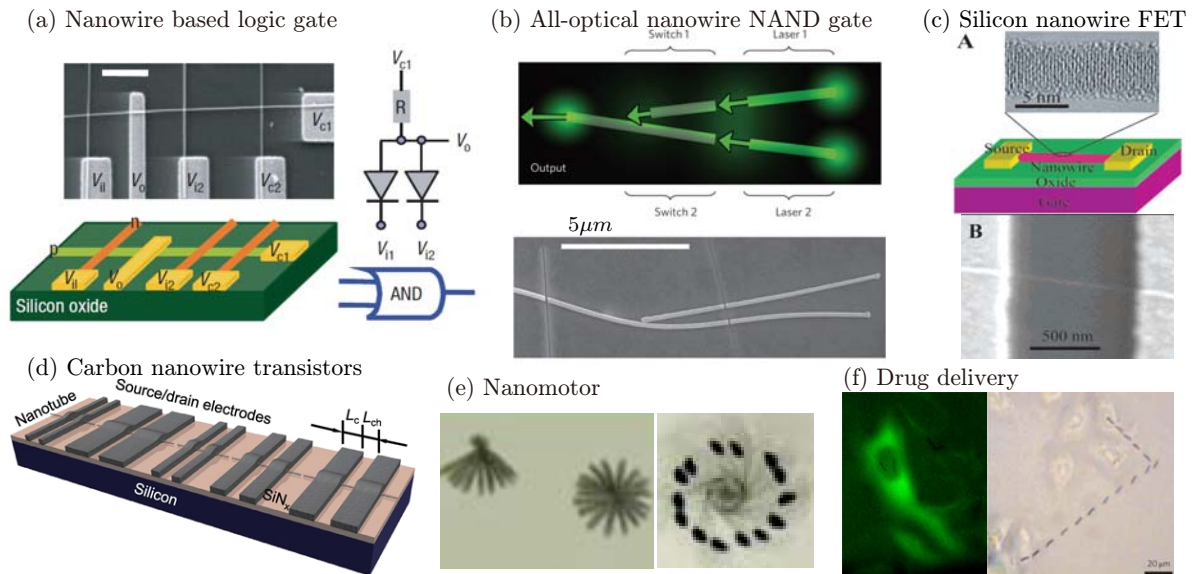


Figure 1.1: Nanowire based functional nanodevices. (a) Nanowire based functional logic gate; a logic AND gate is shown as an example [40]; the scale bar is  $1 \mu\text{m}$ . (b) An all-optical nanowire NAND gate; the scale bar is  $5 \mu\text{m}$  [41]. (c) Figure A shows a silicon nanowire (SiNW) based field-effect transistor (FET) with metal source and drain electrodes on the surface of  $\text{SiO}_2/\text{Si}$  substrate. (inset) High-resolution transmission electron micrograph of a 5 nm-diameter SiNW; the scale bar is 5 nm. Figure B shows scanning electron micrograph of a SiNW FET device; the scale bar is 500 nm [42]. (d) Contact length scaling of molybdenum end-contacted quasiballistic single-walled carbon nanotube transistors [43]. (e) A rotating nanowire based nanomotor powered by a rotating electrical field [1]. (f) Delivery of functional tumor necrosis factor alpha ( $\text{TNF}\alpha$ ) by nanowires. Two  $\text{TNF}\alpha$ -coated nanowires that contact and stimulate the wild-type HeLa cell (left); Nanowire delivery to pre-selected cells, and the overlay of a time series of phase contrast images showing delivery of a single nanowire to the cell; the scale bar is  $20 \mu\text{m}$  [44] (right).

transistor [43] is sketched in Figure 1.1(d). These nanoelectronics reduce size and scale of conventional electronics, and demonstrate advanced properties such as high performance, high sensitivity and high energy-efficiency etc. Mechanical functional nanodevices such as nanomotors and nanorotors are shown in Figure 1.1(e), which are based on a rotating nanowire powered by a rotating electrical field [1]. A further improved high-performing nanomotor was reported in [45]. Those nanomotors are more durable, reliable, and capable of ultra-high-speed rotation, as well as being able to fit inside a human cell to release drugs as a potential drug-delivery tool. Furthermore

in biomedical applications, Figure 1.1(f) shows the drug delivery of functional tumor necrosis factor alpha ( $\text{TNF}\alpha$ ) by nanowires. The left figure shows two  $\text{TNF}\alpha$ -coated nanowires that contact and stimulate the wild-type HeLa cell, and the right figure overlays a time series of phase contrast images showing nanowire delivery to pre-selected cells [44].

In order to fulfill those promising capabilities of 1D nano-materials, various techniques were developed for manufacturing functional nanodevices. The fabrication of those devices can be categorized into top-down, bottom-up, and nanomanipulation-enabled techniques [46, 47]. The top-down approaches [48], such as advanced nanolithographic techniques [49], were used to fabricate nanowires and nanotubes into nanodevices, but fabrication processes of these techniques are slow and costly [50]. Bottom-up methods typically employ self-assembly, chemical synthesis or super-molecule techniques [51]. Especially, chemical synthesis such as vapor-liquid-solid (VLS) technique and chemical vapor deposition (CVD) are widely utilized to generate functional nanodevices [52]. However, large scale chemical synthesis methods yield contaminants and defects, which have huge influence on the properties and functionalities of the nanodevices. Also, those techniques are laborious, costly, and often require thermal annealing and/or chemical treatments for chemical removal [53], which cause the assembly procedures inefficient and expensive. Nanomanipulation is a complementary technique that enables flexible maneuvering and precise positioning of nanostructures for nano-device assembly; it is particularly suitable for device prototyping and property tuning [54].

To fully realize aforementioned numerous potential of functional nanodevices, it is desirable to have automated methods to manipulate/assemble nanowires or nanotubes into nanodevices with controlled orientations at specific spatial locations. However, the automated scalable manipulation and assembly of nanowires or nanotubes is still a largely unmet fundamental challenge [55–61]. The difficulties mainly lie in twofold:

(i) the placement of nanostructures, such as nanowires or nanotubes, in precise locations for functional devices, interconnects, and other electronically useful components and (ii) the automated characterization, scalable manipulation and assembly occurred in electronic, mechanical and biochemical applications. Overcoming the automated nanomanipulation challenges could give rise to additional potential capacities of scalable assembling and manufacturing functional nanodevices for a large variety of applications, such as nanoelectronics assembly, nano-neuron interface, cell characterization and sorting, and the probing the responses of individual cells to mechanical and biochemical stimuli.

The goal of this dissertation is to address the above-mentioned challenges with four intertwined research aspects. More specifically, the dissertation focuses on: (i) analyzing and modeling the nanowire motion in dilute suspension with a simple, generic set of controllable electrodes, (ii) motion control, planning, and manipulation of individual nanowires under electric-fields in fluid suspension, (iii) simultaneous multiple-nanowire motion control, planning, and manipulation under electric-fields in fluid suspension, and (iv) integrating automated characterization, manipulation, and assembly of nanowires to build functional nanodevices, especially towards nano-electrical and biomedical applications. Although we discuss the manipulation of nanowires in the dissertation, the developed planning and control methods can be generalized to other 1D nano-materials.

## **1.2 Background**

In Section 1.1, we summarize the significance and challenge of the automated manipulation of nanowires. In this section, the approaches of nanomanipulation is first discussed. Then we introduce the advantages of electric-field based nanomanipulation. Next, we further explain the reason why electrophoresis is chosen as actuation to

manipulate the motion of nanowire in fluid suspension. Although we utilize the electrophoretic force to actuate the nanoparticles, the proposed nanomanipulation (motion planning and motion control) strategies are not limited to the actuation and can be generalized to other field-based applications.

### 1.2.1 Nanomanipulation

Nanomanipulation refers to the positional control of nanoparticles, and it is a key enabling technique for nanotechnology by filling the gap between the top-down and bottom-up strategies [62]. Nano-manipulation can be applied to the scientific exploration of mesoscopic phenomena and the construction of prototype nano devices and nano blocks [63]. It becomes a key instrument for technology bridging between sub-nano and mesoscale. Nanomanipulation techniques have gone through several phases to be used in scientific explorations, not only to reveal characteristics of nano, micro, and mesoscopic phenomena but also to build functional nanodevices useful for specific applications [64].

Atomic force microscope (AFM), transmission electron microscope (TEM), scanning tunneling microscope (STM), scanning electron microscope (SEM) or near-field scanning optical microscope (NSOM) are commonly used in nanomanipulation. However, those nanomanipulation techniques have several drawbacks, such as complex procedures, need of the assistance of human operators, and high cost. Non-contact actuation instead has been proved to be a promising solution to position micro- and nano-scale objects. The commonly used non-contact actuation techniques include magnetic actuation, electrical field actuation, optical tweezers, etc. Manipulation via actuated flows is also an alternative approach, such as electroosmosis, micromechanical, electrohydrodynamics, thermocapillary pumping, etc.

Optical tweezers [65] and magnetic tweezers [66–68] were invented and widely discussed to hold certain nanoparticles in recent years. The optical tweezers use the pressure radiation of the light to move objects. Besides costly, the short-range laser

force and therefore a limited manipulation range are particularity disadvantages of the optical tweezers actuation principle. Also, the motion of nanoparticles are controlled sequentially, and thus simultaneously nanomanipulation is difficult to be accomplished with limited number of laser spots. The magnetic tweezers rely on magnetic field gradient to hold a paramagnetic particle. Both optical and magnetic tweezers require extensive instrumentation. Particularly, if a particle is trapped in the optical or magnetic field, the field movement is achieved by mechanically moving the stage. Alternatively, the electric tweezers could apply a force to manipulate nanoparticles in suspension versatily without moving parts mechanically [1]. This dissertation will focus on electric-field based manipulation that does not have these disadvantages.

### **1.2.2 Electric-field based nanomanipulation**

Under electric fields in fluid suspension, a variety of phenomena, including electrophoresis (EP), electro-osmosis (EO), dielectrophoresis (DEP), and electro-orientation, can be used as a driving force to steer, characterize and sort nanowires [69–71]. Those forces become one of the most dominant actuation sources when the particle dimensions decrease to micrometer and nanometer scales.

Compared with other nanomanipulation and nanoassembly techniques such as the tip-based approach [72,73], the use of electric-field-induced forces to drive a particle in fluidic suspension has advantages of ease and superior scalability. As a result, EP, EO and DEP have been explored in the past decade as driving forces to precisely control nanowire motion in microfluidic devices [74]. Each of those three phenomena (EP, EO and DEP) will be discussed and covered individually in the following subsections in order to identify the proper actuation to address the distributed feedback control, planning, and manipulation of nanowires with scalable and programmable electrode arrays.

### 1.2.2.1 EP based nanomanipulation

Under electric fields, particles in fluid suspension experience an electrophoretic force (EP force) under DC fields, while the fluid itself experiences EO forces [75]. The EP force magnitude is proportional to the effective electrokinetic potential (i.e., the zeta-potential) and the field strength. The use of EP force is convenient for actuation in that even nominally electrically neutral nanowires typically have a nonzero zeta-potential in the interfacial double layer in some solvents or at some pH. A large zeta-potential value is in fact a common stability criterion for colloidal suspensions. Thus, by actuating a set of electrode arrays, nanowires in fluid suspension can be manipulated, driven, and steered to desired locations under a precisely controlled electric field [70, 76, 77]. In [76, 78, 79], an EP-based motion-planning and manipulation scheme was developed to steer and drive a single nanowire in fluid suspension from one location to its targeted position. The nanowires were suspended in a droplet of fluid with a square-lattice electrode array on the bottom substrate of a micro-fluidic reservoir. Those electrodes can be independently actuated with different DC voltages to generate the electrical field to control the nanowires motion in the horizontal plane, while a top electrode is used to control the nanowires in the vertical direction. The extension of the EP-based motion planning and control for simultaneously driving multiple nanowires has been presented in [77, 80, 81]. The motion control in [76–81] also compensated for the EO flow induced by the electric field acting on the fluid. The work in [76–81] will be discussed in this dissertation.

### 1.2.2.2 DEP based nanomanipulation

Besides EP, DEP is also commonly used to drive and control nanowires in microfluidic devices [74, 82]. The induced dipole moment of the particle interacts with a non-uniform field to give rise to a frequency-dependent dielectrophoretic force. The DEP force is proportional to the polarizability of the particle and the gradient of the field



squared. In general, a particle can be either repelled or attracted to field concentrations depending on the sign of the polarizability. By tuning the field gradient and the frequency of the applied field, the DEP force can be used to manipulate the position of nanowires in fluidic suspension. The use of DEP to position nano-/micro-particles has been reported in many publications; see [74, 83, 84] for a review.

The DEP force depends on the spatial gradient of the square of the electric field, while EP force is proportional to the electric field strength. Therefore, EP-based manipulation is simple, requires lower electric fields, and is easier to implement for long-range motions. Most existing works on DEP-based manipulation in fluid suspension deal with spherical micro-particles such as beads and biological cells [85–96]. The DEP-based manipulation of high-aspect ratio nanowires and nanotubes, although less common, are reported in the literature [60, 97–104]. However, most of the prior works use the open-loop control of electrodes and do not consider the distributed feedback control of nanowires with programmable electrode arrays.

### **1.2.2.3 EO based nanomanipulation**

Use of the EO-based flow control is another way to steer and manipulate the particles and nanowires. In [69], the use of the EO-based flow control to steer and manipulate the particles and nanowires was extensively discussed and demonstrated. The microfluidic devices were fabricated with multiple electrodes to generate EO that steered and oriented particles [69] and nanowires [105] at the center of a star-shaped or cross-shaped microfluidic channel. EO modeling and optimization algorithms were used to steer and manipulate particles and nanowires in those designs. However, the control regions of those designs are always at the center of the microfluidic channel so that the directions of the EO-based flow form a four direction shear pattern and can be precisely modeled. Also, the device and the approach in [69] are difficult to scale up for large numbers of nanowires. In our design for electric-field-based motion control, both EP force and

EO flow are significant to the particle motion. However, due to lack of precise knowledge of the boundary conditions (planner flow in two dimensions), and specifically the unknown zeta-potential on both the particle and device boundaries, exactly modeling of the EO actuation is difficult. As shown in the experiments in [78], the EO-induced disturbances are not always aligned along with the electric field direction due to the complicated boundary conditions, and the existing models of the EO flow cannot be directly applied to our application. To overcome the modeling difficulties for EO flow, we design a robust motion-control algorithm that models the EP driving force and simultaneously compensates for the EO-induced motion disturbance.

Another piece of closely related work is the arbitrary steering of multiple particles by electroosmotic flow (EO flow) in [106]. However, the work in [106] did not consider motion planning of multiple nanowires in the configuration space. In addition, the cases that were considered involved a much larger number of actuators than the number of particles. For example, the approach in [106] used 20 electrodes to steer 8 nanoparticles in simulation and 3 nano-particles in experiments. Its scalability to a larger number of nanowires is however limited. The motion-planning scheme in this work significantly extends and complements the results in [106].

### **1.2.3 Motion planning of nanowires**

Motion planning of nanowires with a set of independently addressable electrodes is challenging due to its combinatorial optimization nature [107]. There are additional challenges to achieve the task of motion planning and control of more than one nanowire simultaneously. A closely related topic is the routing problem for droplets in digital microfluidic biochips (DMFB) [108–111]. In DMFB design, the droplets' motion is controlled by turning on and off a set of electrodes for a given roadmap configuration. The motion-planning problem in DMFB is to coordinate multiple objects' motion for minimum time to reach the desired configuration without collision [112]. The motion-planning problem considered in this dissertation is however different from those in the

DMFB design in several aspects. First, the motion of nanowires are much more complex than the droplets in DMFB, since the EO- and EP-induced motion is not restricted to only translation in four discrete directions, but occurs in continuous 3D space. Second, complete control of the nanoparticle motion in our case necessitates consideration of the orientation of the nanowire or nanotube, as well as position. Finally, the motion of nanowires under electric fields is controlled not only by the four electrodes within nearest distance but also a set of neighboring electrodes, and the nanowire motion highly depends on the actuation electrodes. Those differences significantly increase the complexity of EP/EO motion planning and control design.

The results of the minimum-time trajectory control of kinematic mobile robots with a finite input set in [113] are built on the assumption of individually self-propelled robots. Thus, those results cannot be directly applied to motion planning for EP- and EO-induced nanowire motion with the electric fields generated by the same set of multiple electrodes and possibly interacting nanowires. Indeed, the nanowire motion-planning problem is also related to the coordination of the collision-free motion of multiple robots to reach the desired configuration [112–115]. One of the main differences of the multiple-nanowire control problem lies in the steering actuation of multiple nanowires, which actually comes from the same set of electrodes. Therefore, the coupling of the actuation inputs brings the complexity of the motion planning and control. The actuation by electrodes cannot be decoupled for each nanowire, while each robot in [112–115] is driven independently by its onboard controller.

Other related research on the multiple-nanowire planning problem includes the work in [116, 117], in which a network-flow method is used to solve multi-agent path planning on graphs. However, these schemes only work for discrete motions of the agents, not for continuous motion space such as the nanowires under the EP force. Moreover, the actuation mechanism in this work is completely different with that in [116, 117].

While demonstrating the feasibility, in [76, 78, 79] we have developed an EP-based

motion planning and manipulation algorithm to steer and drive a single nanowire in fluid suspension. The extension of the EP-based motion planning and control for simultaneously driving multiple nanowires is presented in [77, 80]. Due to the complexity of the combinatorial optimization, the motion planning algorithm (i.e., the two-stage planning approach) in [77, 80] uses a heuristic technique to quickly generate the shortest-distance collision-free trajectories for multiple nanowires. Obstacle avoidance is also considered in the planning algorithm. The performance of the two-stage algorithm in [77, 80] can be further improved in several aspects as proposed in [81]. First, as illustrated in [76], the shortest total traveling distances of all nanowires do not imply the shortest traveling time. Indeed, the shortest traveling-time trajectory is not the straight-line connecting the starting to target points due to the electric field distribution. Therefore, it is desirable to obtain the minimum-time trajectory for fast manipulation. Second, because of the straight-line constraint, the maximum number of nanowires that can be simultaneously independently steered in the two-stage algorithm is limited to an upper-bound. For scalability, it is desirable to find an alternative motion planner to relax such constraints.

Optimal control approaches are not effective for the multi-nanowire motion-planning problem. Numerical optimization can be used but it suffers from local minima and expensive computations and therefore, it cannot be applied to the case of more than two simultaneous nanowires. Also, algebraic solutions of optimal control are available primarily for 2D point mass systems [118]. In literature, the optimal control approaches are investigated to achieve the time-optimal objective of one particle in a dielectrophoretic system [119, 120]. However, the authors only consider the motion of one particle on an invariant line, not the whole continuous horizontal plane, and the result cannot be directly applied to multiple particles due to the system construction. The search-based methods compute paths over discretizations of the continuous state space but the computation depends exponentially on the grid size [121]. Sampling-based methods such as Rapidly-exploring Random Tree (RRT) and its variants take

sample points in the collision-free space and add them to a tree covering the whole space with probabilistic complete property [107]. An RRT-based path planning approach to transporting cells with optical tweezers is investigated in [122]. However, RRT algorithm cannot guarantee optimality. Although the RRT\* algorithm [123] is asymptotically optimal, the convergence is slow especially for large scale problems. Sparse roadmaps are applied to provide asymptotically near-optimality in [124] and a sparse tree that covered the state space with a basin of attraction is proposed in [125] with linear quadratic regulator (LQR) feedback-based motion planning. Recently, a sparse structure RRT (SST) [126] has achieved asymptotic optimality for kinodynamic planning using incremental sampling-based planners. This approach takes advantage of sparse structure to return a solution quickly and converges to a sub-optimal solution.

The work in [81] consider a time-optimal motion-planning and control strategy of multiple nanowires in fluid suspensions. The work takes the advantages of both SST and RRT\* approaches. An improved sparse RRT\* based motion-planning algorithm, called SRRT\*, is proposed to generate the asymptotically near time-optimal trajectories of multiple nanowires. Unlike the two-stage planning approach in [77, 80], the maximum number of nanowires that can be steered at one time is not limited by an upper bound. The SRRT\* algorithm takes the advantages of the rewiring strategy of the RRT\* and the sparse structure of the SST to efficiently achieve the asymptotically near time-optimal trajectory with several heuristic techniques.

### **1.3 Dissertation outline and contributions**

There are seven chapters in this dissertation. Chapter 1 presents the introduction and background. Chapter 2 analyzes the nanowire motion in dilute suspension under EP force and presents an electric-field model with a simple, generic set of controllable electrodes. A novel, automated electric-field-based single-nanowire motion control, planning, and manipulation scheme is presented in Chapter 3. In order to improve

the efficiency of nanomanipulation, Chapter 4 and Chapter 5 discuss simultaneous multiple-nanowire motion control, planning, and manipulation problems to achieve shortest distance and minimum time objectives, respectively. An integrated procedure for automated characterization, manipulation, and assembly of nanowires is proposed in Chapter 6 to demonstrate the feasibility of fabricating functional nanodevices using the proposed planning and control strategies. Concluding remarks and discussion of the future work directions are presented in Chapter 7. The content of each chapter is described in details as follows.

In Chapter 2, we first summarize the lowest-order electric field induced forces acting on a particle in suspension and present a dynamic model of nanowires under EP force. Next, we propose a micro-fluidic device design that is actuated by a simple, scalable, and generic set of electrodes to precisely generate controllable electric fields. With the symmetric properties of the electrode array, a superposition approach is developed to efficiently compute the electric-field distribution in the fluid that is contained by the micro-fluidic device.

In Chapter 3, an EP-based motion control of the nanowire in dilute suspension with the aforementioned controllable electrodes is first presented to precisely control the motion of individual nanowires. We design the motion control algorithm for individual nanowires by extending the path-following approach in [127, 128]. A time suspension technique is used to tune the desired nanowire velocity online depending on the path-following errors and error prediction. We then discuss geometric properties relevant to the electric-field-based single-nanowire motion planning and control problem. Due to the NP-hard complexity, we present several heuristic planning solutions and compare their performance with the other well-known benchmark motion planning approaches such as RRT and  $A^*$  algorithms [107]. The comparisons show that the proposed heuristic algorithms obtain sub-optimal minimum time trajectories. Extensive experimental and numerical results confirm the performance of the proposed motion planning and manipulation. Finally, we demonstrate an integrated process to position,

orient and deposit multiple nanowires sequentially onto the substrate. The integrated nanowire manipulation confirms the potential of using the proposed EP-based strategy to steer and deposit nanowires precisely.

Chapter 4 presents the motion-planning and control algorithms for simultaneous manipulation of multiple nanowires in liquid suspension. We first present an EP force-based control algorithm to simultaneously steer multiple nanowires along given trajectories. We further provide the control-system properties that capture the relationship between the maximum number of the simultaneously controllable nanowires and the available number of actuated electrodes. A two-stage motion-planning algorithm is then presented to generate the desired trajectories for multiple nanowires with minimum total traveling distances. Furthermore, we demonstrate the motion control and planning of simultaneous multiple nanowires to form various geometric patterns and track different trajectories. The performance of the proposed motion-planning and control algorithms is validated through numerical simulations and extensive experiments.

To improve nanomanipulation efficiency, we extend the results in Chapter 4 and present the time-optimal motion planning and control of multiple nanowires simultaneously in fluid suspensions in Chapter 5. The EP-force is still used as the primary driving force and the motion control design compensates for the electro-osmosis disturbance. Inspired by the SST and RRT\* approaches, an improved sparse RRT\* based motion-planning algorithm SRRT\* is proposed to generate the asymptotically near time-optimal trajectories of multiple nanowires. The algorithm is not restricted to the time-optimal cost function and any other cost functions can be incorporated into the algorithm. Moreover, unlike the previous results in Chapter 5, the maximum number of nanowires that can be steered at one time is not limited by an upper bound that depends on the number of neighboring electrodes. The SRRT\* algorithm takes the advantages of the rewiring strategy of the RRT\* and the stable sparse structure of the SST to efficiently achieve the near-optimal trajectories with several heuristic techniques. Also, the SRRT\* guarantees the asymptotically near-time-optimal performance

for multiple nanowires. Finally, we demonstrate the minimum-time performance of the proposed motion-planning and control algorithms through numerical simulations and experiments.

In Chapter 6, we propose a completely integrated procedure of automated characterization, simultaneous manipulation, and assembly of nanowires to build functional nanodevices. Particularly, we assemble silicon-nanowire-based FET devices by their electrical conductivities using the proposed integrated strategies. The measurement results confirm the effectiveness and feasibility of the integrated characterization, manipulation and assembly procedure. Finally, we discuss the remaining improvements of proposed work and other potential applications towards biomedical systems in Chapter 7. The demonstration of the effectiveness and functionality of the biomedical applications is out of the scope of this dissertation and remains as the future work.

The main contributions of this dissertation are described in details as follows.

1. A novel design is proposed for the motion control, planning, and manipulation of nanowires under electric-fields in fluid suspension. The design and algorithms are experimentally and numerically demonstrated, and can serve as enabling techniques for scalable and automated manufacturing of nanowire-based functional devices for many potential applications.
2. The formulation and heuristic solutions of the electric-field-based nanowire motion planning under distributed electrode arrays in Chapter 3 are new and complement to the existing results (e.g., routing algorithms for DMFB [108, 110] and minimum-time trajectory control of self-propelled kinematic robots [113]).
3. Robust motion control strategies compensate for the un-modeled flow disturbance, and path-following errors guarantee convergence for both individual nanowire and simultaneous multiple nanowires.
4. A network-flow based two-stage algorithm captures simultaneous motion-control capacity limits and generates the shortest path planning for simultaneous multiple



nanowires. The proposed SRRT\* algorithm generates computationally efficient, obstacle-avoiding, and near-optimal path with no motion-control capacity limitations. All the motion-planning algorithms significantly reduce the computational complexity, yet maintain comparable or near-optimal performance. Extensive experiments and simulation validate the feasibility and effectiveness. The developed algorithms and microfluidic device potentially enable the scalable manipulation of multiple simultaneous nanowires using EP forces and the scalable assembly of nanodevices for a variety of applications.

5. Finally, we present a novel integrated procedure for automated characterization, manipulation, and assembly of nanowires to fabricate functional nanodevices. Silicon nanowires are separated and deposited using the integrated scheme. The assembled FETs using those separated nanowires have demonstrated different characteristics according to the automated separation criterion. The separated high-performance-nanowire based FETs have shown excellent performance, yielding high on-current, small sub-threshold swing and high device mobility. The measurement results confirm the feasibility and effectiveness of the integrated scheme.

In summary, the proposed motion control, planning, and manipulation scheme builds a foundation for scalable, automated, and precise manipulating nanowires to build functional nanodevices, and provides appealingly simple and effective means to hold and position microscopic objects. Finally, the proposed motion planning and motion control strategies can also be generalized to many other robotics applications, in which the actuation among a group of multiple robots or agents are coupled or intertwined.

## Chapter 2

# Electric-Field Based Nanowire Manipulation Modeling and Configuration

### 2.1 Introduction

In order to investigate and achieve scalable manipulation of nanostructures, we design a simple and generic set of lattice-shape distributed electrode array to actuate suspended nanowires under electric-fields in fluid suspension. The precisely controlled electric fields generated by electrode arrays can be used to control the motion of nanowire. We then present a dynamic model of nanowires motion in dilute suspension with the designed set of  $N \times N$  controllable electrodes. Finally, we present a superposition approach to efficiently compute the electrical-field distribution for a given set of electrodes.

### 2.2 System configuration

Figure 2.1(a) shows the schematic of the micro-fluidic device. We consider a device with  $N \times N$  electrodes on the bottom surface. The array of circular electrodes with radius  $R$  are fabricated on a glass substrate with equal distance  $L$  between centers (Figure 2.1(b)). Each electrode is independently actuated with a DC voltage. The electrode arrays are covered by fluid containing a dilute concentration of nanowires. A glass coverslip is used to cover the fluid and form a flow reservoir.

The use of the electrodes on the non-conducting bottom surface creates an electric field inside the fluid reservoir that is primarily parallel to the substrate surface. Under

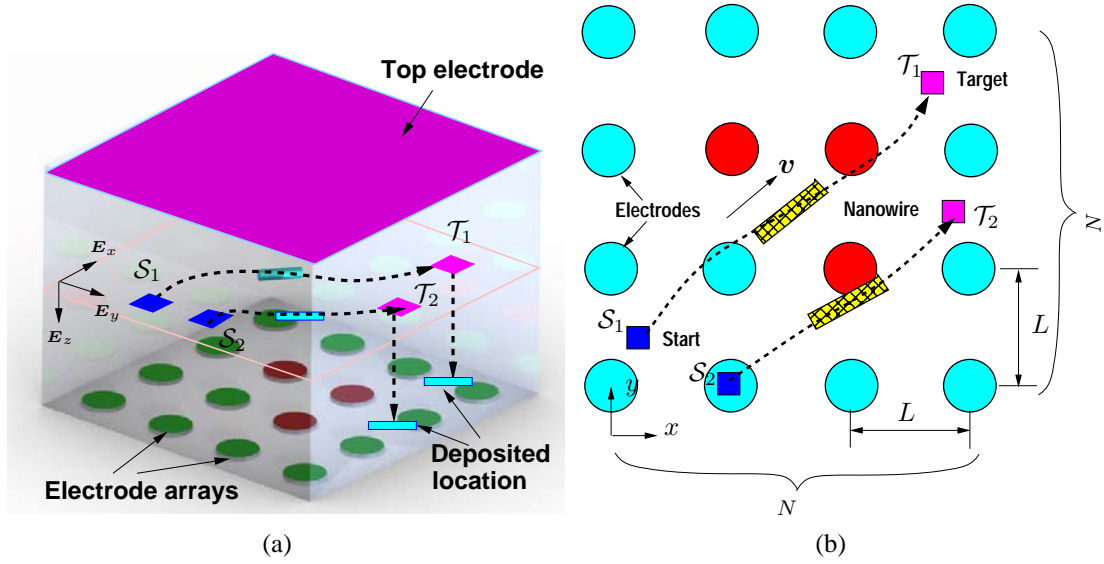


Figure 2.1: Schematic of microfluidic device with  $N \times N$  electrodes. (a) 3D view of micro-fluidic device with  $N \times N$  independently actuated electrodes on a bottom substrate, with a common top electrode. (b) Top view of the motion trajectories of nanowires induced by the electrode array.

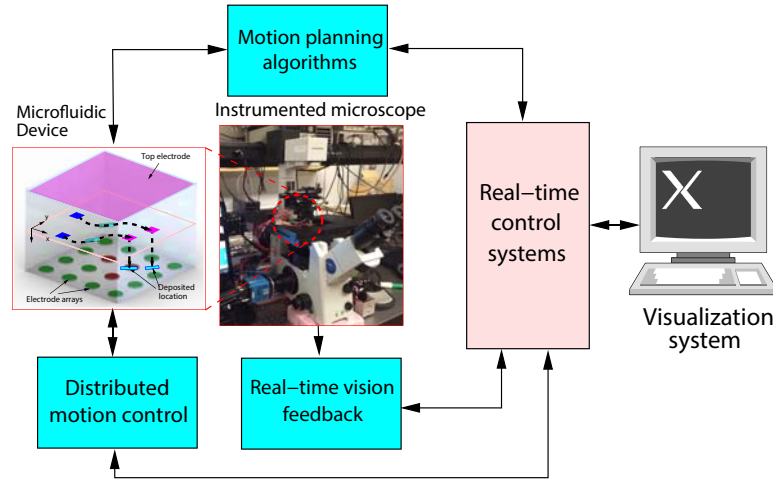


Figure 2.2: A schematic of an electric-field-based nanowires motion control, planning and manipulation scheme.

this largely horizontal electric field, the nanowires orient and move under EP and EO forces. As shown in Figure 2.1(a), a common electrode is used as the top coverslip to vertically position the nanowires and deposit them at desired locations on the substrate. When manipulating nanowire motion in the horizontal plane, the top electrode does not serve as the ground and no voltage is applied to the top electrode. For example, for the

two nanowires in fluid suspension at locations  $\mathcal{S}_1$  and  $\mathcal{S}_2$  shown in Figure 2.1(a), we first actuate the electrode array on the bottom surface to steer and drive the nanowires to the targeted horizontal locations  $\mathcal{T}_1$  and  $\mathcal{T}_2$  in the horizontal plane. Then, the bottom electrodes are turned off and the electrode on the top surface is turned on to align and drive the nanowires vertically until they reach the bottom substrate. Finally, the electrode arrays are turned on again to lay down and deposit the nanowire onto the device surface with the desired orientation.

Figure 2.2 illustrates the schematic of the electric-field-based nanowire motion control, planning, and manipulation scheme. The nanowire motion control is based on a model of nanowire dynamics under EP-force actuation, with vision-based feedback control of the nanowire positioning. The control system also compensates for the complex 3D EO flow that is un-modeled. The motion planner determines the optimized motion trajectory for given target points and nanowire's current position.

We denote the electrode as  $e_{ij}$  at the  $i$ th row and the  $j$ th column,  $i, j = 1, \dots, N$ . We define the electrode control matrix  $\mathbf{u} = \{u_{ij}\}$ ,  $i, j = 1, \dots, N$ , with

$$u_{ij} = \begin{cases} V_{ij} & \text{if } e_{ij} \text{ is turned "on",} \\ 0 & \text{if } e_{ij} \text{ is turned "off".} \end{cases} \quad (2.1)$$

where  $V_{ij}$  is the voltage applied to  $e_{ij}$ . Among  $\mathbf{u}$ , a total of  $N_a \leq N^2$  actuated (i.e., powered-“on”) electrodes are captured by indexing all non-zero elements  $u_{ij}$  into *effective electrode set*  $\mathbf{U} = \{e_{I_k} : I_k = (i, j), u_{ij} \neq 0\}$  with  $|\mathbf{U}| = N_a$ , where  $|\cdot|$  is the cardinality of a set.

For nanowire manipulation using the device shown in Figure 2.1, we mainly consider the following motion control and planning problems.

*Motion Control Problem:* find electrode control  $\mathbf{u}(t)$  at time  $t$  to steer all the nanowires to follow a given trajectory.

*Motion Planning Problem:* for all the nanowires, given starting and target locations  $\mathcal{S}$  and  $\mathcal{T}$ , find an optimal collision-free path that the nanowires achieve certain objective, i.e., minimal total travel distance or total travelling time, from  $\mathcal{S}$  to  $\mathcal{T}$ .

### 2.3 EP-based nanowire motion model

We model the nanowire as a prolate spheroid shape as illustrated in Figure 2.3. A body-fixed coordinate system  $xyz$  is chosen that is aligned with the principle axes of the ellipsoid. A particle moving in a viscous flow is subjected to hydrodynamic forces. If the movement of the prolate spheroid particle is aligned with its main axis (i.e.,  $z$ -axis), the hydrodynamic drag of the prolate spheroid can be evaluated by [129]

$$\mathbf{F}_{drag} = \frac{-8\pi\mu c\mathbf{v}}{[(a/c)^2 + 1] \coth^{-1}(a/c) - a/c} = -6\pi\mu b\mathbf{v}R, \quad (2.2)$$

where  $\mu$  is the dynamic viscosity,  $\mathbf{v}$  is the relative velocity vector of the fluid with respect to the particle,  $a$  and  $b$  are the major and the minor radii of ellipse,  $c = \sqrt{a^2 - b^2}$ , and

$$R = \frac{4}{3\sqrt{(a/c)^2 - 1} \{[(a/c)^2 + 1] \coth^{-1}(a/c) - a/c\}}.$$

We assume that the nanowire is always aligned and moving tangential to the electric field, as any misalignment from the field direction leads to a restoring torque which tends to orient the nanowire with the field [130].

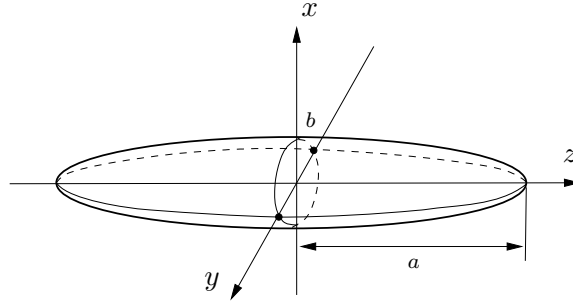


Figure 2.3: Prolate spheroid nanowire with major radius  $a$  and minor radius  $b$ .

Assuming a thin electric double layer for the particle and no retardation effect, the EP force  $\mathbf{F}_{EP}$  acting on a particle in liquid suspension is given by

$$\mathbf{F}_{EP} = 6\pi\mu b\mu_e R\mathbf{E} = 6\pi b\epsilon_m\zeta R\mathbf{E}, \quad (2.3)$$

where  $\mathbf{E}$  is the DC electric field vector,  $\zeta$  is the zeta-potential of the suspended particle (which can be experimentally determined), and  $\mu_e = \epsilon_m\zeta/\mu$ , is the electrophoretic mobility, where  $\epsilon_m$  is the electric permittivity.

Due to small Reynolds numbers for the particle motion, the particle is always at steady state and the inertial force is negligible for nanowires motion. Therefore, the EP force is balanced by the hydrodynamic viscous drag force, so that  $\mathbf{F}_{EP} + \mathbf{F}_{drag} = 0$ . Using (2.2) and (2.3), we obtain

$$\mathbf{v} = \begin{bmatrix} v_x \\ v_y \end{bmatrix} = \frac{\epsilon_m \zeta \mathbf{E}}{\mu}. \quad (2.4)$$

Brownian translation and rotation of the nanowires are neglected in the model for sufficiently large magnitudes of the viscous-flow and electric-field-induced forces [131, 132]. The motion equation (2.4) implies that the velocity of the nanowire is independent of the nanowire geometry (e.g., size and shape), provided we can assume a thin double layer and uniform zeta potential [133].

From (2.4), the velocity magnitude of the nanowire in the suspended plane is proportional to the magnitude of the electric field  $\|\mathbf{E}\|$ , and the direction of motion of the nanowire is along the electric field. By appropriately switching the powered-“on” electrodes, the electric field  $\mathbf{E}$  can be changed and used to control a nanowire’s motion.

## 2.4 Electric-field modeling

Since Gauss’ law for electric fields is linear, the electric-field  $\mathbf{E}_p$  near nanowire  $P$  can be calculated by superposition of the electric-field vectors for each power-“on” electrode, namely,

$$\mathbf{E}_p = \sum_{e_{I_k} \in U} \mathbf{E}_k(P), \quad (2.5)$$

where  $\mathbf{E}_k(P)$  is the electric field near  $P$  under powered-“on” electrode  $e_{I_k} \in U$ . In the following, we describe how to efficiently compute  $\mathbf{E}_p$ .

We consider a nanowire  $P$  located at  $\mathbf{r}_n(P) = [x \ y]^T$ . The coordinate of electrode  $e_{ij}$  is denoted as  $\mathbf{r}_{e_{ij}}$ . To determine the electric-field at  $\mathbf{r}_n(P)$ , we use the high-fidelity package COMSOL to evaluate the effect of turning on one electrode near  $P$ . Only activated electrodes within a  $r_p$ -array-distance range ( $r_p L$ ) with respect to nanowire  $P$

are found to have a significant effect on the electric field at  $\mathbf{r}_n(P)$ , namely, electrodes  $e_{ij}$  satisfy  $\|\mathbf{r}_n(P) - \mathbf{r}_{e_{ij}}\|_1 \leq r_p L$ , where  $\|\mathbf{x}\|_1$  is the 1-norm of vector  $\mathbf{x} \in \mathbb{R}^2$ , and  $r_p \in \mathbb{N}$  is the effective radius. From COMSOL simulation,  $r_p = 2$  for the square lattice arrays designs that proposed in this dissertation. As shown in Figure 2.4(a), for nanowire  $P$  located inside array cell  $ABCD$  and  $r_p = 2$ , the electric field inside  $ABCD$  is influenced primarily by electrodes within  $A'B'C'D'$  shown as the dot-dash lines. For presentation convenience, we define the *atomic* and *basic electrode sets*  $\mathcal{E}_a(P)$  and  $\mathcal{E}_b(P)$  for nanowire  $P$ , respectively, as

$$\mathcal{E}_a(P) = \{e_{ij} : \|\mathbf{r}_n(P) - \mathbf{r}_{e_{ij}}\|_1 \leq L\}, \quad (2.6)$$

and

$$\mathcal{E}_b(P) = \{e_{ij} : \|\mathbf{r}_n(P) - \mathbf{r}_{e_{ij}}\|_1 \leq r_p L\}. \quad (2.7)$$

For example,  $\mathcal{E}_a(P)$  and  $\mathcal{E}_b(P)$  contain the electrodes in areas  $ABCD$  and  $A'B'C'D'$  in Figure 2.4(a), respectively.

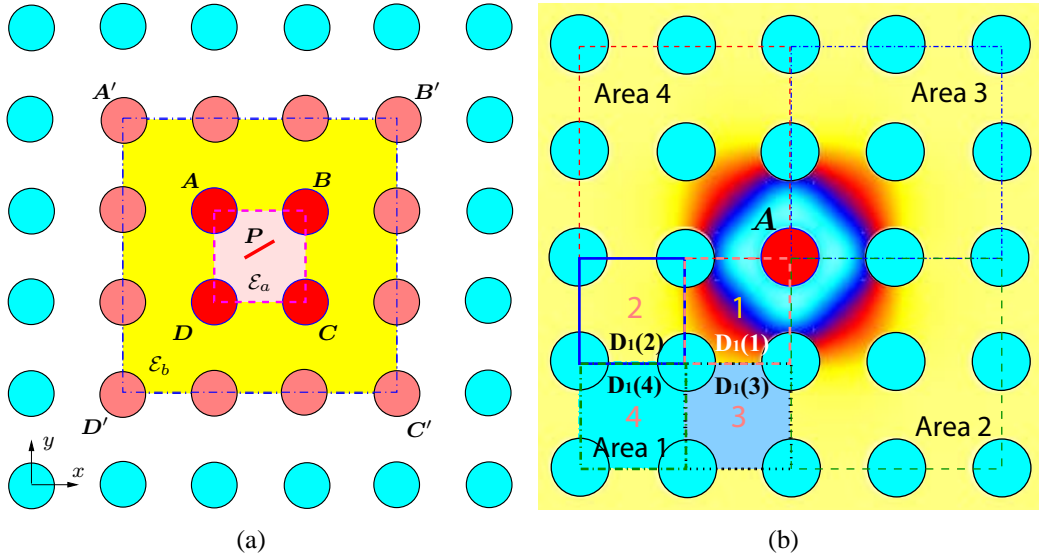


Figure 2.4: (a) A schematic of an atomic and basic areas around nanowire  $P$ . (b) An illustrative schematic diagram to compute the electric field by turning on one electrode.

To calculate the electric field in  $\mathcal{E}_a(P)$ , we shall compute the electric field generated by turning on each electrode in set  $\mathcal{E}_b(P) \cap U$  and then superpose them by (2.5). Notice that the influence of a powered-“on” electrode only affects the electric field

within a distance range of  $r_p L$ . Therefore, let us consider the case when one electrode is “on” and find out how to compute the electric field. Figure 2.4(b) illustrates a case that electrode  $A$  is “on” and all other electrodes in its neighbor within  $\mathcal{E}_b(A)$  are “off” (i.e., grounded). Due to symmetry, the electric fields are the same around  $A$  in four quadrant areas. With this observation, we build the electric field data for one quadrant area (i.e., four atomic cells) and then compute the electric field in the other three quadrant areas by symmetry. We here label region of each atomic electrode cell as  $D_j(i)$ , where index  $i = 1, 2, 3, 4$  indicates the atomic cell number in each quadrant area and  $j = 1, 2, 3, 4$  indicates the left-bottom, right-bottom, right-top and left-top quadrant areas, respectively, as shown in Figure 2.4(b). Moreover, for the four atomic cells  $D_1(i)$  on the left-bottom corner shown in Figure 2.4(b), the electric fields are denoted as  $\mathbf{E}_1(i)$ ,  $i = 1, 2, 3, 4$ , and assumed known.

---

**Algorithm 1:** E-field Generation Algorithm

---

**Input :**  $\mathbf{r}_n(P)$ ,  $U$  and  $\mathbf{E}_1(k)$ ,  $k = 1, 2, 3, 4$

**Output :**  $\mathbf{E}_p$

$\mathcal{E}_b(P) = \{e_{ij} : \|\mathbf{r}_n(P) - \mathbf{r}_{e_{ij}}\|_1 \leq r_p L\}$

$\mathcal{E}_{act}(P) = \mathcal{E}_b(P) \cap U$ ,  $\mathbf{E}_{xi}(P)$ ,  $\mathbf{E}_{yi}(P) \leftarrow \text{NULL}$

$\mathbf{E}_{x1}(k) = \text{proj}_x(\mathbf{E}_1(k))$ ,  $\mathbf{E}_{y1}(k) = \text{proj}_y(\mathbf{E}_1(k))$

**for**  $i \in \mathcal{E}_{act}(P)$  **do**

**if**  $\mathbf{r}_n(P) \in D_1(k)$  **then**

$\mathbf{E}_{xi}(P) \leftarrow \mathbf{E}_{xi}(P) + \mathbf{E}_{x1}(k)$

$\mathbf{E}_{yi}(P) \leftarrow \mathbf{E}_{yi}(P) + \mathbf{E}_{y1}(k)$

**else if**  $\mathbf{r}_n(P) \in D_2(k)$  **then**

$\mathbf{E}_{xi}(P) \leftarrow \mathbf{E}_{xi}(P) - \text{mirrorLR}(\mathbf{E}_{x1}(k))$

$\mathbf{E}_{yi}(P) \leftarrow \mathbf{E}_{yi}(P) + \text{mirrorLR}(\mathbf{E}_{y1}(k))$

**else if**  $\mathbf{r}_n(P) \in D_3(k)$  **then**

$\mathbf{E}_{xi}(P) \leftarrow \mathbf{E}_{xi}(P) - \text{Rot}(\mathbf{E}_{x1}(k), \pi)$

$\mathbf{E}_{yi}(P) \leftarrow \mathbf{E}_{yi}(P) - \text{Rot}(\mathbf{E}_{y1}(k), \pi)$

**else**

$\mathbf{E}_{xi}(P) \leftarrow \mathbf{E}_{xi}(P) + \text{mirrorUD}(\mathbf{E}_{x1}(k))$

$\mathbf{E}_{yi}(P) \leftarrow \mathbf{E}_{yi}(P) - \text{mirrorUD}(\mathbf{E}_{y1}(k))$

**end**

$\mathbf{E}_i(P) = [\mathbf{E}_{xi}(P), \mathbf{E}_{yi}(P)]$

**end**

$\mathbf{E}_p = \sum_{i \in \mathcal{E}_{act}(P)} \mathbf{E}_i(P)$

---



Algorithm 1 illustrates the computing of the electric field within  $\mathcal{E}_a(P)$ . The algorithm first computes sets  $\mathcal{E}_a(P)$  and  $\mathcal{E}_b(P)$ . Since the actuated electrodes are given in  $U$ , the algorithm then finds the subset of powered-“on” electrodes in  $\mathcal{E}_b(P)$ , denoted as  $\mathcal{E}_{act}(P) = \mathcal{E}_b(P) \cap U$ . For each “on” electrode in  $\mathcal{E}_{act}(P)$ , the algorithm computes the electric field  $\mathbf{E}_i$  within area  $\mathcal{E}_a(P)$ . By flipping up and down, left and right, or rotating  $\pi$ , we get the electric field  $\mathbf{E}_i(P)$  within  $\mathcal{E}_a(P)$  for each actuated electrode. Since  $|\mathcal{E}_{act}(P)| \leq 16$ , the complexity of Algorithm 1 is  $O(1)$ .

## 2.5 Conclusion

In this chapter, we present the system modeling and configuration of the electric-field-based nanowire manipulation in liquid suspension with a simple, generic set of electrodes. The main contributions of the work in this chapter are twofold. First, we present a novel schematic of design for EP-based nanowires manipulation system in fluid suspension. Second, with the symmetry properties of the designed electrode array, an efficient electric-field calculation algorithm was designed, which could provide the foundation of efficient motion control of nanowires with the dynamic model under EP force.

## **Chapter 3**

# **Motion Control, Planning and Manipulation of Individual Nanowires under Electric-Fields in Fluid Suspension**

### **3.1 Introduction**

To fully realize the enormous potential of functional nanodevices, automated, scalable methods are needed to manipulate and assemble nanowires and nanotubes with controlled orientations at specific spatial locations. This chapter presents one such technique for the automated motion planning, control and manipulation of individual nanowires suspended in a fluid. Based on the system design in Chapter 2, the suspended nanowires in dilute solution are precisely driven by the controlled electric field generated by the set of lattice-shape distributed electrode arrays. Built on the dynamic model of nanowire motion in fluid suspension, a vision based path-following control strategy is presented to guide the nanowire to follow a given desired trajectory. The control system design incorporates the potential function approach to compensate for un-modeled complex electro-osmotic flow motion. We design an integrated process to steer, orient and deposit multiple nanowires sequentially to form various geometric shapes. Extensive experimental results are presented to demonstrate the motion control and manipulation algorithms.

In this chapter, we mainly focus on the motion control, planning, and manipulation of individual nanowires under electric-fields in fluid suspension. We first present the motion control of nanowires under EP in an electric-field. We then discuss geometric properties relevant to the electric-field-based single-nanowire motion planning and

control problem. Due to the NP-hard complexity, we present several heuristic control solutions and compare with the other well-known motion planning approaches such as rapidly-exploring random tree (RRT) and  $A^*$  algorithms [107]. Extensive experimental and numerical results confirm the performance of the proposed motion planning and manipulation. We finally present a set of experiments to demonstrate the feasibility of using EP-based devices to steer and deposit nanowires to potentially fabricate nanodevices. The results will help provide a foundation for scalable, automated methods for manipulating nanowires to build nanodevices.

The main contributions of this work are twofold. First, we present a novel design for the motion control, planning, and manipulation of individual nanowires under electric-fields in fluid suspension. The design and algorithms are experimentally and numerically demonstrated, which could serve as enabling techniques for scalable and automated manufacturing nanowire-based functional devices for many potential applications. Secondly, the formulation and heuristic solutions of the electric-field-based nanowire motion planning under distributed electrode arrays are new and complement the existing results (e.g., routing algorithms for DMFB [108, 110] and minimum-time trajectory control of self-propelled kinematic robots [113]).

The rest of the chapter is organized as follows. We present the system configuration and the problem formulation in Section 3.2. The motion control of nanowires under EP forces is discussed in Section 3.3 and the motion planning algorithms are presented in Section 3.4. Experimental results are presented in Section 3.5 before we conclude this chapter in Section 3.6.

## 3.2 Problem formulation

Although this chapter only deal with individual nanowires, the microfluidic device is designed as same as the fluid reservoir with  $N \times N$  electrodes array on the bottom surface, as shown in Figure 2.1 in chapter 2. The electrode arrays are covered by

fluid containing a dilute concentration of nanowires. A glass coverslip is used to cover the fluid and form the flow reservoir. The actual device is shown in Section 3.5.1. Each electrode, denoted as  $e_{ij}$  at the  $i$ th row and the  $j$ th column,  $i, j = 1, \dots, N$ , is independently actuated with a DC voltage and for simplicity, the same actuation voltage is applied to all electrodes. Therefore, the electrode control matrix  $\mathbf{u} = \{u_{ij}\}$ ,  $i, j = 1, \dots, N$ , defined in (3.1) becomes

$$u_{ij} = \begin{cases} 1 & \text{if } e_{ij} \text{ is turned "on",} \\ 0 & \text{if } e_{ij} \text{ is turned "off".} \end{cases} \quad (3.1)$$

Different from simultaneously control of multiple nanowires as shown in Figure 2.1, we first only consider the individual nanowire in this chapter. Hence, the following motion control and planning problems are considered.

*Motion Control Problem:* find electrode control  $\mathbf{u}(t)$  at time  $t$  to steer the nanowire to follow a given trajectory  $\mathcal{C}(x_d, y_d)$ .

*Motion Planning Problem:* for given starting and target locations  $\mathcal{S}$  and  $\mathcal{T}$ , find a planning path  $\mathcal{P}$  that the nanowire takes minimum time from  $\mathcal{S}$  to  $\mathcal{T}$ .

In Sections 3.3 and 3.4, we will present how to solve the above two problems, respectively.

### 3.3 Nanowire motion control

The goal of the motion control is to steer the nanowire to follow a given trajectory  $\mathcal{C}(x_d, y_d)$ . As shown in the experiments in Section 3.5, the nanowire motion is affected significantly by EO flow of the suspending fluid and thus, the control design must be robust enough to compensate for any un-modeled disturbances.

We extend the potential function approach in [127, 128] to design the path-following control of  $\mathcal{C}(x_d(\tau), y_d(\tau))$ , which is parameterized by time variable  $\tau$ , instead of time  $t$ . We here present the discrete-time motion controller design. The following potential

function is used to capture the path-following position errors along  $\mathcal{C}$  at the  $k$ th step.

$$U(\boldsymbol{\theta}(k)) = \frac{1}{2}\beta_1 \left[ (1 - \cos 2\theta_x(k)) + (1 - \cos 2\theta_y(k)) \right], \quad (3.2)$$

where  $\beta_1 > 0$  is a constant gain,  $\boldsymbol{\theta}(k) = [\theta_x(k) \ \theta_y(k)]^T$ ,  $\theta_x(k) = \tan^{-1} e_x(k)$ ,  $\theta_y(k) = \tan^{-1} e_y(k)$ , and the position errors  $e_x$  and  $e_y$  are defined as

$$\mathbf{e}(k) = \begin{bmatrix} e_x(k) \\ e_y(k) \end{bmatrix} = \begin{bmatrix} x(k) - x_d(k) \\ y(k) - y_d(k) \end{bmatrix}. \quad (3.3)$$

The position variables at the  $k$ th step for the nanowire and its desired locations are respectively as  $x(k) = x(k\Delta t)$ ,  $y(k) = y(k\Delta t)$ , and  $x_d(k) = x_d(\tau_k)$ ,  $y_d(k) = y_d(\tau_k)$ , where  $\Delta t$  is the constant sampling period. The updating law for  $\tau_k$  will be given later in this section.

At the  $k$ th step, the desired velocity  $\mathbf{v}^d(k) = [v_x^d(k) \ v_y^d(k)]^T$  is calculated by

$$\begin{bmatrix} v_x^d(k) \\ v_y^d(k) \end{bmatrix} = \lambda_1 \begin{bmatrix} \frac{dx_d}{d\tau} \\ \frac{dy_d}{d\tau} \end{bmatrix} - \lambda_2 \begin{bmatrix} \sin 2\theta_x(k) \\ \sin 2\theta_y(k) \end{bmatrix} - \lambda_3 \begin{bmatrix} \hat{e}_x(k) \\ \hat{e}_y(k) \end{bmatrix}, \quad (3.4)$$

where  $\lambda_1 = e^{-\beta_2 U(\boldsymbol{\theta}(k))}$ ,  $\lambda_2 = 2 - e^{-\beta_2 U(\boldsymbol{\theta}(k))}$ ,  $\beta_2 > 0$  is a self-pacing parameter and  $\lambda_3$  is a positive constant parameter. The error prediction, namely, the last term in (3.4), is calculated by

$$\hat{\mathbf{e}}(k) = \begin{bmatrix} \hat{e}_x(k) \\ \hat{e}_y(k) \end{bmatrix} = \alpha_1 \mathbf{e}(k) + \alpha_2 [\mathbf{e}(k) - \mathbf{e}(k-1)], \quad (3.5)$$

where positive constants  $\alpha_1, \alpha_2 > 0$  are design parameters.

Note that the first term in the right hand of (3.4) indicates the direction of the desired trajectory  $\mathcal{C}$ , the second term penalizes the tracking direction and the third term tries to compensate the predicted error for the next time period using the past two-step error measurements as given in (3.5). The time parameter updating is given by the following dynamics

$$\tau_{k+1} = \tau_k + \lambda_1 \Delta t. \quad (3.6)$$

Finally, we need to determine the powered-“on” electrodes such that the electric field  $\mathbf{E}_p(k)$  is to steer nanowire velocity  $\mathbf{v}(k)$  in (2.4) to follow  $\mathbf{v}^d(k)$  given by (3.4). To determine the controlled electrodes, we formulate an optimization approach to determine the actuation electrodes control  $\mathbf{u}^*(k)$  as follows.

$$\mathbf{u}^*(k) = \arg_{e_{ij} \in \mathcal{E}_b(P)} \min \|\mathbf{v}_c(k) - \mathbf{v}^d(k)\|, \quad (3.7)$$

where  $\mathbf{v}_c(k) = \frac{\epsilon_m \zeta \mathbf{E}(\mathbf{u}(k))}{\mu}$  for a given electrode control  $\mathbf{u}(k)$  for  $e_{ij} \in \mathcal{E}_b(P)$ .

With the above design, we have the following property.

**Lemma 3.1.** *If the nanowire velocity  $\mathbf{v}$  follows  $\mathbf{v}^d$  precisely, then path-following errors converge to zero, namely,  $\mathbf{e}(t) \rightarrow \mathbf{0}$ .*

*Proof.* The proof of Lemma 3.1 extends the approach in [127] and we here discuss the continuous-time case.

Let us denote the nanowire 2D position vector  $\mathbf{q} = [x \ y]^T$  and error (3.3) is then written as  $\mathbf{e}(\mathbf{q}, \tau) = [e_x \ e_y]^T$ . We denote  $\Delta = [\Delta_x \ \Delta_y]^T = [2\theta_x \ 2\theta_y]^T$ . The potential function (3.2) is written as

$$U(\Delta) = \frac{1}{2} \beta_1 [(1 - \cos \Delta_x) + (1 - \cos \Delta_y)].$$

Note that  $U(\Delta)$  is lower bounded, i.e.,  $U(\Delta) \geq 0$ , and the time derivative of  $U(\Delta)$  is

$$\frac{d(U(\Delta))}{dt} = \frac{1}{2} \beta_1 \sum_{i=x,y} \sin(\Delta_i) \dot{\Delta}_i = \beta_1 \sum_{i=x,y} \frac{\sin \Delta_i}{1 + e_i^2} \dot{e}_i, \quad (3.8)$$

where we use the fact  $\dot{\Delta}_i = 2\dot{\theta}_i = \frac{2}{1+e_i^2} \dot{e}_i$ ,  $i = x, y$ .

Considering  $\dot{\mathbf{e}} = \frac{\partial \mathbf{e}}{\partial \mathbf{q}} \dot{\mathbf{q}}$  and if  $\dot{\mathbf{q}} = \mathbf{v}^d$  given by (3.4), we have

$$\dot{\mathbf{e}} = \begin{bmatrix} \frac{\partial e_x}{\partial x} & \frac{\partial e_x}{\partial y} \\ \frac{\partial e_y}{\partial x} & \frac{\partial e_y}{\partial y} \end{bmatrix} \mathbf{v}^d = -\lambda_2 \begin{bmatrix} \sin \Delta_x \\ \sin \Delta_y \end{bmatrix} - \lambda_3 \begin{bmatrix} \hat{e}_x \\ \hat{e}_y \end{bmatrix}. \quad (3.9)$$

Using error prediction (3.5), i.e.,  $\hat{\mathbf{e}} = \alpha_1 \mathbf{e} + \alpha_2 \dot{\mathbf{e}}$ , (3.9) is written as

$$\dot{\mathbf{e}} = -\lambda_2 \begin{bmatrix} \sin \Delta_x \\ \sin \Delta_y \end{bmatrix} - \lambda_3 (\alpha_1 \mathbf{e} + \alpha_2 \dot{\mathbf{e}})$$

and thus, we obtain

$$\dot{\mathbf{e}} = -\frac{1}{1 + \alpha_2 \lambda_3} \left( \lambda_2 \begin{bmatrix} \sin \Delta_x \\ \sin \Delta_y \end{bmatrix} + \alpha_1 \lambda_3 \mathbf{e} \right). \quad (3.10)$$

Plugging (3.10) into (3.8), we obtain

$$\frac{d(U(\Delta))}{dt} = \frac{-\beta_1}{1 + \alpha_2 \lambda_3} \sum_{i=x,y} \left( \frac{\lambda_2 \sin^2 \Delta_i}{1 + e_i^2} + \frac{\alpha_1 \lambda_3 e_i \sin \Delta_i}{1 + e_i^2} \right).$$

Noticing that  $e_i \sin \Delta_i = \tan \theta_i \sin 2\theta_i = 2 \sin^2 \theta_i$  for  $i = x, y$ , the above equation becomes

$$\frac{d(U(\Delta))}{dt} = \frac{-\beta_1}{1 + \alpha_2 \lambda_3} \sum_{i=x,y} \frac{\lambda_2 \sin^2 \Delta_i + 2\alpha_1 \lambda_3 \sin^2 \theta_i}{1 + e_i^2} \leq 0 \quad (3.11)$$

for uniformly positive  $\lambda_2 > 0$  and positive  $\lambda_3, \beta_1, \alpha_1, \alpha_2$ . The result (3.11) implies that  $U(\Delta)$  converges and thus  $\Delta$  converges to a critical point of  $U(\Delta)$ , i.e.,  $\theta = 0$ . Since  $\mathbf{e} = \tan \theta$ , we have  $x \rightarrow x_d$  and  $y \rightarrow y_d$  and this completes the proof.  $\square$

**Remark 3.1.** *The number of elements in  $\mathcal{E}_b(P)$  is 16 and the most influential electrodes for electric field  $\mathbf{E}_p$  are those in  $\mathcal{E}_a(P)$ , which contains only 4 electrodes. Therefore, obtaining control  $\mathbf{u}^*$  by searching solution in (3.7) is not computationally expensive. It is also noted that the powered-“on” electrodes (i.e.,  $\mathbf{u}^*$ ) can switch between any consecutive steps. The directions of desired velocity  $\mathbf{v}^d(k)$  and EP-induced velocity  $\mathbf{v}_c(k)$  might not align each other perfectly. Therefore, as shown in experiments in Section 3.5, the nanowire motion trajectories show zigzag patterns.*

## 3.4 EP-based nanowire motion planning

### 3.4.1 Optimal trajectory property

As discussed in Section 2.4,  $\mathbf{E}_p$  is only determined by the 16 electrodes in  $\mathcal{E}_b(P)$ . The motion-planning problem thus becomes to determine “on” or “off” status of these 16 electrodes. However, searching all of the  $2^{16}$  possibilities of binary control of electrodes in  $\mathcal{E}_b(P)$  is prohibitive due to high computational cost. Therefore, we shall use

the properties of the motion trajectory to simplify the searching process. It is noted that when an electrode is turned “on”, the generated electric field is symmetric about all of the horizontal, vertical and diagonal directions around the electrode. Such symmetry property is used to simplify the planning complexity.

We first introduce some geometry concepts to facilitate the illustration of the motion planning algorithms. Figure 3.1 shows the schematic of the motion planning of a nanowire from starting point  $S$  and to target point  $T$ . Let us consider the atomic electrode set  $\mathcal{E}_a = \{S, Q, R, G\}$  in the figure.

**Definition 3.1.** *A mirror of  $\mathcal{E}_a$  is a line segment connecting any pair of vertices of  $\mathcal{E}_a$  or any of the middle points of each side of  $\mathcal{E}_a$  with its center. A mirror line is the straight-line combined by co-linear mirrors.*

For example, for the atomic cell  $\mathcal{E}_a = \{S, Q, R, G\}$ , lines  $SW$ ,  $WG$ ,  $GV$ ,  $VR$ ,  $RU$ ,  $UQ$ ,  $QT$ ,  $TS$ ,  $SO$ ,  $OR$ ,  $QO$ ,  $OG$ ,  $OW$ ,  $OV$ ,  $OU$  and  $OT$  are all mirrors of  $\mathcal{E}_a$ ; mirrors  $QO$  and  $OG$  are on the same mirror line  $QG$ .

We define the *control line* as the straight line connecting the nanowire current location and target point  $T$  and the *cut line* as the line perpendicular to the control line and passing the nanowire current position. For example, lines  $ST$  and  $nn'$  are the control line and the cut line, respectively, for the starting and target points  $S$  and  $T$  as shown in Figure 3.1. Line  $nn'$  divides all electrodes into two groups. The electrodes in the half plane  $HIJKL$ , as shown the shaded area in the figure, are the power sources that drive the nanowire toward  $T$  and we define them as *target power electrodes* and denote as  $\mathcal{E}_T$ .

Due to symmetry of the electric field in  $\mathcal{E}_a$ , it is straightforward to obtain the following property:

**Property 3.1.** *For any given trajectory  $\mathcal{P}$  in  $\mathcal{E}_a$ , we can always find an alternative electrode control such that a dual trajectory  $\mathcal{P}'$  achieves the same travel time as that of  $\mathcal{P}$  where  $\mathcal{P}'$  is symmetric with  $\mathcal{P}$  about mirror lines of  $\mathcal{E}_a$ .*



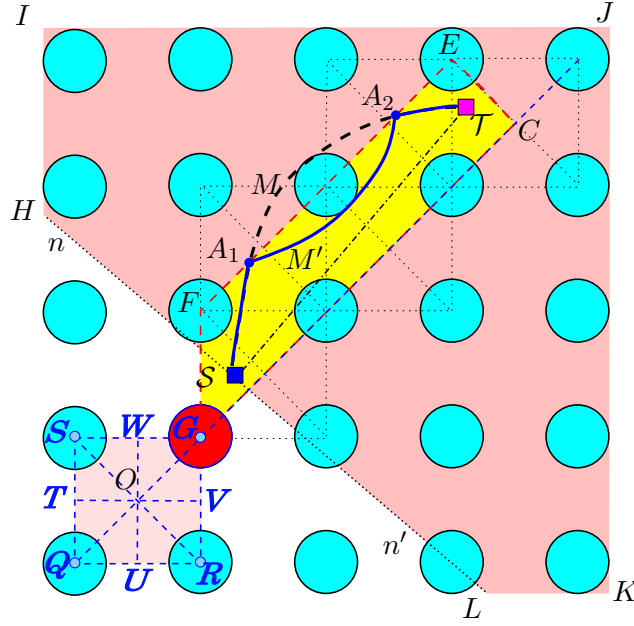


Figure 3.1: Illustrative schematic of the trajectory search area.

With the above observation, the minimum time trajectory from  $\mathcal{S}$  to  $\mathcal{T}$  satisfies the following properties:

**Lemma 3.2.** *The minimum-time trajectory can avoid passing across one mirror line twice.*

*Proof.* As shown in Figure 3.1, suppose that the minimum-time trajectory  $\widehat{A_1 M A_2}$  passes across the mirror line  $\widehat{A_1 A_2}$  twice. By Property 3.1, it is straightforward to find that an alternative trajectory  $\widehat{A_1 M' A_2}$ , symmetric with  $\widehat{A_1 M A_2}$  with respect to mirror line  $\widehat{A_1 A_2}$ , gives the same time as  $\widehat{A_1 M A_2}$ . Therefore, the minimum time trajectory can be instead chosen as  $\widehat{A_1 M' A_2}$  to avoid across line  $\widehat{A_1 A_2}$  twice. This completes the proof.  $\square$

We now define a *trajectory search area*  $\mathcal{A}_m$  as follows:

**Definition 3.2.** *Trajectory search area  $\mathcal{A}_m$  is the convex hull whose boundaries are formed by the mirror lines. Moreover,  $\mathcal{A}_m$  contains all the mirrors that intersect with the control line. If the control line passes through intersection points of mirrors, then take all the intersected mirrors on both sides of the control line into  $\mathcal{A}_m$ ; if the control*

line coincides with any mirrors, then only mirrors lie in either half side of the control line are considered into  $\mathcal{A}_m$ .

Using the results in Lemma 3.2, we have the following property about the minimum-time trajectory:

**Lemma 3.3.** *The minimum-time trajectory from  $\mathcal{S}$  to  $\mathcal{T}$  is located inside  $\mathcal{A}_m$ .*

*Proof.* Due to the page limit, we only present the sketch of the proof here. Since  $\mathcal{A}_m$  is convex and its boundaries are formed by the mirror lines, each vertex point, say  $B$ , of  $\mathcal{A}_m$  has only three possible inner angles:  $135^\circ$ ,  $90^\circ$ , or  $45^\circ$ , as shown in Figs. 3.2(a)-3.2(c), respectively. Suppose that a portion of the optimal trajectory is outside  $\mathcal{A}_m$ . We consider the above-mentioned three cases.

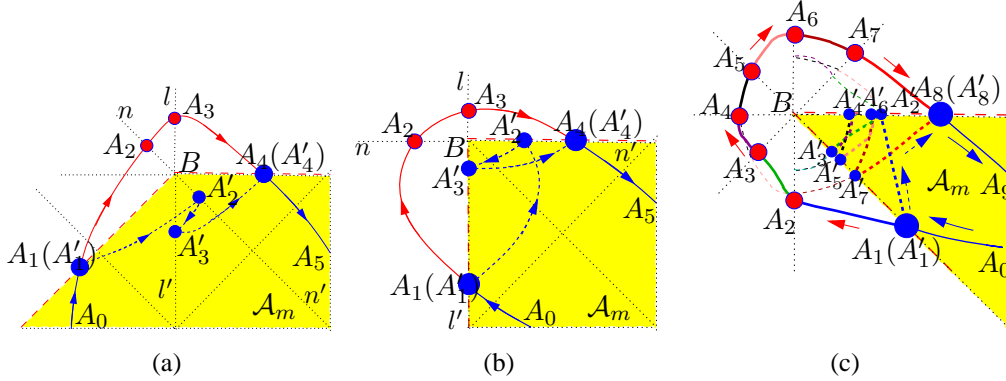


Figure 3.2: Schematic of time-equivalent trajectory within  $\mathcal{A}_m$ . (a) Vertex  $B$  with  $135^\circ$ -deg inner angle. (b) Vertex  $B$  with  $90^\circ$ -deg inner angle. (c) Vertex  $B$  with  $45^\circ$ -deg inner angle.

For the first two cases as shown in Figs. 3.2(a) and 3.2(b), let  $\widehat{A_1 \cdots A_4}$  denote the minimum time trajectory outside  $\mathcal{A}_m$ . Since boundaries  $\widehat{A_1 B A_4}$  of  $\mathcal{A}_m$  are the mirror lines,  $\widehat{A_1 \cdots A_4}$  intersects two other mirror lines  $nn'$  and  $ll'$  at  $A_2$  and  $A_3$ , respectively. By Lemma 3.2, there exist alternative minimum-time trajectories  $\widehat{A'_1 A'_2}$  and  $\widehat{A'_4 A'_3}$  that are symmetric with  $\widehat{A_1 A_2}$  and  $\widehat{A_3 A_4}$  about  $A_1 B$  and  $A_4 B$ , respectively. Without loss of generality, we assume that both  $\widehat{A'_1 A'_2}$  and  $\widehat{A'_4 A'_3}$  are located inside  $\mathcal{A}_m$  because the symmetry lines are the boundaries of  $\mathcal{A}_m$  (if only partials of  $\widehat{A'_1 A'_2}$  and  $\widehat{A'_4 A'_3}$  are in  $\mathcal{A}_m$ , applying the similar symmetry multiple times will lead to completely inside  $\mathcal{A}_m$

as explained in third case). Moreover, there also exists an alternative trajectory  $\widehat{A'_2 A'_3}$  in  $\mathcal{A}_m$  that gives the same travel time as the rest portion  $\widehat{A_2 A_3}$  of  $\widehat{A_1 \cdots A_4}$ . Therefore, we find an alternative minimum-time trajectory in  $\mathcal{A}_m$  that achieves the same time.

For the last case shown in Figure 3.2(c), a similar process to the above described can be applied but more complicated procedure is needed to find an alternative minimum-time trajectory inside  $\mathcal{A}_m$ . First, we partition the outside- $\mathcal{A}_m$  portion of the minimum-time trajectory  $\widehat{A_1 \cdots A_8}$  into seven pieces by their intersections with mirror lines at vertex point  $B$ ; see Figure 3.2(c). For each portion  $\widehat{A_i A_{i+1}}$ ,  $i = 1, \dots, 7$ , a corresponding  $\widehat{A'_i A'_{i+1}}$  can be found by mapping symmetrically around the mirror lines multiple times such that  $\widehat{A'_i A'_{i+1}}$  generates the same travel time for nanowire motion. Thus, similar to the above cases, the minimum-time trajectory can be instead chosen as  $A'_1 \cdots A'_8$  inside  $\mathcal{A}_m$ . This completes the proof.  $\square$

For a given pair of starting and target points  $\mathcal{S}$  and  $\mathcal{T}$ , Algorithm 2 describes the computational approach to find  $\mathcal{A}_m$ . The algorithm takes the intersection of the diagonal parallelogram  $\mathcal{A}_d$ , anti-diagonal parallelogram  $\mathcal{A}_a$ , and rectangle  $\mathcal{A}_r$  areas. All of these parallelograms or rectangles are computed through finding the convex Polygon for sets of lines  $\mathbf{L}_h$  (horizontal with slope  $k = 0$ ),  $\mathbf{L}_v$  (vertical with slope  $k = \infty$ ),  $\mathbf{L}_d$  (diagonal with slope  $k = 1$ ) and  $\mathbf{L}_a$  (anti-diagonal with slope  $k = -1$ ). Function Lineswipe identifies these line sets, and procedure Nearline finds the  $i$ th closest lines  $\mathbb{L}_S$  and  $\mathbb{L}_T$  to points  $\mathcal{S}$  or  $\mathcal{T}$ , with slope  $k$  and passing through any electrodes. Procedure Linecross then determines whether these  $\mathbb{L}_S$  and  $\mathbb{L}_T$  intersect with control line  $\mathbb{L}_c$ . Function Lineswipe identifies the desired line sets by only testing at most six times for  $\mathcal{S}$  and  $\mathcal{T}$ . The intersection of three polygons costs  $O(1)$  since the polygons are either parallelograms or rectangles. Thus, the complexity of the algorithm is  $O(1)$ .

---

**Algorithm 2:** Find trajectory search area  $\mathcal{A}_m$ 


---

**Input :**  $\mathcal{S}, \mathcal{T}$   
**Output:**  $\mathcal{A}_m$   
 $\mathbb{L}_c \leftarrow \text{Line}(\mathcal{S}, \mathcal{T}), \mathbf{L}_h \leftarrow \text{Lineswipe}(\mathcal{S}, \mathcal{T}, 0, \mathbb{L}_c)$   
 $\mathbf{L}_v \leftarrow \text{Lineswipe}(\mathcal{S}, \mathcal{T}, \infty, \mathbb{L}_c)$   
 $\mathbf{L}_d \leftarrow \text{Lineswipe}(\mathcal{S}, \mathcal{T}, 1, \mathbb{L}_c)$   
 $\mathbf{L}_a \leftarrow \text{Lineswipe}(\mathcal{S}, \mathcal{T}, -1, \mathbb{L}_c)$   
 $\mathcal{A}_r \leftarrow \text{Polygon}(\mathbf{L}_h, \mathbf{L}_v), \mathcal{A}_d \leftarrow \text{Polygon}(\mathbf{L}_d, \mathbf{L}_v)$   $\mathcal{A}_a \leftarrow$   
 $\text{Polygon}(\mathbf{L}_a, \mathbf{L}_v), \mathcal{A}_m \leftarrow \mathcal{A}_r \cap \mathcal{A}_d \cap \mathcal{A}_a$   
**function**  $\mathbf{L} = \text{Lineswipe}(\mathcal{S}, \mathcal{T}, k, \mathbb{L}_c)$   
**while**  $i = 1, \dots, 3$  **do**  
     $\mathbb{L}_S \leftarrow \text{Nearline}(k, \mathcal{S}, i)$   
     $\text{IsIntersect1} \leftarrow \text{Linecross}(\mathbb{L}_S, \mathbb{L}_c)$   
    **if**  $\neg \text{IsIntersect1}$  **then** Break  
**end**  
**while**  $i = 1, \dots, 3$  **do**  
     $\mathbb{L}_T \leftarrow \text{Nearline}(k, \mathcal{T}, i)$   
     $\text{IsIntersect2} \leftarrow \text{Linecross}(\mathbb{L}_T, \mathbb{L}_c)$   
    **if**  $\neg \text{IsIntersect2} \ \&\& \ \mathbb{L}_T \neq \mathbb{L}_S$  **then** Break  
**end**  
 $\mathbf{L} = \{\mathbb{L}_S, \mathbb{L}_T\}$

---

### 3.4.2 Motion-planning algorithms

We here present two heuristic planning algorithms by using the properties described in the previous section. For comparison purposes, we also present the planning results by using the well-known  $A^*$  and RRT algorithms.

#### 3.4.2.1 Heuristic algorithm – AllPower

A heuristic algorithm, AllPower, is simply to turn on all the target power electrodes. At each planning step, the algorithm updates the control line and cut line and then, the target power electrodes are all activated. The nanowire is driven by the maximum velocity along the direction towards  $\mathcal{T}$ . Although each target power electrode produces an attractive force towards  $\mathcal{T}$ , the resulting trajectory is not necessarily the shortest time since the travel distance could end up longer than the minimum-time trajectory.

### 3.4.2.2 Heuristic algorithm – MinCost

Another heuristic algorithm, MinCost, considers the cost of every possible combination of power sources. At each planning time step, the algorithm computes the velocity field  $\mathbf{v}_T$  and  $\mathbf{v}_\perp$  along the control-line and cut-line directions, respectively, under any possible combination of target power electrodes. The control  $\mathbf{u}_c$  is obtained by maximizing a cost function that penalizes the ratio of  $|\mathbf{v}_T|$  and  $|\mathbf{v}_\perp| + v_0$ , where  $v_0 > 0$  is a small constant to avoid singularity, namely,

$$\mathbf{u}_c = \arg \max_{e_{ij} \in \mathcal{E}_T} \frac{|\mathbf{v}_T|}{|\mathbf{v}_\perp| + v_0}.$$

Under  $\mathbf{u}_c$ , a large velocity can be obtained along the control-line direction while a small velocity in the cut-line direction.

### 3.4.2.3 $A^*$ pruning

We here modify  $A^*$  algorithm [107] to solve the planning trajectory. In each planning step, the algorithm expands the  $A^*$  graph only in  $\mathcal{A}_m$ . For each expended node, it checks whether the node's parents have passed the mirror lines before: if so, deletes the new node that across the same mirror line. Meanwhile, if the new node's position has been explored previously, then the algorithm compares the cost of each trajectory that arrives at that same position, prunes the graph by deleting the higher cost node and reconnects the deleted node's children to the lower cost node. Finally, the algorithm sorts the cost of each node in the open list of the  $A^*$  graph and drives the nanowire using the least cost. For nanowire  $P(x, y)$ , the (time) cost function is defined as

$$T_c(P) = \frac{\text{dist}(\mathcal{T}(x, y), P(x, y))}{v_{\max}} + T(P(x, y)), \quad (3.12)$$

where  $\text{dist}(\cdot, \cdot)$  defines the distance between two points,  $v_{\max}$  is the possible maximum velocity of the nanowire,  $T(P(x, y))$  is the travel time to reach point  $P(x, y)$ , and  $\mathcal{T}(x, y)$  is the target point. It is straightforward to obtain that the cost function never overestimates the minimum time.

#### 3.4.2.4 Breadth-first search (BFS)-based planning

With a fixed planning time step, we build trajectory paths under all possible combinations of powered-“on” electrodes and then a graph is constructed using all possible trajectory paths. A breadth-first search (BFS) method is used to build a searching tree to obtain the optimal results. Similar to the  $A^*$  algorithm, only the trajectories within  $\mathcal{A}_m$  are used in the searching process, and mirror-line checking and cost-pruning are also used in this algorithm. At a fixed planning time step, BFS yields the optimal time result when all the time costs of expanding nodes are equal because it always expands the shallowest unexpanded node. Therefore, we will use BFS as the benchmark to compare various planning algorithms.

#### 3.4.2.5 RRT pruning

By modifying the sampling based search algorithm [107], the RRT-pruning algorithm only samples points inside  $\mathcal{A}_m$ , enforces the mirror-line checking and employs the cost-pruning technique as those in the  $A^*$  pruning algorithm to steer the nanowire from the current position to the new nodes and then connect them back to the RRT trees.

### 3.5 Experimental results

#### 3.5.1 Experimental setup

Figure 3.3(a) shows the experimental setup for nanowire motion control and manipulation test. A microfluidic device (Figure 3.3(c)) with  $2 \times 3$  electrode arrays was fabricated on glass and mounted on a PCB connector as shown in Figure 3.3(b). The distance between centers of adjacent electrodes is  $L = 1200 \mu\text{m}$  and the diameter of each circular electrode is  $L/2 = 600 \mu\text{m}$ . A top coverslip coated with an indium tin oxide (ITO) layer is used to cover the microfluidic device and as an additional electrode to control the vertical position of the nanowires and deposit them onto the

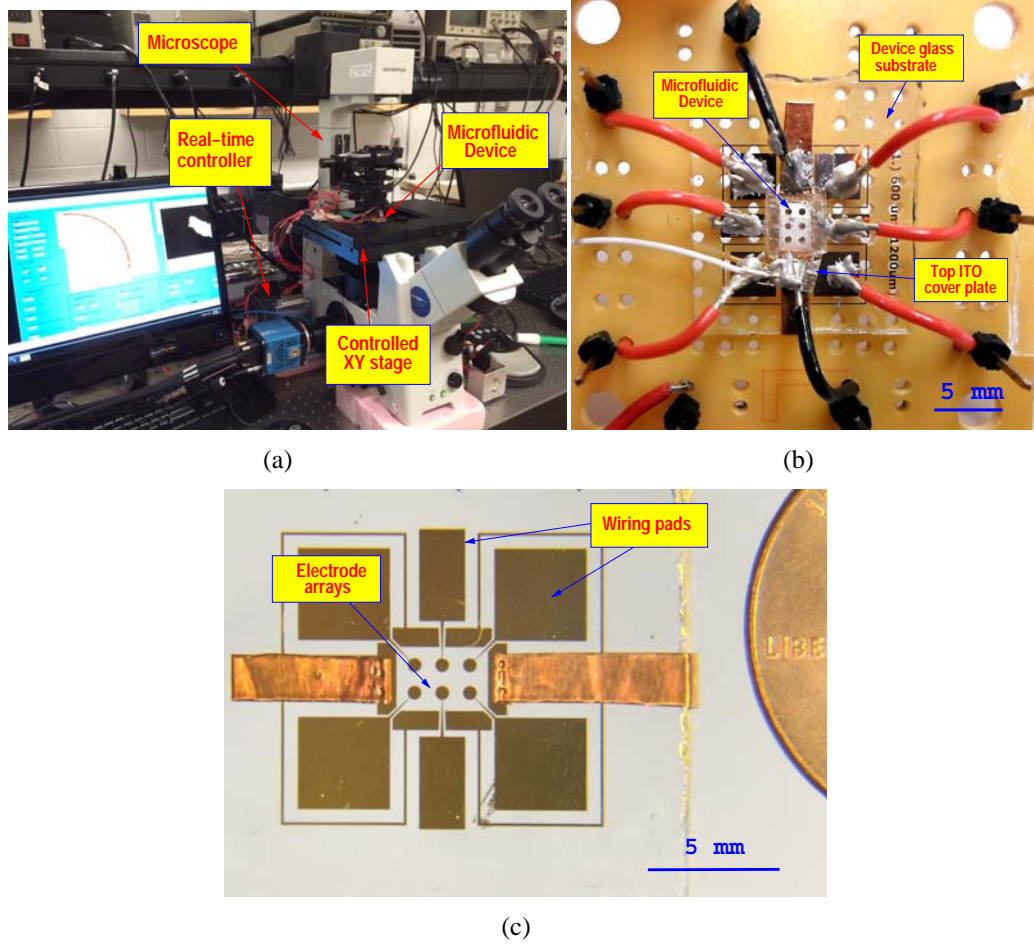


Figure 3.3: The experimental setup. (a) The inverted microscope setup with embedded control systems and vision-based nanowire motion feedback. (b) The glass microfluidic device is mounted on a PCB for testing and a top coverslip coated with an indium tin oxide (ITO) layer is placed to cover the device. (c) The top view of the microfluidic device with  $2 \times 3$  electrode arrays.

bottom surface of the device. An inverted optical microscope (Olympus IX71) with a monochrome CCD camera (PCO AG pco.edge  $2560 \times 2160$  pixels) is used to capture and feedback the nanowire trajectory. The PCB connector board is mounted on a motorized, computer-controlled XY stage (Prior ProScan III). An embedded system (NI cRIO 9074) is used to control the electrode array and a LabView application is developed to process the vision feedback of nanowire positions. Using a voltage source and an amplifier, a 100 (–100) V DC potential is selectively applied to the electrode array.

We use metal-assisted chemical etched silicon nanowires suspended in heavy viscosity mineral oil at a concentration of 0.5 mg/ml. Figure 3.4(a) shows a forest of

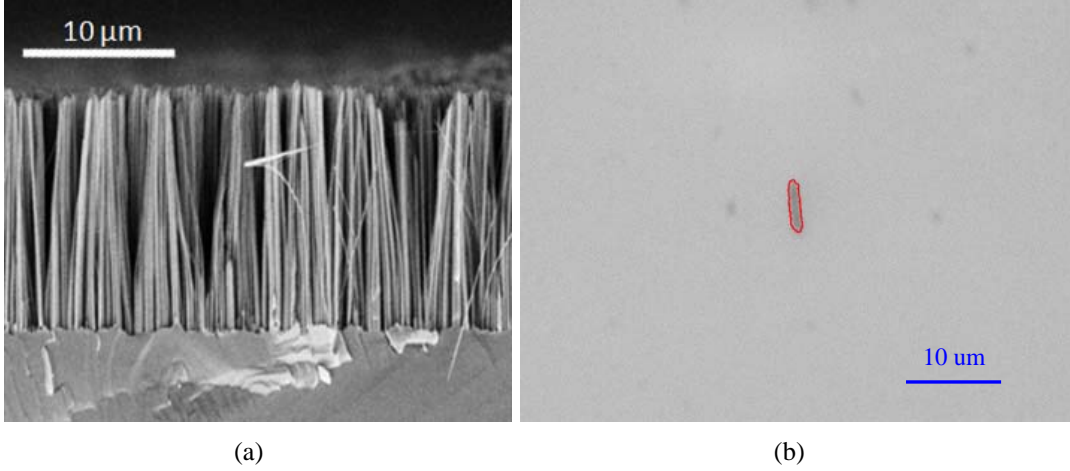


Figure 3.4: (a) SEM image of as-grown silicon nanowires used in experiments. (b) The nanowire image under microscope and the processed contour for positioning feedback.

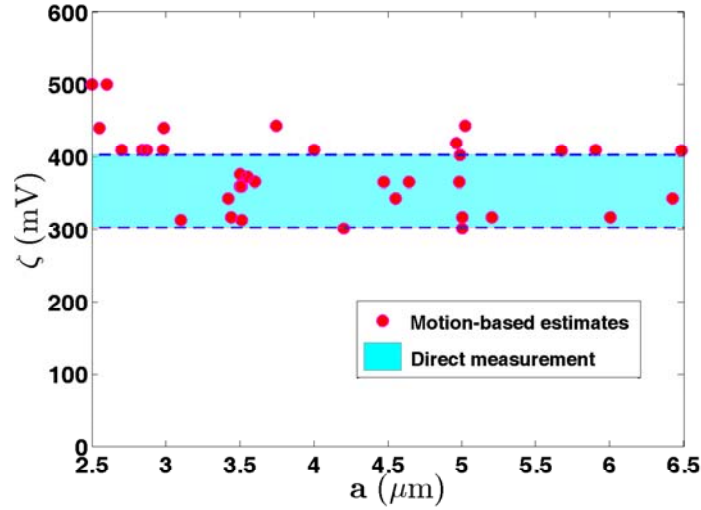


Figure 3.5: Comparison of estimated and measured values of zeta-potential among a total of 35 silicon nanowires.

the silicon nanowires fabricated for the experiments and Figure 3.4(b) shows an image of an individual nanowire suspended in the oil, with the extracted contour information by vision algorithms for positioning feedback. The values of the model parameters of the nanowire used in motion control design are as follows:  $\mu = 251.2$  cP,  $\epsilon_m = 2.17\epsilon_0$ ,  $a = 2$  to  $7 \mu\text{m}$ ,  $b = 100$  nm, and sampling time  $\Delta t = 0.5$  s. We use the known electric fields and nanowire motion trajectories to infer the values of particle zeta-potential  $\zeta$  in (2.4). Figure 3.5 plots the motion-based estimates of the  $\zeta$  values for each of 35 silicon nanowires. The shaded area of Figure 3.5 shows the range of



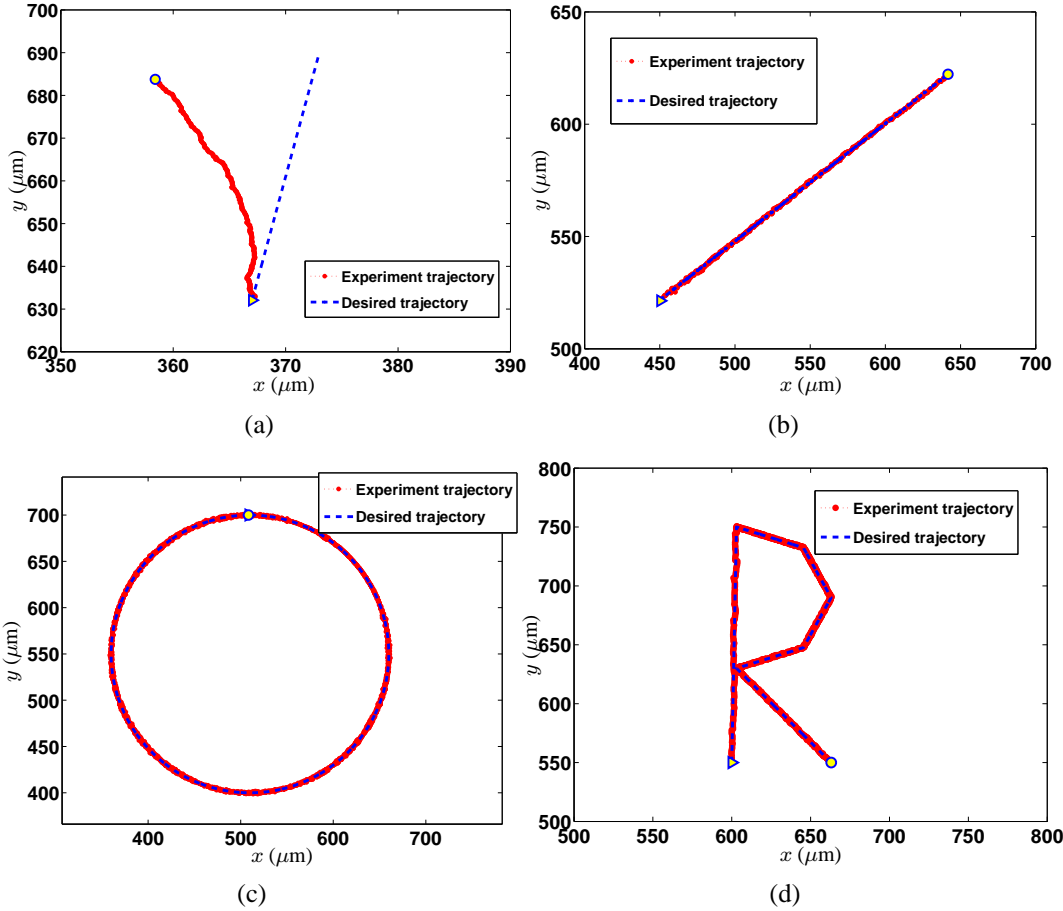


Figure 3.6: Trajectory tracking performance. (a) EP model-based nanowire motion control of a straight-line trajectory without disturbance compensation. (b) Disturbance-compensated following a straight-line path. (c) Disturbance-compensated following a circular path. (d) Disturbance-compensated following an “R”-shape path. In all plots, the triangular and empty circular marks indicate the starting and ending points, respectively, of the nanowire trajectory.

zeta-potentials independently measured for an identical silicon nanowire/oil suspension using a Brookhaven ZetaPALS instrument. This consistency of the calculated and measured zeta potentials indirectly confirms the basic model of the nanowire dynamics and electric fields described in Sections 2.3 and 2.4.

### 3.5.2 Nanowire motion-control results

Figure 3.6 shows the motion control and path-following performance for various trajectories. In experiments, we estimated and updated the zeta-potential values for the

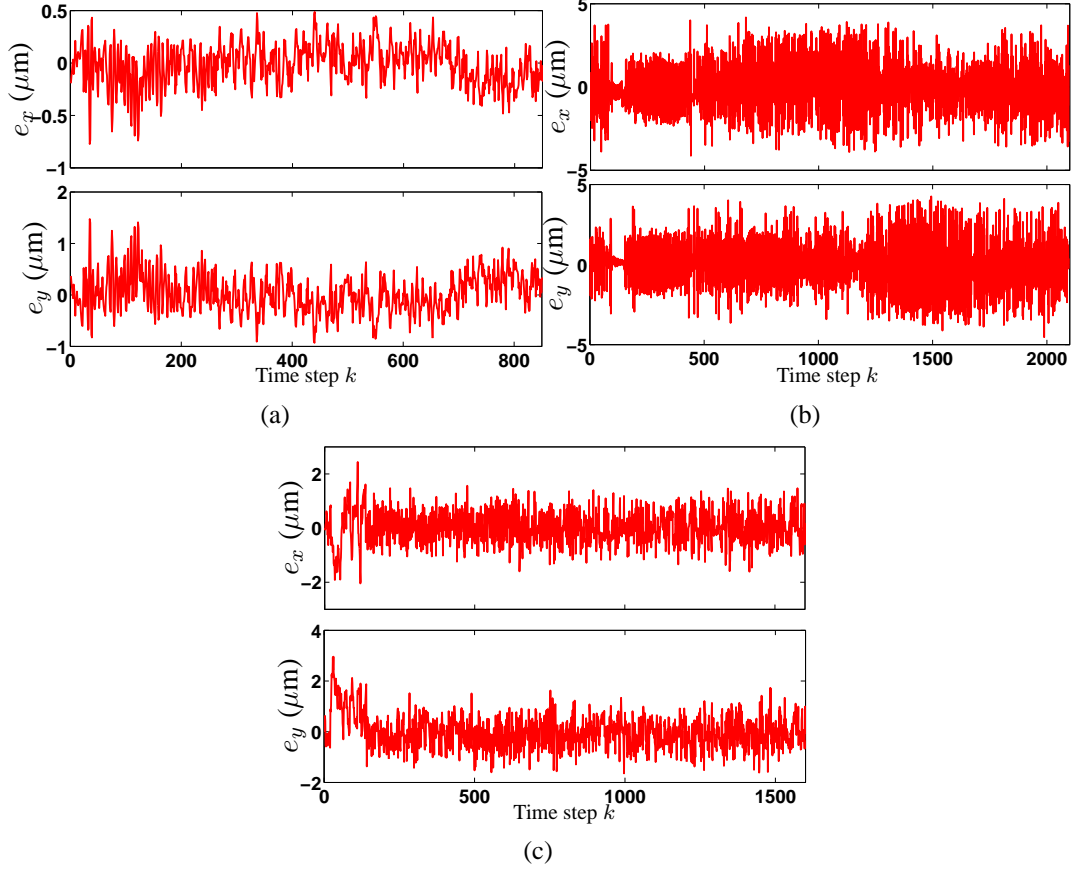


Figure 3.7: Trajectory-tracking errors. (a) Errors for a straight-line trajectory. (b) Errors for a circular trajectory. (c) Errors for an “R”-shape trajectory.

nanowire using the motion information of the beginning few seconds. To demonstrate the EO effects in experiments, Figure 3.6(a) shows the tracking performance of a straight-line trajectory without disturbance compensating. The motion control of the nanowire shown here is purely based on the EP-model given by (2.4). More EO flow disturbed motion results are presented in [78]. Clearly, the EO flow disturbance affects the nanowire motion significantly.

Under the motion control (3.4), Figure 3.6(b)-3.6(d) shows the path-following performance of a straight-line, a circular and an “R”-shape trajectory, respectively. Figure 3.7 shows the positioning errors for these three trajectories. The errors are consistently within  $4 \mu\text{m}$  over a few hundred micrometers range driving distance. For the straight-line following (Figs. 3.6(b) and 3.7(a)), the tracking errors are within  $1 \mu\text{m}$  most of the time. The plots in these two figures confirm that the motion control design

can steer the nanowire (around  $8\ \mu\text{m}$  long) to follow a given path with an average error around  $2\text{-}4\ \mu\text{m}$ .

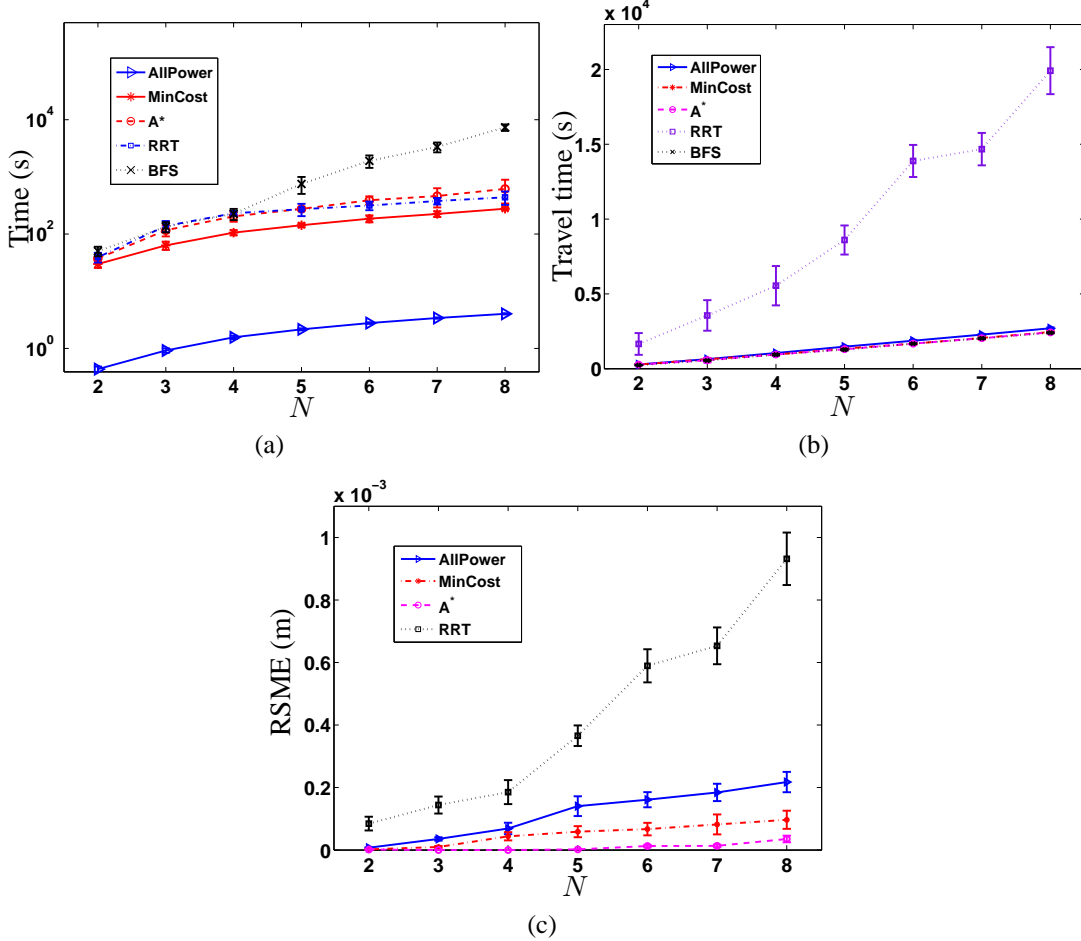


Figure 3.8: Performance comparison among various motion planning algorithms on an  $N \times N$  electrode array. (a) Computation time (mean and standard deviation). (b) Nanowire travel time. (c) RMSE (benchmarked with the BFS results).

### 3.5.3 Motion-planning results

We first use simulation to demonstrate and compare the performance of the various motion-planning algorithms. For an  $N \times N$  electrode array, we first select the locations of starting and target points  $\mathcal{S}$  and  $\mathcal{T}$ . Depending on the size  $N$ , we choose the locations  $\mathcal{S}$  and  $\mathcal{T}$  randomly such that the distance between them is at least  $\frac{\sqrt{2}}{2}L$  for  $N = 2$  and  $\sqrt{2}(N - 2)L$  for  $N = 3, \dots, 8$ . To eliminate the performance variation, we conduct 10 runs for each algorithm and then compute the statistics of these simulation runs.

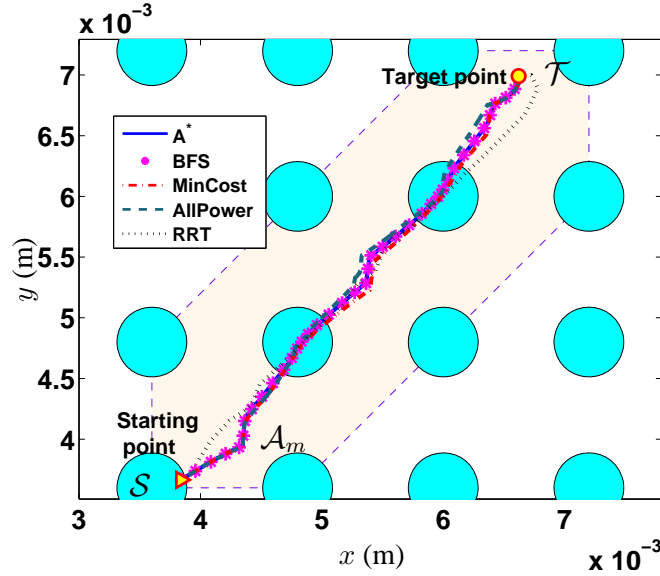
Figure 3.8(a) shows the comparison results of the computation time, while Figs. 3.8(b) and 3.8(c) show the planned travel time for nanowires and the root mean square errors (RMSE) of the trajectories benchmarked by the BFS algorithm. From the results shown in the figure, the computation time of the BFS algorithm increases exponentially with dimension  $N$ . The complexity of the  $A^*$ , RRT and MinCost algorithms are similar. The heuristic algorithm AllPower shows the best complexity performance among all algorithms. The traveling time and accuracy confirm a similar observation: RRT shows the worst results and all other algorithms demonstrate similar good performance.

Figure 3.9 shows the planning trajectories by various algorithms for a  $4 \times 4$  electrode array. For clarity, the starting and target points and search area  $\mathcal{A}_m$  are marked in the figure. Table 3.1 lists the travel time, RMSE and  $R^2$  comparisons. Again, the RMSE and  $R^2$  results in the table are benchmarked with the BSF algorithm. From these results, we observe that: (1)  $A^*$  shows superior accuracy performance compared to the other three algorithms; (2) the heuristic algorithms such as MinCost and AllPower show similar accuracy and traveling-time performance. These two algorithms show superior accuracy than that of RRT; (3) all algorithms demonstrate similar path trajectories, except that the trajectory by RRT shows some significant deviations; and (4) the RRT algorithm takes significantly much more time than any of the other algorithms. In summary, the two heuristic algorithms, particularly AllPower, clearly outperform the other three planning approaches in complexity, and yield comparable travel time and accuracy. The heuristic algorithms are less computationally expensive than the  $A^*$  and RRT algorithms since they require less or no searching actions in each time step. Although the heuristic algorithms cannot guarantee optimality, they yield comparable travel time and accuracy performance from both the simulation and experimental results.

Figure 3.10 shows the motion-planning experiments. In the figure, a silicon nanowire was driven from points  $\mathcal{S}$  to  $\mathcal{T}$  across the line connecting two electrode centers. Two motion planning algorithms, BFS and AllPower, are implemented. We chose the

Table 3.1: Performance comparisons for the example shown in Figure 3.9

	BFS	AllPower	MinCost	$A^*$	RRT
Travel time (s)	947	1062	1046	950	6875
RMSE	N/A	$6.9 \times 10^{-5}$	$5.9 \times 10^{-5}$	0	$1.4 \times 10^{-4}$
$R^2$	N/A	0.995	0.996	1	0.978

Figure 3.9: Comparison of the nanowire trajectories under different motion planning algorithms using a  $4 \times 4$  electrode array.

AllPower algorithm here because it outperforms the other algorithms in both complexity and travel time as demonstrated previously, while the BFS is used as a benchmark for the optimal trajectory. The BFS-based motion trajectory was obtained offline due to the high computational cost. For the AllPower algorithm, the motion planning and control were conducted online. It is clearly shown in the figure that both algorithms give almost the same trajectory path. The zoom-in subplot in Figure 3.10 shows that the AllPower trajectory follows closely to the BFS planned trajectory and both algorithms have demonstrated a zigzag pattern motion due to the switching of powered-“on” electrodes at consecutive time steps.

It is interesting to observe that both the BFS and AllPower algorithms generate a similar trajectory that is not the shortest distance between points  $S$  and  $T$ .

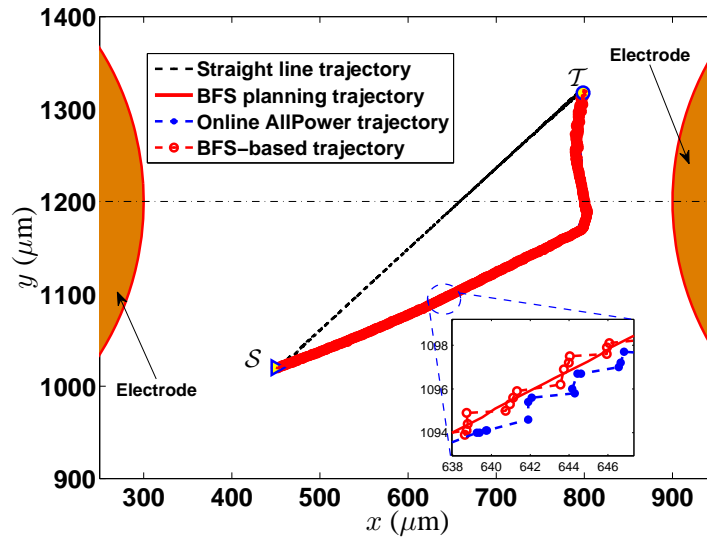


Figure 3.10: Experimental silicon nanowire trajectories under BFS and AllPower. Note that the straight-line trajectories shown for comparison is not the minimum-time trajectory.

For comparison, we also implemented a motion planning and control design that follows the straight-line (shortest distance) trajectory between  $S$  and  $T$  as shown in Figure 3.10. The travel times from  $S$  to  $T$  are 1180 s, 993 s, and 977 s for the straight-line, AllPower and BFS algorithms, respectively. Clearly, the shortest-distance trajectory does not demonstrate the shortest time. This is because that the nanowire motion is determined by the electric-field direction and magnitude. The velocity magnitude is larger along the BFS and AllPower trajectories than along the straight-line trajectories. In particular, since the strength of electric field is inversely proportional to the square of the distance between the particle and electrodes, the nearby electrodes have much more significant impact on the nanowire motion than that of far-away electrodes. As a result, in the AllPower and BFS trajectories, the nanowire moves rapidly in the horizontal direction when the nearby electrodes are powered on, and then more slowly (but for a shorter distance) when they are turned off. Overall, the velocity of the AllPower trajectory is significantly larger than that of the straight-line trajectory. Therefore, the fastest trajectory is not always along the shortest distance between two points.

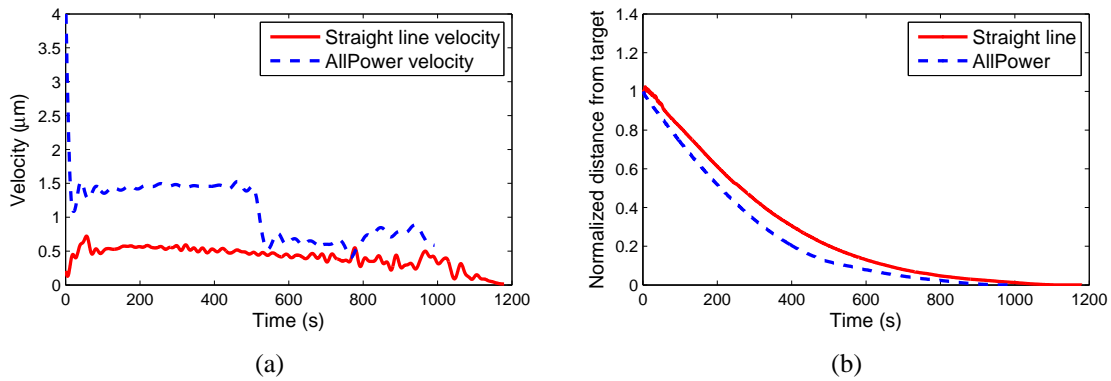


Figure 3.11: (a) Velocity profiles corresponding to the ALLPOWER and the straight-line trajectories. (b) Normalized distance from target point corresponding to the ALLPOWER and the straight-line trajectories.

### 3.5.4 Steering and manipulating nanowires

In this section, we demonstrate the use of the motion planning and control design for 3D nanowire manipulation. We first demonstrate how to steer, orient and deposit a single nanowire on the device substrate and then present the sequential manipulation and deposition of multiple nanowires.

Figure 3.12 illustrates a sequence of snapshots of steering, orientation and manipulation of a single nanowire from location *A* in fluid suspension to location *B* on device substrate surface. First, the nanowire was steered from *A* to *B* by the AllPower and motion control algorithms (Figure 3.12(a) and 3.12(b)). Then, by turning on the ITO electrode on the top plate, an electric field along the vertical (*z*-axis) direction was generated such that the nanowire was aligned vertically and moving towards the bottom surface (Figure 3.12(c)). Finally, once the nanowire reached the surface, the ITO electrode was turned off and the electrodes on the bottom surface were turned on again to re-orient and deposit the nanowire on the substrate in the desired direction, as shown in Figure 3.12(d). Due to change in the focal plane of the microscope for the images, several other nanowires and objects on the bottom surface that are seen clearly in Figure 3.12(d) are not seen in the other images. Figure 3.12(e) shows the overall trajectory of the nanowire by overlaying the image sequence that is shown in part in

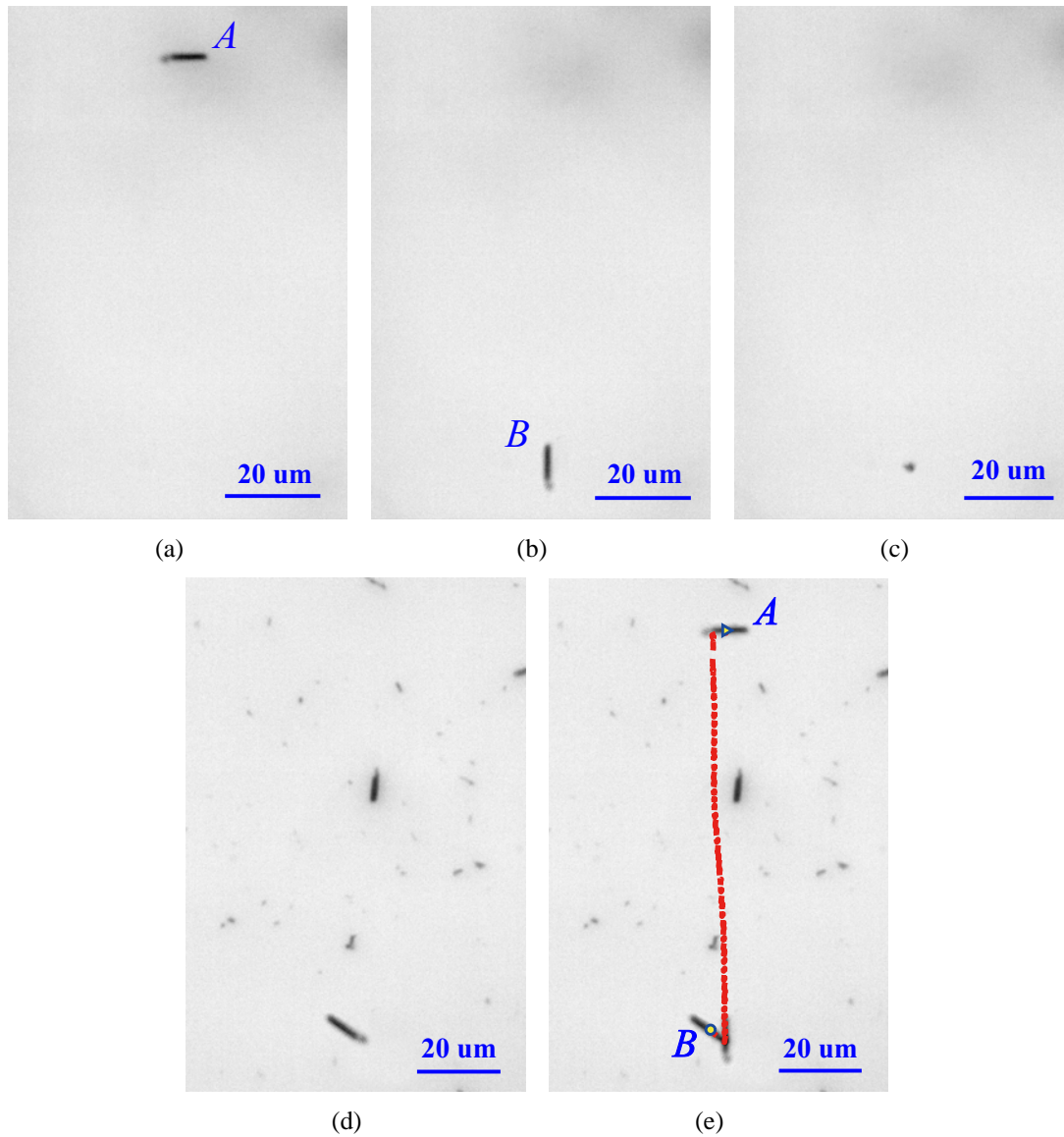


Figure 3.12: Vertical positioning and deposition of a single nanowire on the device substrate. (a) nanowire at location *A*. (b) Nanowire is steered to location *B* by AllPower algorithm. (c) Using the top ITO electrode, the nanowire was aligned along the vertical direction and steered to touch the bottom surface. (d) By turning the electrode again, the nanowire was re-orient and deposited on the substrate surface with the desired orientation. (e) Overlay trajectory of the entire nanowire motion. The triangular and empty circular marks indicate the starting and ending points of the nanowire.

Figs. 3.12(a)-3.12(d).

Figure 3.13 further demonstrates the use of the EP-based motion control and manipulation to sequentially steer and deposit three individual nanowires to form larger



patterns on the device substrate surface. In Figure 3.13(a), three nanowires were suspended in the fluid in an area of a size of  $50 \times 100 \mu\text{m}^2$ . Then, each of these three nanowires was sequentially steered and transferred to the substrate as shown in Figure 3.13(b) using the procedure discussed above. Once the nanowire is settled down on the bottom substrate, it sticks to the surface due to the Van der Waals interactions. The nanowire position and orientation is no longer changed by the electric field when moving and reorientating the other nanowires. Thus, we can sequentially deposit nanowires head-to-tail to form a longer, straight-line pattern on the substrate surface.

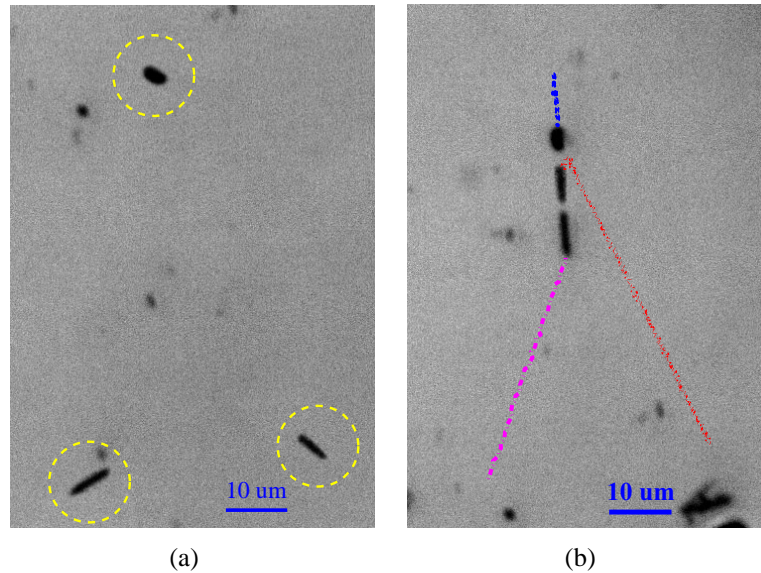


Figure 3.13: Electric-field-based steering and manipulation of three nanowires to form a straight-line on the device substrate. (a) Initial positions of the three nanowires. (b) Final positions of these three nanowires after re-positioning and depositing to align into a straight-line.

Figure 3.14 demonstrates a few more examples of the use of electric-field-based forces to drive and steer multiple nanowires to form more complicated geometric shapes than those in Figure 3.13. Figure 3.14(a) shows the result of moving and depositing six nanowires in a straight line, and Figure 3.14(b) shows the formation of a hexagonal pattern with multiple nanowires, while Figure 3.14(c) demonstrates cross patterns formed by depositing three nanowires perpendicularly on top of three other

aligned nanowires. These experiments further confirm the feasibility of using electric-field-based manipulation for fabricating functional nanodevices using nanowires and nanotubes.

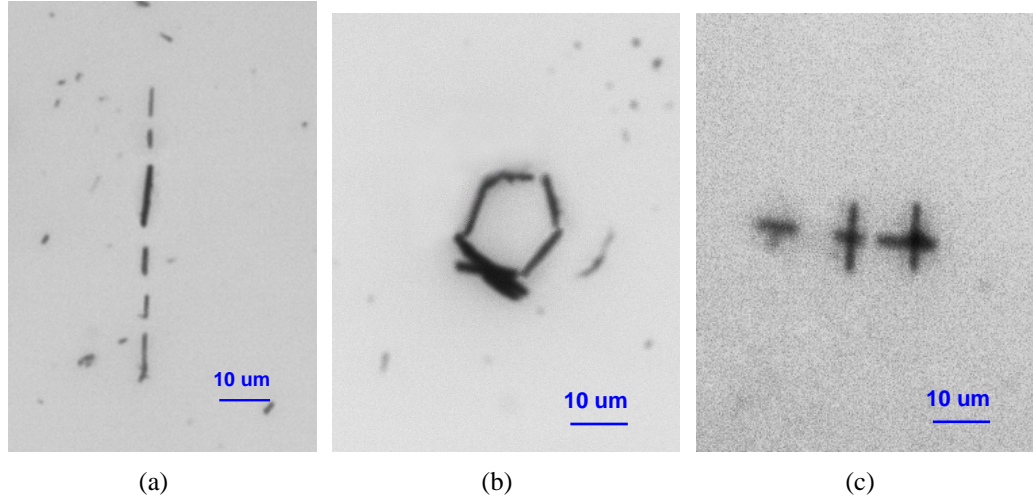


Figure 3.14: Electric-field-based steering and manipulation of multiple nanowires to form (a) a straight-line, (b) hexagonal and (c) three cross-shape patterns on the device substrate.

### 3.6 Conclusion

This chapter presented electric-field-based motion control, planning and manipulation of individual nanowires in liquid suspension. The motion-planning-and-control schemes take advantages of the symmetry of the electric field generated by the electrodes. A superposition approach was developed to efficiently compute the electric-field distribution for any given set of powered-“on” electrodes. The EP driving force on the particles is modeled, and the vision-based feedback control compensates for un-modeled particle dynamics such as disturbances due to EO flow. The nanowire motion-planning problem is NP hard and we proposed two heuristic algorithms based on the reduced search areas. We compared the heuristic algorithms with other existing motion planning algorithms such as RRT and  $A^*$ . The results showed that the heuristic algorithms significantly reduced the computational complexity while maintained comparable performance with those of the RRT,  $A^*$  and other algorithms. Extensive

experimental results confirmed the analysis and the design of nanowire motion control, planning, and manipulation. Using an additional top electrode, we have also demonstrated the ability to position individual nanowires vertically as well as horizontally and then deposit them in sequence at desired locations on the device substrate.

Based on the result of individual nanowires motion control, planning and manipulation, more systematic control methods to achieve optimal performance, as well as the large-scale motion planning algorithms for simultaneous steering of multiple nanowires in liquid suspension will be presented in the next chapter. The results in this chapter lay a critical foundation for nanomanipulation using EP induced forces.

## **Chapter 4**

# **Simultaneous Multiple-Nanowire Motion Control, Minimum Distance Planning and Manipulation under Electric-Fields in Fluid Suspension**

### **4.1 Introduction**

The automated steering and manipulation of multiple simultaneous nanowires would enable the scalable assembly of nanodevices for a variety of applications. As discussed in Chapter 3, an EP-based motion planning and manipulation scheme was developed to steer and drive a single nanowire in fluid suspension from one location to its targeted position. The motion control designed in Section 3.3 compensated for the EO flow induced by the electric field acting on the fluid. While demonstrating the feasibility, these studies and experiments only dealt with an individual nanowire and cannot be directly applied to multiple nanowires due to the combinatorial complexity and potential collision of the multiple-nanowire problem. Therefore, this chapter presents an electric-field-based design for simultaneous motion planning and control of multiple nanowires in liquid suspension. The design uses a set of electrode arrays, the same electrode design as in Chapter 3, to drive and orient multiple nanowires from their starting locations to targeted locations under electrophoretic forces. The motion control of multiple nanowires in fluid suspension is first presented to steer the nanowires simultaneously along given trajectories. We further provide the control-system properties that capture the relationship between the maximum number of the simultaneously controllable nanowires and the given number of actuated electrodes. A two-stage motion-planning algorithm is then presented to generate the desired trajectories for multiple

nanowires with minimized total travel distances while avoiding collision. We present extensive simulations and experiments to demonstrate the motion planning and control of multiple nanowires to form various geometric patterns. The results will help provide a foundation for scalable, automated methods for manipulating nanowires to build nanodevices.

The main contribution of the work lies in the development and demonstration of the novel efficient and effective motion-planning and control algorithms for simultaneously manipulating multiple nanowires in liquid suspension. The developed algorithms and microfluidic device can potentially enable the scalable assembly of nanodevices for a variety of applications.

The rest of the chapter is organized as follows. We present the problem formulation in Section 4.2. The nanowire-motion-control strategy is proposed in Section 4.3. The motion-planning algorithms are presented in Section 4.4. We then present simulation and experimental results in Section 4.5, and conclude the chapter in Section 4.6.

## 4.2 Problem formulation

Figure 2.1 shows the schematic of the micro-fluidic device, which is a fluid reservoir with  $N \times N$  electrodes array on the bottom surface. The square lattice array of circular electrodes with radius  $R$  is fabricated on a glass substrate with equal distance  $L$  between centers (Figure 2.1(b)). The actual device is shown in Section 4.5.2. Each electrode is independently actuated with different DC voltage. Fluid containing a dilute concentration of nanowires is placed on top of the electrode array. A glass coverslip is used to cover the fluid and form a flow reservoir.

We consider  $n$  nanowires in the 2D work space with a coordinate system defined at the left-bottom corner on device; see Figure 2.1(b). The position of the  $i$ th nanowire  $P_i$  at time  $t$  is denoted as  $\mathbf{r}_i(t) = [x_i(t) \ y_i(t)]^T$ ,  $i = 1, \dots, n$ . For each nanowire  $P_i$ , its starting location is  $\mathbf{r}_{iS}$  and the targeted location is  $\mathbf{r}_{iT}$ . We concatenate the position

vectors of all nanowires as  $\mathbf{q}(t) = [\mathbf{r}_1^T(t) \cdots \mathbf{r}_n^T(t)]^T \in \mathbb{R}^{2n}$  and the sets of starting and target locations as  $\mathcal{S} = [\mathbf{r}_{1S}^T \cdots \mathbf{r}_{nS}^T]^T$  and  $\mathcal{T} = [\mathbf{r}_{1T}^T \cdots \mathbf{r}_{nT}^T]^T$ , respectively.

We define a *path* of time interval  $[t_1, t_2]$ , denoted as  $\pi(\mathbf{q}(t_1), \mathbf{q}(t_2))$ , for all nanowires as the collection of the trajectory of all nanowires. Moreover,  $\mathbf{q}(0) = \mathcal{S}$  to  $\mathbf{q}(t_f) = \mathcal{T}$  for a finite time  $t_f$ . We also define  $\pi^*(\mathcal{S}, \mathcal{T})$  as a collision-free path from  $\mathcal{S}$  to  $\mathcal{T}$  that minimizes a specified cost function. The electrode  $e_{ij}$ , its position  $\mathbf{r}_{e_{ij}}$ , and the electrode control matrix  $\mathbf{u}$  follow the definition as defined in equation (2.1) in Section 2.2.

As discussed in Chapter 2, for nanowire  $P_i$  in Figure 2.4, only powered electrodes in  $\mathcal{E}_b(\mathbf{r}_i)$  influencing the motion of  $P_i$ . Indeed,  $\mathcal{E}_b(\mathbf{r}_i)$  includes all electrodes within an  $r_p$ -array-distance range with respect to  $P_i$ , and  $r_p \in \mathbb{N}$  is the effective radius. It is straightforward to show that  $|\mathcal{E}_b(\mathbf{r}_i)| = 4r_p^2$ , and  $r_p = 2$  for the square lattice arrays from COMSOL simulation.

Followed by the definition of atomic and basic electrode sets, we also define an *atomic cell area*  $\mathcal{A}_a^i$  and a *basic cell area*  $\mathcal{A}_b^i$  of  $P_i$  as the area that are formed by the maximum convex hull of  $\mathcal{E}_a(\mathbf{r}_i)$  and  $\mathcal{E}_b(\mathbf{r}_i)$ , respectively. For example, for  $P_i$  in Figure 4.1 and  $r_p = 2$ ,  $\mathcal{E}_a(\mathbf{r}_i)$  and  $\mathcal{E}_b(\mathbf{r}_i)$  contain the electrodes within squares  $ABCD$  and  $A'B'C'D'$ , respectively, and squares  $ABCD$  and  $A'B'C'D'$  are  $\mathcal{A}_a^i$  and  $\mathcal{A}_b^i$ , respectively. For  $n$  nanowires, we define  $\mathcal{A}_b = \bigcup_{i=1}^n \mathcal{A}_b^i$  and then the effective electrode set  $\mathcal{U}$  should be inside  $\mathcal{A}_b$ . Hopefully without causing any confusion, we abuse the notation to use  $|\mathcal{A}_b^i|$  to indicate the number of electrodes in  $\mathcal{A}_b^i$ .

The nanowire motion is modeled as that of a non-spherical particle immersed in a viscous fluid under external electric field as discussed in Section 2.3. Under a DC electric field, the equation of motion for  $P_i$  is given as

$$\mathbf{v}_i = \dot{\mathbf{r}}_i = \begin{bmatrix} v_{ix} \\ v_{iy} \end{bmatrix} = \frac{\epsilon_m \zeta_i \mathbf{E}_i}{\mu} = C_i \begin{bmatrix} E_{ix} \\ E_{iy} \end{bmatrix}, \quad (4.1)$$

---

\*We here drop the dependency of  $\mathcal{A}_a^i$  and  $\mathcal{A}_b^i$  on position vector  $\mathbf{r}_i$  explicitly for notation clarity.

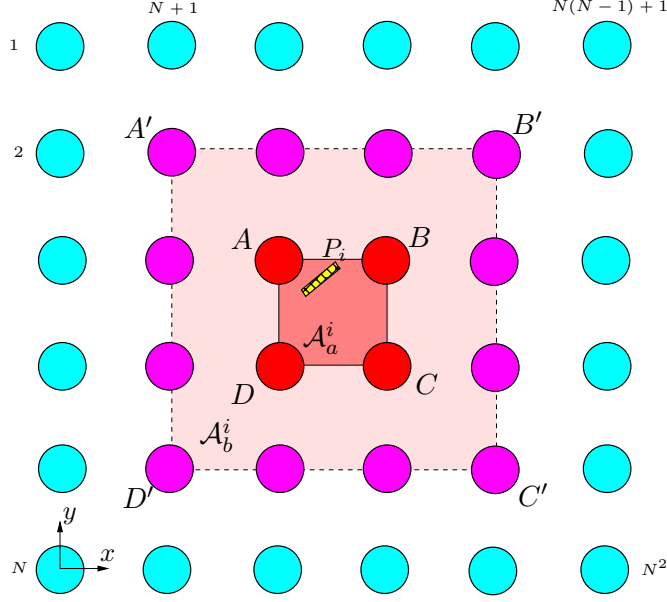


Figure 4.1: A schematic of an atomic and basic areas around nanowire  $P_i$  with a re-indexed electrode order (as one-dimensional array).

where  $\mathbf{v}_i = [v_{ix} \ v_{iy}]^T$  is the  $P_i$ 's velocity vector,  $\mathbf{E}_i = [E_{ix} \ E_{iy}]^T$  is the DC electric-field vector at  $\mathbf{r}_i$ ,  $C_i = \epsilon_m \zeta_i / \mu$ ,  $\mu$  is the dynamic viscosity, and  $\epsilon_m$  is the electric permittivity.  $\zeta_i$  is the zeta-potential of the  $i$ th suspended particle and is estimated online for each nanowire. From (4.1), the electric field is regulated to steer the nanowires' motion by appropriately applying voltage  $\mathbf{u}$  to electrodes. Similar to the electric field calculation in Section 2.3,  $\mathbf{E}_i$  at  $\mathbf{r}_i$  can be calculated by

$$\mathbf{E}_i = \sum_{e_{I_k} \in \mathcal{E}_b(\mathbf{r}_i) \cap U} V_{I_k} \mathbf{E}_k(\mathbf{r}_i), \quad (4.2)$$

where  $\mathbf{E}_k(\mathbf{r}_i)$  is the electric field at  $\mathbf{r}_i$  by only powered-“on” electrode  $e_{I_k} \in \mathcal{E}_b(\mathbf{r}_i) \cap U$  with *unit* voltage and  $V_{I_k}$  is the corresponding voltage that applied.

### 4.3 Motion control of multiple nanowires

The simultaneous control problem aims to compute the electrode voltages to steer all nanowires to follow the given  $\pi^*(\mathcal{S}, \mathcal{T})$ . To formulate the motion equations for all  $n$  nanowires, we first re-index the electrodes into a one-dimensional  $N^2$ -element array

with a column-wise order; see Figure 4.1. We denote the electric field under unit voltage at  $\mathbf{r}_j(t)$  by the powered  $i$ th electrode as  $\mathbf{E}_i(\mathbf{r}_j(t)) = [E_{x_i}(\mathbf{r}_j(t)) \ E_{y_i}(\mathbf{r}_j(t))]^T$ ,  $j = 1, \dots, n$ , and the corresponding controlled electrode voltage as  $\mathbf{u}_c \in \mathbb{R}^{N^2}$ , which is also re-ordered column-wise from  $\mathbf{u}$  in (2.1). By defining a *motion gain matrix*

$$\mathbf{B} = \begin{bmatrix} C_1 \mathbf{E}_1(\mathbf{r}_1(t)) & \cdots & C_1 \mathbf{E}_{N^2}(\mathbf{r}_1(t)) \\ \vdots & \ddots & \vdots \\ C_n \mathbf{E}_1(\mathbf{r}_n(t)) & \cdots & C_n \mathbf{E}_{N^2}(\mathbf{r}_n(t)) \end{bmatrix}, \quad (4.3)$$

we re-write (4.1) for all nanowires as

$$\dot{\mathbf{q}} = \mathbf{B} \mathbf{u}_c, \quad (4.4)$$

where  $\mathbf{B} \in \mathbb{R}^{2n \times N^2}$ . Every two rows in (4.4) represent one nanowire's equation of motion.

Given the desired velocity  $\dot{\mathbf{q}}_d$ , a least-square problem is formulated to obtain control input  $\mathbf{u}_c$  in (4.4)

$$\min_{\mathbf{u}_c} \|\dot{\mathbf{q}} - \dot{\mathbf{q}}_d\|_2 = \min_{\mathbf{u}_c} \|\mathbf{B} \mathbf{u}_c - \dot{\mathbf{q}}_d\|_2. \quad (4.5)$$

The motion gain matrix  $\mathbf{B}$  should have full-row rank and the closed-form solution of (4.5) is given by

$$\mathbf{u}_c = \mathbf{B}^+ \dot{\mathbf{q}}_d, \quad (4.6)$$

where  $\mathbf{B}^+ := \mathbf{B}^T (\mathbf{B} \mathbf{B}^T)^{-1}$  is the pseudo inverse of  $\mathbf{B}$ . To drive the nanowires to follow a given trajectory  $\mathbf{q}_d$ , we define a tracking error  $\mathbf{e} = \mathbf{q} - \mathbf{q}_d$  and consider an exponential convergence profile for  $\mathbf{e}$ , namely,  $\dot{\mathbf{e}} = -\mathbf{K} \mathbf{e}$ , where  $\mathbf{K} = \text{diag}(k_1, \dots, k_{2n})$ ,  $k_i > 0, i = 1, \dots, 2n$ , is a constant gain matrix. Plugging the error dynamics into (4.4), we obtain

$$\dot{\mathbf{q}} = \dot{\mathbf{q}}_d - \mathbf{K} \mathbf{e} = \mathbf{B} \mathbf{u}_c. \quad (4.7)$$

Taking the similar approach in (4.6), we obtain the control input

$$\mathbf{u}_c = \mathbf{B}^+ (\dot{\mathbf{q}}_d - \mathbf{K} \mathbf{e}) = \mathbf{B}^+ \dot{\mathbf{q}}_d - \mathbf{B}^+ \mathbf{K} \mathbf{e}. \quad (4.8)$$



The computation of  $\mathbf{B}$  is obtained by extending the electric-field computation in 2.4 with the superposition and symmetry properties; we will also discuss a numerical approximation coping with physical voltage limitation later in this section. The computational complexity of the algorithm is  $O(n)$ . Since only electrodes in  $\mathcal{E}_b(\mathbf{r}_i)$  influence the motion of  $P_i$ , we conclude that each row of  $\mathbf{B}$  only has  $4r_p^2$  non-zero elements as stated in the following lemma.

**Lemma 4.1.** *The maximum number of nanowires that can be simultaneously controlled in one atomic cell is  $2r_p^2$ .*

*Proof.* Without loss of generality, we assume that  $n_i$  nanowires are in one atomic cell, and no other nanowires in the basic cells. Therefore, the dimension of non-zero elements in  $\mathbf{B}$  is  $2n_i \times 4r_p^2$ . To maintain  $\mathbf{B}$  as full row rank, it follows  $n_i \leq 2r_p^2$ .  $\square$

Similar to Lemma 4.1, we extend the results to basic cell area  $\mathcal{A}_b$  without proof.

**Lemma 4.2.** *The maximum number of nanowires that can be simultaneously controlled in each basic cell area is  $|\mathcal{A}_b|/2$ .*

For the controller given in (4.8), we have the following property.

**Lemma 4.3.** *The powered-on electrodes by controller (4.8) are only inside or on the boundaries of  $\mathcal{A}_b$ .*

*Proof.* Let  $r = |\mathcal{A}_b|$  be the cardinality of set  $\mathcal{A}_b$ . Without loss of generality, we rearrange and decompose  $\mathbf{B} = [\mathbf{B}_r \ \mathbf{B}_{N^2-r}]$ , where matrix  $\mathbf{B}_r \in \mathbb{R}^{2n \times r}$  corresponds to the electric field components inside or on the boundaries of the basic cell area, and  $\mathbf{B}_{N^2-r} = \mathbf{0}$ . Accordingly, we re-arrange and re-construct  $\mathbf{u}_c = [\mathbf{u}_{c_r}^T \ \mathbf{u}_{c_{N^2-r}}^T]^T$  and thus obtain  $\dot{\mathbf{q}} = \mathbf{B}\mathbf{u}_c = [\mathbf{B}_r \ \mathbf{B}_{N^2-r}][\mathbf{u}_{c_r}^T \ \mathbf{u}_{c_{N^2-r}}^T]^T = \mathbf{B}_r\mathbf{u}_{c_r}$ . Any solution  $\mathbf{u}_c$  of (4.4) must contain  $\mathbf{u}_{c_r}$  as components. Since the Moore-Penrose solution (4.8) minimizes the 2-norm of  $\mathbf{u}_c$ , it is the particular solution with  $\mathbf{u}_{c_{N^2-r}} = \mathbf{0}$ . Note that  $\mathbf{u}_{c_{N^2-r}}$  is the voltage of electrodes outside  $\mathcal{A}_b$  and therefore, the actuated electrodes must only be the electrodes inside or on the boundaries of  $\mathcal{A}_b$ .  $\square$

The control inputs obtained by (4.8) do not consider any physical constraints such as device voltage limits. To obtain the voltage inputs that are physically feasible, we modify (4.5) by considering the following optimization problem.

$$\begin{aligned} \min_{\mathbf{u}_c} \quad & \|\mathbf{B}\mathbf{u}_c - \dot{\mathbf{q}}_d\|_2 \\ \text{subject to} \quad & u_{\min} \leq \|\mathbf{u}_c\|_\infty \leq u_{\max}, \end{aligned} \tag{4.9}$$

where  $u_{\min}$  and  $u_{\max}$  are respectively the lower- and upper-bound of the applied voltages. A quadratic programming technique is used to solve (4.9). Because of the physical constraints, the solution of (4.9) does not necessarily result in the shortest-distance path.

To compensate for un-modeled disturbances such as EO-induced flow motions, we also extend the path-tracking control strategy in Section 3.3 to multiple nanowires. The path-tracking control adjusts the desired velocity profile according to the tracking errors in real time. A potential function is used to generate the desired velocity  $\dot{\mathbf{q}}_d(\tau)$  that is parameterized by time variable  $\tau$ , instead of time  $t$ . A self-placing time suspension technique is used to adjust the desired rate of the progression and then the velocity profile online within the planning framework at each time step [134]. To get the desired velocity along  $\pi^*(\mathcal{S}, \mathcal{T})$ , the path-tracking control strategy considers the direction of the desired trajectory, penalizes the tracking direction, and compensates for the predicted error.

The controller given by (4.9) can be proven to have the same properties given in Lemmas 4.1-4.3. To demonstrate this, we have the following results.

**Lemma 4.4.** *The solution of (4.9) is either the same as (4.8) or at the boundary voltages as  $u_{\min}$  or  $u_{\max}$ .*

*Proof.* Defining  $\bar{u} = (u_{\max} + u_{\min})/2$  and  $\delta_u = (u_{\max} - u_{\min})/2$ , the constrained optimization problem in (4.9) can be written with  $N^2$  quadratic inequality constraints

as

$$\min_{\mathbf{u}_c} \quad \|\mathbf{B}\mathbf{u}_c - \dot{\mathbf{q}}_d\|_2 \quad (4.10)$$

$$\text{subject to} \quad (u_{ci} - \bar{u})^2 \leq \delta_u^2, i = 1, 2, \dots, N^2,$$

where  $u_{ci}$  is the  $i$ th element of  $\mathbf{u}_c$ , namely,  $\mathbf{u}_c = [u_{c1} \cdots u_{cN^2}]^T$ . Since the objective function is globally convex and the constraints are also convex, the necessary and sufficient Karush-Kuhn-Tucker (KKT) conditions for a feasible solution  $\mathbf{u}_c$  to (4.10) are

$$(\mathbf{B}^T \mathbf{B} + \boldsymbol{\lambda}^*) \mathbf{u}_c = \boldsymbol{\lambda}^* \bar{\mathbf{u}} + \mathbf{B}^T \dot{\mathbf{q}}_d, \quad (4.11)$$

$$\lambda_i \geq 0, \quad (4.12)$$

$$\lambda_i [\delta_u^2 - (u_{ci} - \bar{u})^2] = 0, \quad (4.13)$$

$$\delta_u^2 - (u_{ci} - \bar{u})^2 \geq 0, \quad (4.14)$$

for  $i = 1, 2, \dots, N^2$ , where  $\boldsymbol{\lambda}^* = \text{diag}(\lambda_1, \dots, \lambda_{N^2}) \in \mathbb{R}^{N^2 \times N^2}$  is a diagonal matrix formed by the Lagrange multipliers.

From (4.12),  $\lambda_i, i = 1, 2, \dots, N^2$ , is either equal to 0 or greater than 0. Let  $m \in \mathbb{N}$  denote the number of  $\lambda_i = 0$  and  $p = N^2 - m > 0$ . We reformulate and re-arrange the Lagrange multiplier vector  $\boldsymbol{\lambda} = [\mathbf{0}_m^T \quad \boldsymbol{\lambda}_p^T]^T$ , where  $\boldsymbol{\lambda}_p \in \mathbb{R}^p$  in which each element is greater than zero. Corresponding to the same re-arranged order as  $\boldsymbol{\lambda}$ , we re-order and re-formulate the control  $\mathbf{u}_c = [\mathbf{u}_{cm}^T \quad \mathbf{u}_{cp}^T]^T$ , and motion gain matrix  $\mathbf{B} = [\mathbf{B}_m \quad \mathbf{B}_p]$ , where  $\mathbf{u}_{cm} \in \mathbb{R}^m$ ,  $\mathbf{u}_{cp} \in \mathbb{R}^p$ ,  $\mathbf{B}_m \in \mathbb{R}^{2n \times m}$ , and  $\mathbf{B}_p \in \mathbb{R}^{2n \times p}$ .

Since the first  $m$  elements in  $\boldsymbol{\lambda}$  are zero, from (4.11) we obtain

$$\mathbf{u}_{cm} = \mathbf{B}_m^+ \dot{\mathbf{q}}_d. \quad (4.15)$$

For  $\boldsymbol{\lambda}_p \neq \mathbf{0}$ , from (4.13),  $\delta_u^2 - (u_{cj} - \bar{u})^2 = 0$ , where  $u_{cj}$  is the  $j$ th element of  $\mathbf{u}_{cp} = [u_{c1} \cdots u_{cp}]^T$ . Then,  $u_{cj} = u_{\min}$  or  $u_{\max}$ ,  $j = 1, 2, \dots, p$ . Therefore, the control solved by (4.9) is either at the inverting solution from (4.8), namely, solution obtained by (4.15), or at the boundary points as  $u_{\min}$  or  $u_{\max}$ . This completes the proof.  $\square$

Similar to Lemma 4.1, in order to maintain  $\mathbf{B}$  in full row rank, it follows that the maximum number of nanowires that can be simultaneously controlled in one atomic cell is  $\min\{2r_p^2, m_b/2\} \leq 2r_p^2$ , where  $m_b$  is the number of  $m$  electrodes that are located within the corresponding basic cell  $\mathcal{E}_b$ . Here,  $m$  is number of electrodes that are not operated at the boundary voltages. Therefore, the results in Lemma 4.1 still hold for the solution obtained by (4.9).

The number of simultaneously controlled nanowires can also be explained through numerical computation of the motion gain matrix  $\mathbf{B}$  in (4.3). Similar to the analysis in [106], we apply singular-value decomposition (SVD) to  $\mathbf{B}$ . To obtain  $\mathbf{B}$ , we uniformly sample  $n_s$  points inside the atomic cells and then form the corresponding matrix  $\mathbf{B}_s \in \mathbb{R}^{2n_s \times |\mathcal{A}_b|}$ . Performing SVD to  $\mathbf{B}_s$ , we obtain  $\mathbf{B}_s = \mathbf{U}\mathbf{\Sigma}\mathbf{V}^T$ , where  $\mathbf{U} = [\mathbf{U}_1 \mathbf{U}_2 \cdots, \mathbf{U}_{2n_s}] \in \mathbb{R}^{2n_s \times 2n_s}$  and  $\mathbf{V} = [\mathbf{V}_1 \mathbf{V}_2 \cdots, \mathbf{V}_{|\mathcal{A}_b|}] \in \mathbb{R}^{|\mathcal{A}_b| \times |\mathcal{A}_b|}$  are both unitary matrix. Matrix  $\mathbf{\Sigma} = [\boldsymbol{\sigma}_b \mathbf{0}]^T \in \mathbb{R}^{2n_s \times |\mathcal{A}_b|}$ , where  $\boldsymbol{\sigma}_b = \text{diag}\{\sigma_1, \cdots, \sigma_{|\mathcal{A}_b|}\}$  is a diagonal matrix formed by the singular values of  $\mathbf{B}_s$ . The SVD approach actually projects and approximates the computation of the electric field through the new orthonormal basis  $\mathbf{U}_i$ , i.e.,  $\mathbf{B}\mathbf{V}_i = \sigma_i \mathbf{U}_i$ .

When we compare the nanowire motion given by (4.4) to the above SVD projection, the orthonormal basis  $\mathbf{U}_i$  is considered as a unit velocity-field vector amplified by  $\sigma_i$  when a unit control vector  $\mathbf{V}_i$  (also orthonormal basis) is applied to the system. Therefore, the larger the singular value  $\sigma_i$ , the larger the velocity that is generated by the corresponding unit control vector  $\mathbf{V}_i$ . Hereby, we treat the ratio of  $\rho_i = \sigma_i/\sigma_1$  as an indicator for the strength of the  $i$ th components of the electric field in comparison to the first (i.e., largest) component when a unit control vector is applied to the electrodes. We truncate  $\mathbf{\Sigma}$  by only keeping the first  $\kappa$  singular values that are greater than a threshold, namely,  $\rho_i > \epsilon$ ,  $i = 1, \cdots, \kappa$ , where  $\epsilon$  is determined by the physical voltage limitation. A truncated electric field matrix is formed as  $\mathbf{B}_t = \mathbf{U}\mathbf{\Sigma}_t\mathbf{V}^T$ , where  $\mathbf{\Sigma}_t$  is the truncated singular-value matrix. We next obtain the truncated  $\hat{\mathbf{B}}$  at the nanowires position  $\mathbf{r}_j$  by interpolation using  $\mathbf{B}_t$ . The control inputs are determined by replacing

$B$  with  $\hat{B}$  in (4.9). By the above discussions and using Lemma 4.2, we conclude that the maximum number of the simultaneously controlled nanowires in the basic cell area is  $\kappa/2$ .

#### 4.4 Multiple nanowire motion planning

In this section, we present a two-stage motion-planning scheme to generate the optimal trajectory  $\pi^*(\mathcal{S}, \mathcal{T})$  for all nanowires, while preserving the constraints given in the motion-control design in the previous section. The optimized trajectory minimizes the cost function, which in this work we consider as the sum of all nanowires' traveling distances, namely,

$$C(\pi(\mathbf{q}_l, \mathbf{q}_{l+M})) = \sum_{i=1}^n \sum_{k=l}^{l+M-1} \|\mathbf{r}_i(k+1) - \mathbf{r}_i(k)\|, \quad (4.16)$$

where  $M$  is the number of planning time steps starting from  $\mathbf{q}_l$  to  $\mathbf{q}_{l+M}$ .

The two-stage motion-planning algorithm is shown in Algorithm 3. As discussed in the previous section, for all nanowires, if  $\mathcal{A}_b^i$  do not overlap each other at each time instance, then no coupling effect of the electric field exists for manipulating individual  $P_i$ s, and thus the motion control and planning strategy in chapter 3 can be directly applied to each  $P_i$ . We consider this case “not OverLoaded”, and Algorithm 3 only goes through the second stage (Lines 4 and 5). If  $\mathcal{A}_b^i$ s overlap for at least two nanowires at a time, the algorithm goes to the first stage (Lines 1-3). In this case, a min-cost max-flow (MCMF) global routing algorithm is used to select the atomic cells for each  $P_i$  from  $\mathbf{r}_{iS}$  to  $\mathbf{r}_{iT}$ . If feasible, the MCMF generates the shortest total-distance path and meanwhile guarantees that the number of nanowires is not greater than the capacity of the cell. If the MCMF planning fails, the lower bound of the MCMF is relaxed and an A\*-inspired MCMF planning algorithm is used to search for the optimal path. The second stage of motion planning is to generate collision-free  $\pi^*(\mathcal{S}, \mathcal{T})$  among the selected cells to form the shortest path. An RRT-based motion-planning algorithm is used with a collision-avoidance strategy, called stRRT. The stRRT algorithm is inspired

by the idea of minimizing the dimensionality of the search space from  $M^*$  [135]. In the following, we describe these two stages in detail.

---

**Algorithm 3:** Two-stage motion planning and control

---

**Input** :  $\mathcal{S}, \mathcal{T}$

**if** OverLoaded **then**

- 1 | Construct flow graph and MCMF global routing
- 2 | If MCMFfeasible go to 4
- 3 | Run A\* MCMF re-planning and go to 4

**else**

- 4 | Run visibility graph-based shortest path planning
- 5 | Run stRRT collision-free motion planning

**end**

Run control design (4.9) for each  $\mathcal{A}_b$ .

---

#### 4.4.1 First-stage planning

The purpose of the first-stage planning is to select adequate atomic cells for each nanowire while maintaining the number of nanowires inside  $\mathcal{A}_b$  to be no greater than  $|\mathcal{A}_b|/2$  by Lemma 4.2 (or  $\kappa/2$  computed by the SVD method as detailed in the previous section.) Since nanowires in different atomic cells might move across the cell boundaries, with the result of possibly violating the constraints in Lemma 4.2, we use the MCMF global routing to coordinate the atomic-cell selection. This process maintains the number of nanowires below the maximum capacity for each atomic cell while coordinating the motion of multiple nanowires by setting the lower-bound path constraint in the flow graph. If the MCMF is not feasible, an  $A^*$  re-planning is applied and the algorithm re-calculates the optimal path each time. If the cell selection is changed, then a set of back propagation vertices are added to an open list and no-search iteration is then initiated with a heuristic cost.

Algorithm 4 describes how the direct flow graph  $G$  from  $\mathcal{S}$  and  $\mathcal{T}$  is constructed. The algorithm first finds all the paths (sequences of atomic cells) with shortest Manhattan distance between  $\mathcal{A}_a(\mathcal{S})$  and  $\mathcal{A}_a(\mathcal{T})$  and then forms these paths as part of the direct graph. In the direct graph, each node is an atomic cell and the indexing of

the cells follows the same column-wise labeling rule for the electrode sets. Functions `AllCombination` computes the number of combinations of  $N_a$  that take value of  $\Delta_x$ , and `act` takes the  $-1$  (backward),  $0$  (no movement), or  $1$  (forward) to represent the motion in both the  $x$ - and  $y$ -axis directions. Function `move` generates the atomic cells according to the movement from `act`, and `link` creates the links of the atomic cells from  $\mathbf{r}_{iS}$  with the shortest Manhattan distance between  $\mathcal{A}_a(\mathcal{S})$  and  $\mathcal{A}_a(\mathcal{T})$ . The algorithm has complexity of  $O(nN^2)$ .

---

**Algorithm 4:** Flow Graph Formulation

---

**Input :**  $\mathcal{S}, \mathcal{T}$ 
**Output:**  $G$ 
**for**  $i = 1$  *to*  $n$  **do**
 $G_i.add(\mathcal{A}_a^i(\mathbf{r}_{iS}))$ 
 $\Delta_x \leftarrow \text{proj}_x(\lceil \mathbf{r}_{iT}/L \rceil - \lceil \mathbf{r}_{iS}/L \rceil), \Delta_y \leftarrow \text{proj}_y(\lceil \mathbf{r}_{iT}/L \rceil - \lceil \mathbf{r}_{iS}/L \rceil)$ 
 $d_x \leftarrow \text{sign}(\Delta_x), d_y \leftarrow \text{sign}(\Delta_y), N_a \leftarrow |\Delta_x| + |\Delta_y|,$ 
 $C \leftarrow \text{AllCombination}(N_a, \Delta_x), N_C \leftarrow \text{size}(C)$ 
**for**  $j = 1$  *to*  $N_C$  **do**
 $\text{act} \leftarrow \text{zeros}(2, N_a + 1), \text{act}(1, C_j + 1) \leftarrow d_x$ 
 $id \leftarrow \text{find}(\text{act}(1, 2 : \text{end}) == 0)$ 
 $\text{act}(2, id) \leftarrow d_y, G_{ij} \leftarrow \text{link}(\text{move}(\mathbf{r}_{iS}, \text{act}))$ 
**end**
 $G_i.add(G_{ij})$ 
**end**


---

According to the construction, multiple nanowires may exist in the same node in the flow graph. We introduce capacity upper bound  $U_{ij}$ , lower bound  $L_{ij}$ , and cost  $C_{ij}$  to edge  $i$  that connects to node  $\mathcal{A}_a^j$ .  $U_{ij}$  and  $L_{ij}$  represent the maximum and minimum numbers of nanowires that travel from  $\mathcal{A}_a^i$  to  $\mathcal{A}_a^j$ , respectively, and  $C_{ij}$  indicates the heuristic cost of nanowires from  $\mathcal{A}_a^i$  to  $\mathcal{A}_a^j$ . The value of  $U_{ij}$  is given as

$$U_{ij} = \min(|U_{\mathcal{A}_a^j} - \sum_{k=1}^3 P_{kj}|, 2r_p^2), \quad (4.17)$$

where  $U_{\mathcal{A}_a^j} = |\mathcal{A}_a^j|/2 - \sum_{\mathcal{A}_a^l \in \mathcal{A}_a^j} N_{\mathcal{A}_a^l}$  is the capacity of atomic cell  $\mathcal{A}_a^j$ ,  $N_{\mathcal{A}_a^l}$  is the number of nanowires use  $\mathcal{A}_a^l$  for routing. The first term in (4.17) calculates the upper-bound capacity for the edge from  $\mathcal{A}_a^i$  to  $\mathcal{A}_a^j$  by subtracting the possible number of nanowires

that travel from other three neighboring edges of  $\mathcal{A}_a^j$ ; see Figure 4.2. Denoting  $\mathcal{A}_a^{jk}$ ,  $k = 1, 2, 3$ , as the three atomic cells adjacent to  $\mathcal{A}_a^j$ ,  $P_{kj}$  is the possible number of nanowires travel from  $\mathcal{A}_a^{jk}$  to  $\mathcal{A}_a^j$  if  $k \neq i$  or from  $\mathcal{A}_a^i$  to  $\mathcal{A}_a^j$  if  $k = i$  in  $\mathbf{G}$ , if they travel along the straight line connecting every pair of corresponding starting and targeted points in  $\mathcal{S}$  and  $\mathcal{T}$ , denoted by  $\overline{\mathcal{ST}}$  in both cases. Term  $P_{kj}$  is calculated as

$$P_{kj} = \begin{cases} N_{\mathcal{A}_a^{jk}} & \pi(\mathbf{q}(t_1), \mathbf{q}(t_2)) \subseteq \overline{\mathcal{ST}}, \mathbf{r}(t_1) \in \mathcal{A}_a^{jk}, \\ & \mathbf{r}(t_2) \in \mathcal{A}_a^j, k \neq i \\ N_{\mathcal{A}_a^{ij}} & \pi(\mathbf{q}(t_1), \mathbf{q}(t_2)) \subseteq \overline{\mathcal{ST}}, \mathbf{r}(t_1) \in \mathcal{A}_a^i, \\ & \mathbf{r}(t_2) \in \mathcal{A}_a^j, k = i \\ 0 & \text{otherwise.} \end{cases} \quad (4.18)$$

The lower bound  $L_{ij}$  of an edge from  $\mathcal{A}_a^i$  to  $\mathcal{A}_a^j$  in  $\mathbf{G}$  is defined as  $L_{ij} = P_{ij}$  in the MCMF global routing to minimize the cost by traveling through straight lines, and  $L_{ij} = 0$  in the A\* MCMF re-planning. The cost of an edge from  $\mathcal{A}_a^i$  to  $\mathcal{A}_a^j$  in  $\mathbf{G}$  is defined as  $C_{ij} = \frac{2}{1+L_{ij}}$ .

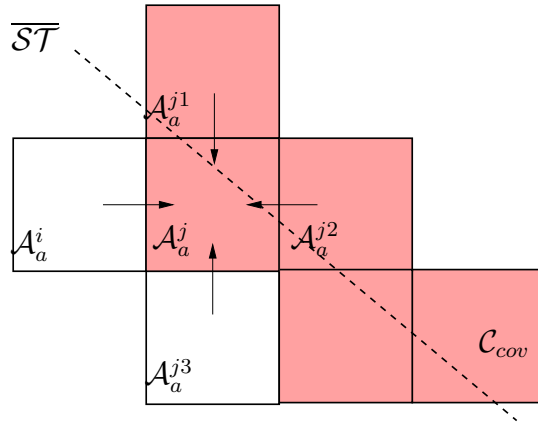


Figure 4.2: Schematic of the capacity  $U_{ij}$  calculation and *CoverCell*  $\mathcal{C}_{cov}$  illustration as the shaded cells across  $\overline{\mathcal{ST}}$ .

To enforce strictly the constraints of the capacity bounds from  $\mathcal{S}$  to  $\mathcal{T}$ , we define *CoverCell*, denoted as  $\mathcal{C}_{cov}$ , as a set of sequenced atomic cells that  $\overline{\mathcal{ST}}$  crosses through for each nanowire. We build a Bresenham-based cover-cell algorithm to compute  $\mathcal{C}_{cov}$ . For  $P_i$ , the algorithm finds the line-segment intersections of  $\overline{\mathbf{r}_{iS}\mathbf{r}_{iT}}$  and all the boundary



lines of atomic cells; see Figure 4.2. The algorithm then records all the center points of the atomic cells that  $\overline{\mathbf{r}_{iS}\mathbf{r}_{iT}}$  covers and returns the linear index sequence of the covered atomic cell  $\mathcal{C}_{cov}$ . The algorithm has complexity of  $O(nN)$ .

In the MCMF global routing,  $U_{ij}$ ,  $L_{ij}$  and  $C_{ij}$  are calculated based on the assumption that each nanowire lies in  $\mathcal{C}_{cov}$  for all time, while in the  $A^*$  MCMF re-planning, the  $U_{ij}$ ,  $L_{ij}$  and  $C_{ij}$  are calculated based on the location of the nanowires at the current time instance. Note that the capacity is always underestimated for the edges and thus, the MCMF global-routing algorithm finds the minimum number of non-detour and non-overload atomic cells for each nanowire. We use TORSCHÉ Scheduling Toolbox [136] and the integer programming solver in the GLPK package [137] to solve the MCMF problem. The algorithm has complexity of  $O(N^4 \log(N))$  in the worst case.

The  $A^*$  MCMF re-planning algorithm first takes the optimal straight-line path and adds the corresponding atomic cell list  $\mathcal{Q}_i$  into the open list. If the MCMF calculation result  $\mathcal{Q}'_i$  based on the starting configuration's capacity and cost is different from  $\mathcal{Q}_i$ , then  $\mathcal{Q}'_i$  is added to the open list. Each time a nanowire crosses any atomic cell boundary and the corresponding capacity of the atomic cell changes, the MCMF algorithm re-calculates with the updated capacity. If the re-calculated MCMF cell selection is changed, then a set of feasible back-propagation paths are checked and the least-cost one is added to the open list by (4.16). One node in the open list keeps being examined until the maximum iteration number is reached. The algorithm returns the optimal trajectory and at each iteration, and the most promising vertex (i.e., the cheapest path) is taken from the open list and expanded. The algorithm has the worst-case complexity of  $O(nN^5 \log(N))$ .

#### 4.4.2 Second stage planning

After obtaining the sequenced atomic cells for each nanowire, we construct the roadmap in the free space. We build the roadmap by visibility graphs using a sweepline algorithm [107] with complexity of  $O(N \log(N))$ . An  $A^*$  algorithm [107] is then used to

search for the shortest path on the road map. The algorithm returns the shortest path between the initial and final configuration of each nanowire that follows the atomic-cell selection from the first-stage planning.

A  $\text{stRRT}$  motion-planning algorithm is proposed to generate the collision-free path for all nanowires. We denote the configuration space of nanowire  $P_i$  as a directed graph  $\mathcal{G}_{rrt} = \{V, E\}$ , where  $V$  is the set of vertices in  $\mathcal{G}_{rrt}$  and  $E$  represents directed edge transitions connecting vertices. The  $\text{stRRT}$  process is similar to the RRT algorithm with two differences: First, the configuration space is one-dimensional, instead of  $2D$  continuous space. The sampling points are along the given path. Also, the  $\text{stRRT}$  algorithm checks whether the location of nanowires in  $\mathbf{q}_{new}$  causes the graph to go above its capacity; if so,  $\text{stRRT}$  re-samples states. Second, for the distance metric, only positive distance vectors from nodes on  $\mathcal{G}_{rrt}$  to random  $\mathbf{q}_{rand}$  are considered. The RRT algorithm guarantees the completeness and the  $A^*$  process guarantees the optimality. The collision avoidance is included in the  $\text{stRRT}$  algorithm by checking whether any collisions occur between pairs of nanowire paths in the new state  $\mathbf{q}_{new}$ . If there are no collisions, then  $\mathbf{q}_{new}$  and the edge from  $\mathbf{q}_{nearest}$  to  $\mathbf{q}_{new}$  are added to the  $\mathcal{G}_{rrt}$  structure. If a collision cannot be avoided without changing the path, e.g., two nanowire paths are collinear and move towards each other,  $\text{stRRT}$  then generates two separate sub-paths for the nanowires and adds the sub-paths into the searching path. The algorithm finally returns  $\pi^*(\mathcal{S}, \mathcal{T})$ .

## 4.5 Simulation and experimental results

In this section, we first present simulation results and then show experiments to demonstrate the simultaneous motion control and planning of multiple nanowires.

### 4.5.1 Simulation results

We first demonstrate the performance of the simultaneous motion control of multiple nanowires. In the simulation, we set  $L = 600 \mu\text{m}$  and  $R = 150 \mu\text{m}$  to match the dimensions of the micro-fluidic device in experiments. Figure 4.3(a) shows the simultaneous motion control of 8 nanowires to form an “RU”-character trajectory using a  $5 \times 5$  electrode array. To simulate unmodeled nanowire motions due to disturbances such as background EO flow [78], we have added a random position disturbance within a range of  $\pm 10 \mu\text{m}$  in each nanowire’s motion. The actual trajectories are not straight lines when disturbances exist and no tracking error compensation is used. Figure 4.3(b) shows the simulation result of simultaneous motion control of 3 nanowires to track a circular shape trajectory. From these simulation results, it can be seen that the motion control scheme accurately and effectively steers multiple nanowires simultaneously, even under random fluid disturbances.

Figure 4.4(a) illustrates the simultaneous motion planning and motion control of 10 nanowires to re-position them into an equally spaced crossed-line pattern. The MCMF global routing is feasible and the  $A^*$  MCMF re-planning step is skipped. The motion-planning algorithm generates the trajectories to avoid the possible collision between nanowires. For comparison, Figure 4.4(b) shows the direct motion control of 10 nanowires to form the same cross-line trajectory, but without motion planning and path tracking. It clearly shows that nanowires #3 and #8 fail to reach the target locations due to collisions.

We now demonstrate the performance of the two-stage motion-planning and control algorithms. For an  $N \times N$  electrode array, we first specify a number of nanowires and then select the locations of starting and target points. We distribute these nanowires in randomly chosen atomic cells. The starting and targeted locations for each nanowire are also randomly determined in these cells. To eliminate the performance dependency on the simulation specifications and procedures, we conduct 30 runs of each configuration for the same algorithm and then compute the statistics in these simulation runs.

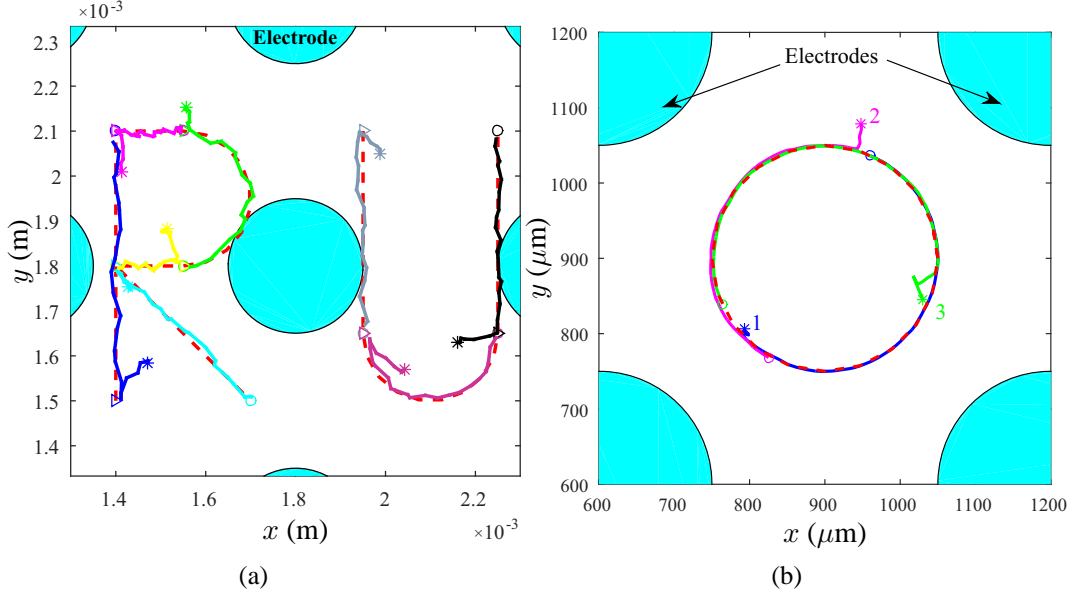


Figure 4.3: (a) Simultaneous motion control of 8 nanowires to form an RU trajectory in the presence of random fluid disturbances. The total travelling time is 26 s. (b) Simultaneous motion control of 3 nanowires to track a circular shape trajectory. The total travelling time is 877 s. The “\*” markers indicate the position of the random starting points, the “▷” and “○” markers are the starting and ending points of each trajectory segment, respectively. The solid lines are the actual trajectories and the dashed lines are the desired trajectories.

The simulation are running on a computer with Intel Core i7-4700 CPU at 2.40 GHz and 4G RAM memory. We first conduct simulation testing for three combinations of numbers of the electrodes and the nanowires:  $(N, n) = (6, 18)$ ,  $(8, 30)$  and  $(9, 40)$ . These configurations all satisfy the capacity requirements given in Lemma 4.2. Figure 4.5 shows the 2D trajectory results under the two-stage motion-planning and control algorithms for one representative run. From these plots, we clearly observe that the trajectories of the nanowires are all near straight-line; this is primarily due to the choice of distance metric in the cost function.

Figure 4.6 further shows the computation times (mean and one standard deviation) for the two-stage motion planning algorithm, compared with the RRT\* algorithm [123] for a  $6 \times 6$  ( $N = 6$ ) electrode array. The RRT\* algorithm is implemented by using the same control scheme discussed in Section 4.3. The computation time under the two-stage algorithm shows roughly polynomial increasing with the number of nanowires

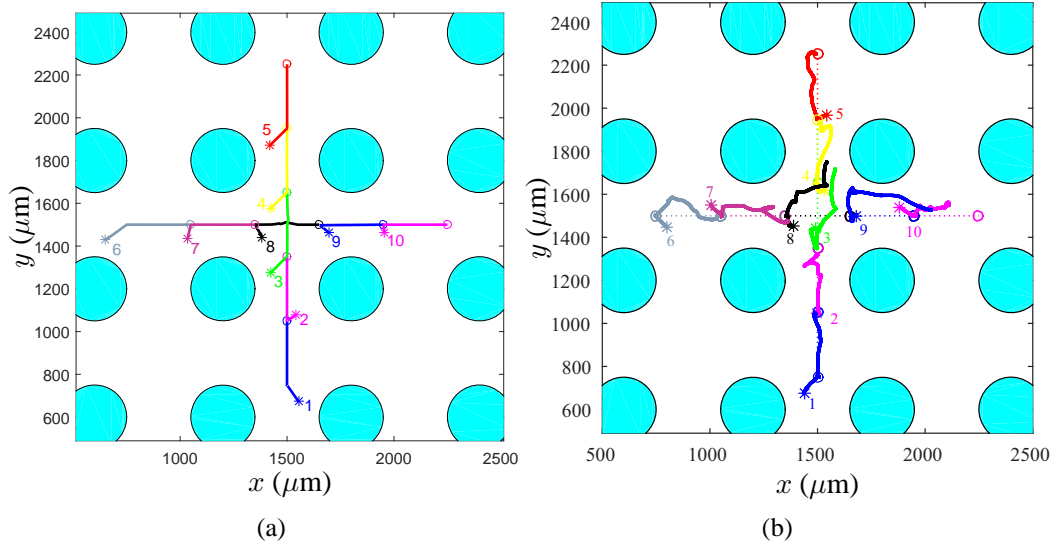


Figure 4.4: (a) Motion planning and control of 10 nanowires simultaneously to form an equally spaced crossed-line trajectory. The total travelling time is 664.5 s. (b) Simultaneously direct motion control of 10 nanowires try to form the same cross line trajectory as (a) without motion planning and path tracking, but fail due to collision. The total travelling time is 111.4 s. The “\*” markers indicate the position of the random starting points and the “o” markers are the ending points of each desired trajectory segment. The solid lines represent the actual trajectories and the dashed lines are the desired trajectories.

and is more than three-order-of-magnitude more efficient than the RRT\* algorithm. The numbers on each data point shown in Figure 4.6 show the associated success rates under the two motion-planning algorithms with a maximum iteration number of 30,000 and a maximum running time of 10,000 s. It is clearly demonstrated that for a small number of nanowires (e.g.,  $n = 2, 3$ ), both the two-stage and the RRT\* algorithms achieve 100% success rates. However, when the number of nanowires increases, the two-stage algorithm clearly outperforms the RRT\* algorithm. In particular, when more than five nanowires must be routed, the RRT\* algorithm cannot successfully generate the planning results while the two-stage algorithm shows robust performance.

To demonstrate the efficiency of using the SVD to compute the nanowire capacity in atomic cells, Figure 4.7 indicates the maximum number of nanowires that can be simultaneously controlled in different numbers of atomic cells with a choice of  $\epsilon = 0.01$ . The comparison between the original electric field and the SVD-truncated electric field

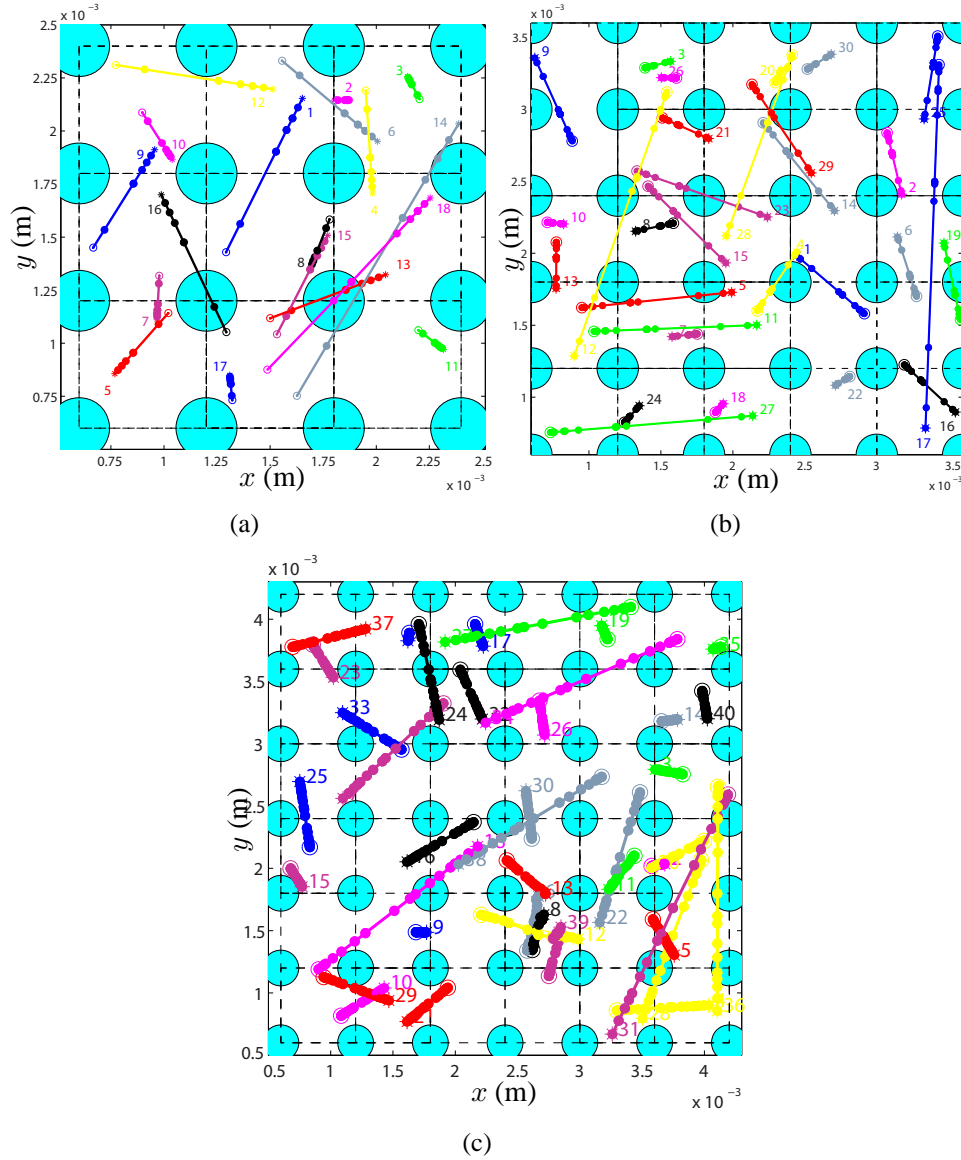


Figure 4.5: Simulation of simultaneous motion planning and control of different numbers of nanowires. (a) 18 nanowires in a  $6 \times 6$  electrode array with the total travelling time 858 s. (b) 30 nanowires in an  $8 \times 8$  electrode array with the total travelling time 1386 s. (c) 40 nanowires in a  $9 \times 9$  electrode array with the total travelling time 1826 s.

shows that the more atomic cells involved in the control problem, the more nanowires can be simultaneously controlled within the physical voltage limitation. The results confirm that the use of the SVD computation can capture the same nanowire capacity as that by the original electric field-based method. The atomic cell-nanowire capacity relationship is almost linear and scalable for a large number of nanowires. Therefore,

an effective motion-planning algorithm is needed in order to control the theoretical-maximum (Lemma 4.2) number of nanowires simultaneously.

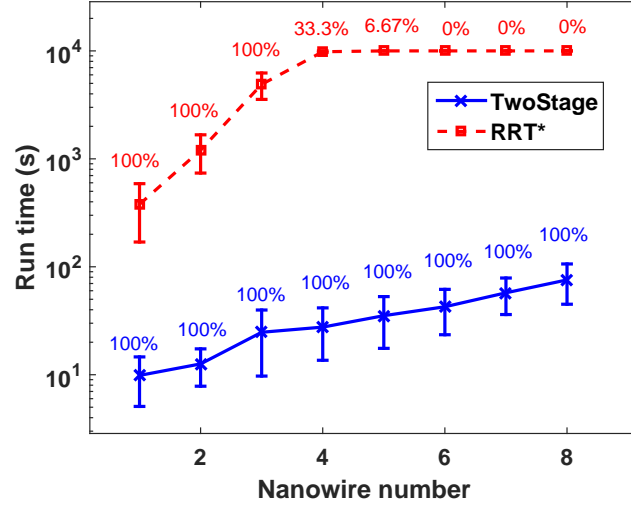


Figure 4.6: Run-time comparison between the TwoStage and the RRT\* algorithms with different numbers of nanowires in a  $6 \times 6$  electrode array. The numbers on each data point show the success rates for both the TwoStage and the RRT\* algorithms. The last five data points for the RRT\* algorithm are clamped to  $10^4$  s due to reaching the maximum running time limit.

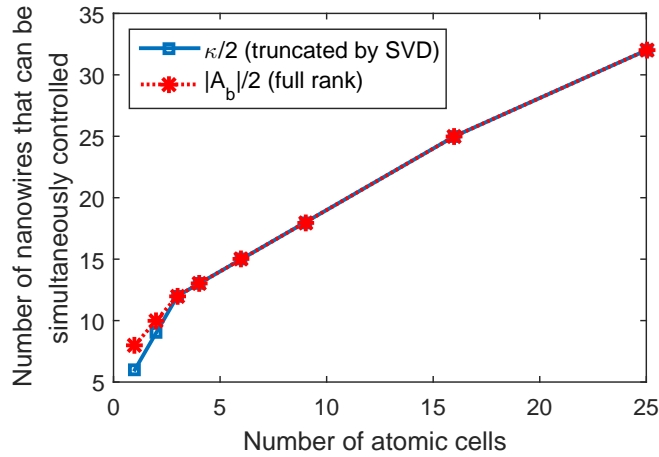


Figure 4.7: Comparison of the maximum number of nanowires that can be simultaneously controlled in different numbers of atomic cells between the original electric field and SVD-truncated electrical field.

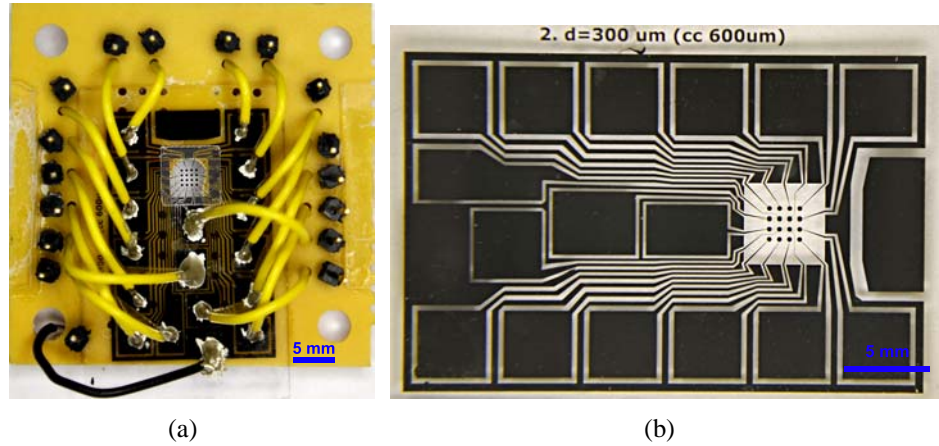


Figure 4.8: (a) The micro-fluidic device mounted on a PCB testing board. (b) The top view of the micro-fluidic device with  $4 \times 4$  electrode arrays.

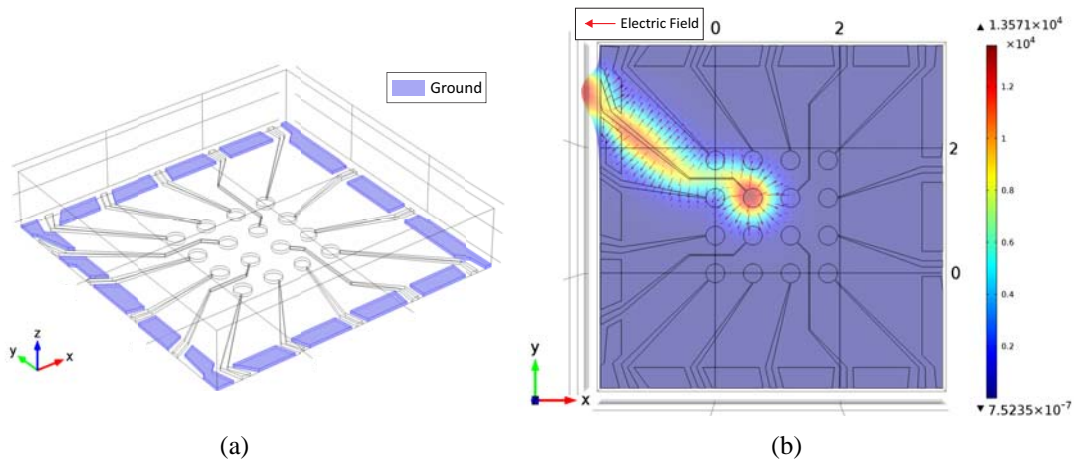


Figure 4.9: (a) A schematic of the geometry design of the micro-fluid reservoir. The shaded areas show the common electrical ground on the bottom substrate. (b) Sample electric-field distribution when a voltage with a magnitude of 10 V is applied to only one electrode marked as the red color and other electrodes are grounded. The red arrows show the direction of the electric field and the color legend shows the magnitude of the electric field.

#### 4.5.2 Experimental results

Figure 3.3 shows the overall experimental setup and Figure 4.8(a) shows the micro-fluidic device mounted on a testing PCB board fabricated for this study. A detailed view of the electrodes on the bottom surface of the micro-fluidic device is shown in Figure 4.8(b). The PCB mounting board shown in Figure 4.8(a) is installed on a motorized, computer-controlled microscope XY stage (Prior ProScan III) on an inverted



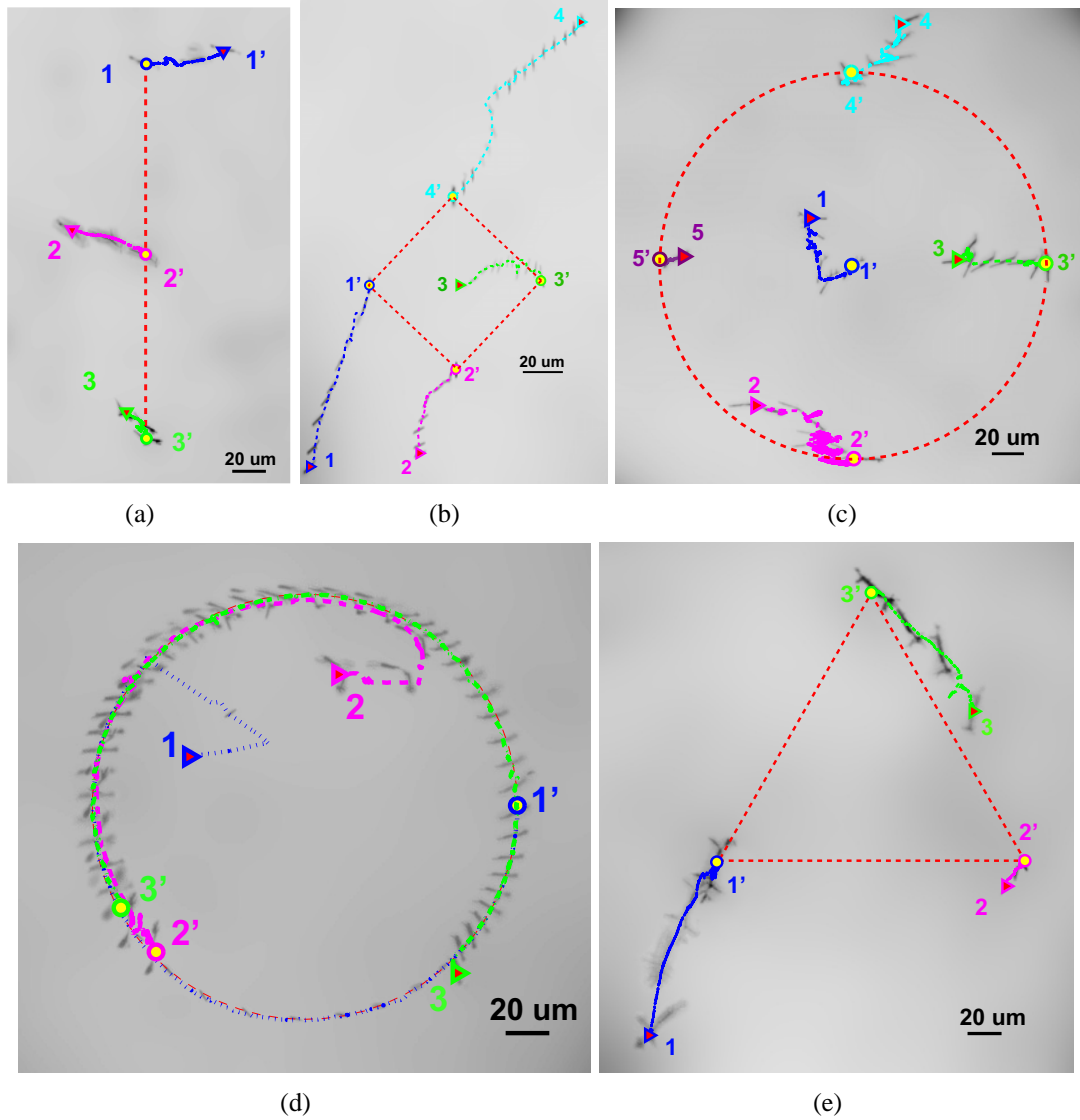


Figure 4.10: Overlaid nanowire trajectories to form different geometric patterns. All pictures are obtained by taking and overlaying the nanowire images at a series of time snapshots. All background images are removed to clearly present the nanowire trajectories. The “▷” and “○” marks indicate the nanowires’ initial and final positions, respectively. (a) A straight-line with the total travelling time 66.3 s. (b) A square with the total travelling time 222 s. (c) A circle with one nanowire at the center with the total travelling time 338.6 s. (d) Simultaneous tracking control of three nanowires to form a circle. The total travelling time is 253 s. (e) An equilateral triangle with the total traveling time 172.4 s.

microscope(Olympus IX71). Bright field images are recorded using a 40× objective and a low light high sensitivity camera (pco.edge sCMOS) with a 2560 × 2160 pixels

resolution. The high-resolution images provide visual feedback of the precise movements of the nanowires in larger range of motion across the field of view for visual feedback. An embedded system (NI cRIO 9074) is used to control the electrode array and a LabView application extracts nanowire positions in real time from recorded images and provide vision-based feedback. The micro-fluidic device shown in Figure 4.8(b) has a  $4 \times 4$  electrode array. The radius of the electrodes is  $R = 150 \mu\text{m}$ , and distance  $L = 600 \mu\text{m}$ . The device was fabricated by lithographic patterning and sputtering of platinum on a glass substrate through typical MEMS-fabrication procedures. In experiments,  $u_{\max} = 50 \text{ V}$ ,  $u_{\min} = -50 \text{ V}$  and a PWM-based continuously adjusted potential is selectively applied to the electrodes.

The same as in Chapter 3, we use metal-assisted chemical etched silicon nanowires suspended in the heavy viscosity mineral oil at a concentration of  $0.5 \text{ mg/ml}$ . Figure 3.4(a) shows a forest of the silicon nanowires fabricated for the experiments. The values of the model parameters of the nanowire used in motion control design are as follows:  $\mu = 251.2 \text{ cP}$ ,  $\epsilon_m = 2.17\epsilon_0$ . The dimension of the silicon nanowires after suspended in the oil is around  $5$  to  $18 \mu\text{m}$  in length,  $100$  to  $200 \text{ nm}$  in diameter, and the sampling time is taken as  $0.1 \text{ s}$ . Figure 4.9(a) shows the zoomed view of the geometry design of micro-fluid reservoir. The shaded areas show the common electrical ground terminals on the substrate surface. Figure 4.9(b) illustrates a typical distribution of the electric field in the same area when a voltage of  $10V$  magnitude is applied to only one electrode indicated by the red color (and other electrodes are grounded.) Similarly, the electric field distribution of each electrode on the bottom substrate is stored in a look-up table, and is used in (4.2) to compute the electric field at each nanowire's position.

We first estimated and updated the zeta-potential values for each nanowire at the start of the experiments. This was done by applying a constant potential to the electrodes array for a few seconds and recording the motion of the nanowires. We then calculated the electric field acting on each nanowire using (4.2) and used least-square fitting to estimate the zeta-potential of each nanowire from the measured velocity and

given electric field. The online estimation of the nanowire zeta-potential enables the proposed method independent of the sizes and material characteristics of the nanowires as long as the EP force exists and dominates their motions. More details about the zeta-potential estimation can be found in Chapter 4 or [76].

Figure 4.10 shows a series of experimental results of steering multiple nanowires from different starting positions to target locations to form specific geometric shapes: a straight-line with three nanowires (Figure 4.10(a)), a square with four nanowires at the vertices (Figure 4.10(b)), a circle with four nanowires at the 12-, 3-, 6-, and 9-o'clock positions with an additional nanowire at the center (Figure 4.10(c)), and a triangle with three nanowires at the vertices (Figure 4.10(e)). Figure 4.10(d) further demonstrates that the motion planning and control methods can be used for continuous tracking control of three nanowires along a circular trajectory. In these figures, we show the initial and final positions of these nanowires as well as overlaid transient positions. It is interesting to observe that under the proposed motion planning and control algorithms, the nanowires can be steered into different and sometimes even opposite motion directions simultaneously (e.g., nanowires #1 and #2 in Figure 4.10(a)). Figure 4.11 further demonstrates the motion planning and control of three nanowires initially located in three different atomic cells to form an equally spaced horizontal line while avoiding any collisions. It is observed in the experiment that nanowire #1 has passed nanowires #2 and #3 before they reached their targeted locations. Also Figure 4.11 shows that nanowires can be guided across the atomic-cell boundaries. These experiments clearly demonstrate the feasibility and performance of motion planning and control for multiple nanowires simultaneously.

As discussed previously, the complex EO background flow has a significant impact on nanowire motion and the motion-control algorithms compensate for the background flow motion using a path-tracking technique similar to that in Section 3.3. As an example, Figure 4.12 shows the trajectory of three nanowires without compensating for

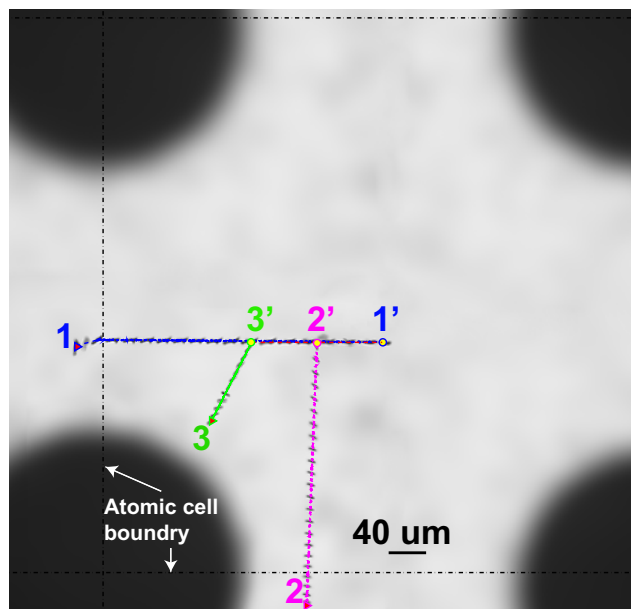


Figure 4.11: Motion planning and control for three nanowires simultaneously guided from three different initial atomic cells to form an equally spaced horizontal line. The total travelling time is 1086.1 s. The “ $\triangleright$ ” and “ $\circ$ ” marks indicate the nanowires’ initial and final positions, respectively.

background fluid motion, whereas Figure 4.10(e) demonstrates the results under compensation. Clearly, the motion of these nanowires is completely disturbed without the EO-flow compensation.

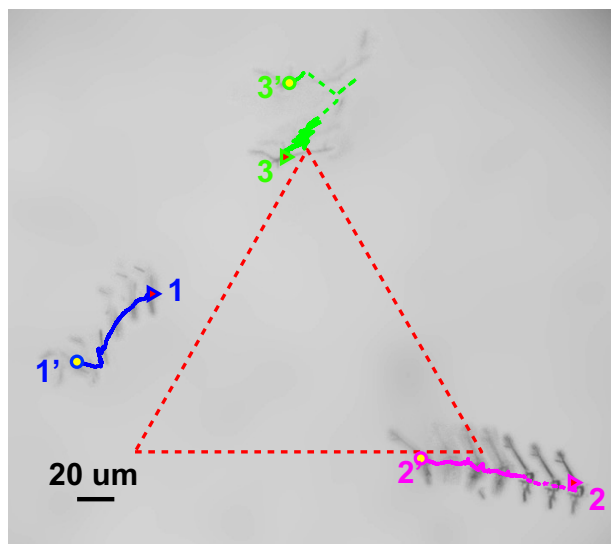


Figure 4.12: Overlaid nanowire trajectories and formation control of three nanowires without compensation for EO background flow. The total travelling time is 401.7 s.

## 4.6 Conclusion

This chapter presented an electric-field-based motion-planning and control algorithms for the simultaneous steering of multiple nanowires in liquid suspension. A motion-control algorithm was designed to simultaneously steer multiple nanowires to follow desired trajectories under controlled EP forces. A two-stage motion-planning algorithm was proposed and demonstrated to minimize the total travel distances for multiple nanowires in 2D space. The motion-planning algorithm was built on the network-flow MCMF problem to generate the feasible atomic-cell areas with incorporating the simultaneous motion-control capacity limits. The nanowires' roadmap was then constructed in the reduced search area to obtain the obstacle-avoiding optimal path. Simulation results demonstrated that the two-stage algorithm reduced the computational complexity significantly when compared with the RRT\* algorithm. We have also demonstrated the performance of the proposed motion-planning and control schemes with extensive experiments to illustrate the automated manipulation of multiple nanowires in a microfluidic device.

The objective of this chapter is to minimize the total traveling distance of all nanowires and the total traveling time is not optimized. In Chapter 3, we have found that the shortest-distance trajectory does not demonstrate the shortest time. Therefore, the time-optimal simultaneous motion planning and manipulation of multiple nanowires is studied in the next chapter to improve the manipulation efficiency.

## Chapter 5

# Time-Optimal Simultaneous Motion Planning and Manipulation of Multiple Nanowires under Electric-Fields in Fluid Suspension

### 5.1 Introduction

Driving nanowires in fluid suspension under electric field has been demonstrated as an effective way for automated manipulation, sorting and characterization of these nanowires [69, 70]. In [76, 78, 79] and Chapter 3, we have developed an EP-based motion planning and manipulation algorithms to steer and drive a single nanowire in fluid suspension. The extension of the EP-based motion planning and control for simultaneously driving multiple nanowires is presented in [77, 80] and Chapter 4. Due to the complexity of the combinatorial optimization, the motion planning algorithm (i.e., a two-stage planning approach) in Chapter 4 uses a heuristic technique to quickly generate the total shortest-distance trajectories for multiple nanowires. Obstacle avoidance is also considered in the planning algorithm in Chapter 4. The performance of the two-stage algorithm in Chapter 4 can be further improved in several aspects. First, as illustrated in Chapter 4, the shortest total traveling distances of all nanowires do not imply the shortest traveling time. Indeed, the shortest traveling-time trajectory is not the straight-line connecting the starting to target points due to the electric field distribution. Therefore, it is desirable to obtain the minimum-time trajectory for fast planning algorithms. Second, because of the straight-line constraint, the maximum number of nanowires that can be simultaneously steered in the two-stage algorithm is limited to an upper bound. For scalability, it is desirable to find an alternative motion planner to

relax such constraints.

The goal of this chapter is to extend the approach in Chapter 4 to present time-optimal motion-planning and control of multiple nanowires simultaneously in fluid suspensions. The EP-force is still used as the primary driving force, while the motion control design also compensates for the electro-osmosis disturbance. Inspired by the SST and RRT\* approaches, an improved sparse RRT\* based motion-planning algorithm, called SRRT\*, is proposed to generate the asymptotically near time-optimal trajectories of multiple nanowires. Moreover, unlike the previous results in Chapter 4, the maximum number of nanowires that can be steered at one time is not limited by the upper bound that depends on the number of neighboring electrodes. The SRRT\* algorithm takes the advantages of the rewiring strategy of the RRT\* and the stable sparse structure of the SST to efficiently achieve the asymptotically near time-optimal trajectory with several heuristic techniques. We demonstrate the performance of the proposed SRRT\* algorithm through numerical simulations and experiments.

The main contribution of the chapter lies in the development and demonstration of the asymptotically near-time-optimal motion-planning and control algorithms for simultaneously steering multiple nanowires efficiently in liquid suspension.

The remainder of this chapter is organized as follows. We present the problem formulation in Section 5.2. The nanowire-motion-control strategy is proposed in Section 5.3. The motion-planning algorithms are presented in Section 5.4. We then present simulation and experimental results in Section 5.5. Finally, we conclude the chapter and discuss the future work directions in Section 5.6.

## 5.2 Problem formulation

As presented in Chapter 2, Figure 2.1 shows the schematic of the micro-fluidic device. We consider a device with  $N \times N$  electrodes on the bottom surface. The square lattice array of circular electrodes is fabricated on a glass substrate with equal distance  $L$

between centers (Figure 2.1(b)). The actual device is shown in Section 5.5.2. Each electrode is independently actuated with different DC voltage, which is used to steer and drive the nanowires to the targeted horizontal locations. A common electrode is used as the top coverslip to vertically position the nanowires and deposit them at desired locations on the substrate.

As defined in Section 4.2, we consider  $n$  nanowires in the 2D work space with a coordinate system defined at the left-bottom corner on device; see Figure 4.1. The electrode control matrix and other system notations are the same as defined in Section 4.2.

Under a DC electric field, the equation of motion for  $P_i$  is given the same as in (4.1). From (4.1), the electric field is regulated to steer the nanowires' motion by appropriately applying voltage  $\mathbf{u}$  to electrodes. The calculation of electric field  $\mathbf{E}_i$  at  $i$ th nanowire position  $\mathbf{r}_i$  has been presented in 4.2.

In this chapter, we mainly consider the following motion-planning problem.

*Motion planning problem:* For all  $P_i$ s,  $i = 1, \dots, n$ , given  $\mathcal{S}$  and  $\mathcal{T}$ , find the optimal collision-free path  $\pi^*(\mathcal{S}, \mathcal{T})$  that achieves the minimal total travel time of all nanowires. We also need to compute electrode control  $\mathbf{u}(t)$  at time  $t$  to steer all nanowires to follow a given  $\pi^*(\mathcal{S}, \mathcal{T})$ .

### 5.3 Motion control of multiple nanowires

The simultaneous steering multiple nanowires aims to compute the electrode voltages to steer all nanowires to reach the target location while compensating the fluid disturbance. Similar in Section 4.3, to formulate the motion equations for all  $n$  nanowires, we first re-index the electrodes into a one-dimensional  $N^2$ -element array with a column-wise order; see Figure 4.1. We denote the electrical field at  $\mathbf{r}_j(t)$  by the powered  $i$ th electrode as  $\mathbf{E}_i(\mathbf{r}_j(t)) = [E_{x_i}(\mathbf{r}_j(t)) \ E_{y_i}(\mathbf{r}_j(t))]^T$ ,  $j = 1, \dots, n$ , and the corresponding controlled electrode voltage as  $\mathbf{u}_c \in \mathbb{R}^{N^2}$ , which is also re-ordered column-wise



from  $\mathbf{u}$  in (2.1). By defining a matrix

$$\mathbf{B} = \begin{bmatrix} C_1 \mathbf{E}_1(\mathbf{r}_1(t)) & \cdots & C_1 \mathbf{E}_{N^2}(\mathbf{r}_1(t)) \\ \vdots & \ddots & \vdots \\ C_n \mathbf{E}_1(\mathbf{r}_n(t)) & \cdots & C_n \mathbf{E}_{N^2}(\mathbf{r}_n(t)) \end{bmatrix}, \quad (5.1)$$

we re-write (4.1) for all nanowires as

$$\dot{\mathbf{q}} = \mathbf{B} \mathbf{u}_c, \quad (5.2)$$

where  $\mathbf{B} \in \mathbb{R}^{2n \times N^2}$ . Every two rows in (5.2) represent one nanowire's equation of motion.

We define tracking error  $\mathbf{e}(t) = \mathbf{q}(t) - \mathbf{q}_d(t)$  and consider the error prediction  $\hat{\mathbf{e}}(t) = \mathbf{K} \mathbf{e}(t) + \mathbf{K}_d \dot{\mathbf{e}}(t)$ , where  $\mathbf{K} = \text{diag}(k_1, \dots, k_{2n})$ ,  $k_i > 0$ ,  $i = 1, \dots, 2n$ , and  $\mathbf{K}_d = \text{diag}(k_{d_1}, \dots, k_{d_{2n}})$ ,  $k_{d_j} > 0$ ,  $j = 1, \dots, 2n$  are two constant gain matrix. Given the desired velocity  $\dot{\mathbf{q}}_d$ , a least-square problem is formulated to obtain control input  $\mathbf{u}_c$  in (5.2)

$$\min_{\mathbf{u}_c(t)} \|\dot{\mathbf{q}}(t) - \dot{\mathbf{q}}_d(t) + \hat{\mathbf{e}}(t)\|_2. \quad (5.3)$$

To obtain the voltage inputs that are physically feasible, we modify (5.3) by considering the following optimization problem.

$$\begin{aligned} \min_{\mathbf{u}_c(t)} & \|\mathbf{B}(t) \mathbf{u}_c(t) - \dot{\mathbf{q}}_d(t) + \mathbf{K} \mathbf{e}(t) + \mathbf{K}_d \dot{\mathbf{e}}(t)\|_2 \\ \text{subject to} & \quad u_{\min} \leq \|\mathbf{u}_c(t)\|_{\infty} \leq u_{\max}, \end{aligned} \quad (5.4)$$

where  $u_{\min}$  and  $u_{\max}$  are respectively the lower- and upper-bound of the applied voltages.  $\dot{\mathbf{e}}(t)$  is implemented by numerical discrete-time derivative. The inclusion of the error prediction into (5.3) compensates the predicted error for the next time period using the past two step error measurements. A quadratic programming technique is used to solve (5.4). We will apply this motion control to the motion planning algorithms in the next section.

## 5.4 Multiple nanowire motion planning

In this section, we present the sparse RRT\* motion planner (i.e., SRRT\*) to generate the asymptotically time-optimal trajectory  $\pi^*(\mathcal{S}, \mathcal{T})$  for all nanowires. Although the optimized trajectory minimizes the total traveling time of all nanowires, other types of cost function can be also applied.

### 5.4.1 Roadmap formulation

The roadmap aims to solve the motion planning problem defined in Section 5.2 by providing a discrete, graphical representation of the 2D continuous configuration space. We use the sparse structure similar to [126] to maintain only a sparse set of samples to make the computation efficient.

As the configuration space is 2D continuous plane, we discretize atomic cell  $\mathcal{A}_a$  (with size of  $L \times L$ ) into many  $a \times a$  grids. We denote  $\delta_s = L/a$  as the sparse resolution, and  $\mathcal{B}_1(\mathbf{q}, \delta_s)$  as the *witness area*, a set of grids for each individual nanowire at position  $\mathbf{q}$ . Every grid is considered as a local neighborhood of each nanowire's witness position. We define mapping  $w(\mathbf{q})$  which finds the witness area corresponding state  $\mathbf{q}$ . We denote *witness* as  $w_{\min}(\mathbf{q})$  and it represents the least-cost node inside  $\mathcal{B}_1(\mathbf{q}, \delta_s)$ , and  $w_{\text{peer}}(\mathbf{q})$  as other nodes if exist in  $\mathcal{B}_1(\mathbf{q}, \delta_s)$ . The proposed algorithm will maintain a single node in the tree to represent that witness, and that node will have the best path cost from the root within each grid for each nanowire. The grids are used to only keep record the witness area and thus maintain a sparse structure of the nodes in the tree. It does not affect sampling, steering, and rewiring processes that are operated in the continuous space.

We denote the configuration space as a tree structure  $\mathcal{G} = \{V, E\}$ , where  $V$  is the set of vertices that represents position  $\mathbf{q}$  and  $E$  represents directed edge transitions connecting vertices. We use Euclidean distance as metric and the  $\delta$ -radius closed hyperball centered at  $\mathbf{q}$  denotes as  $\mathcal{B}_2(\mathbf{q}, \delta) = \bigcup_{i=1}^n \mathcal{B}_2(\mathbf{q}_i, \delta)$ . Then, we define a collision

checker:

**Definition 5.1.** *Given an individual state  $\mathbf{q}$ , a collision checker returns whether  $\mathbf{q}$  has at least  $R_o$ -distance away from each nanowire position, i.e.,  $\mathbf{r}_i \notin \mathcal{B}_2(\mathbf{r}_j, R_o)$ ,  $i \neq j$ ,  $i, j = 1, 2, \dots, n$ .*

To create roadmap, the sampled configurations must be connected by edges with aid of a local planner and thus, we define local planner.

**Definition 5.2.** *Given two states, a local planner `steer` returns a local collision-free path between the states.*

### 5.4.2 The SRRT\* algorithm

The SRRT\* motion planner is illustrated in Algorithm 5. The algorithm first tries to steer the system from the starting location to the target location by using the local planner (line 3). This initial steering has exponentially fast convergence profile that minimizes the error between starting and target configurations. If all the nanowire reach their targets, then the global variable *reach* is marked as true; otherwise, *reach* is marked as false. Unlike RRT, SRRT\* uses a heuristic sampling strategy with higher probability of avoid collision (line 4); see Section 5.4.3. After generating the random sample  $\mathbf{q}_{\text{rand}}$ , the `Best_Near` function (Algorithm 6) selects the best parent node in the tree for providing a good quality path (line 5). The nodes of the tree are split into two sets, the active vertices  $V_{\text{act}}$  and the inactive vertices  $V_{\text{inact}}$  (line 1).  $V_{\text{inact}}$  keeps record the nodes that are not the witness, i.e.,  $\mathbf{q}_{\text{peer}} \in \{w_{\text{peer}}(\mathbf{q})\}$ , while the  $V_{\text{act}}$  are the witness node in each witness area, i.e.,  $\{w_{\text{min}}(\mathbf{q})\}$ . Next, SRRT\* tries to steer the system from the selected  $\mathbf{q}_{\text{parent}}$  to  $\mathbf{q}_{\text{rand}}$  (line 6). If any new node is added to the tree, then the algorithm steers the system from the new generated  $\mathbf{q}_{\text{new}}$  to the target configuration (line 7). Finally, the algorithm outputs the best trajectory  $\pi^*$  from  $\mathcal{S}$  to  $\mathcal{B}_1(\mathcal{T}, \delta_s)$  according to the updated  $\mathcal{G}$  (line 8).

---

**Algorithm 5:** SRRT\* motion planning and control

---

**Input :**  $\mathcal{S}, \mathcal{T}, R_o, R_e, \delta_s, \delta_{bn}$   
**Output:**  $\pi^*$   
1  $V_{\text{act}} \leftarrow \mathcal{S}, V_{\text{inact}} \leftarrow \emptyset, V \leftarrow (V_{\text{act}} \cup V_{\text{inact}})$   
2  $\mathcal{G} = \{V, E \leftarrow \emptyset\}, w_0 \leftarrow \mathcal{S}, W \leftarrow \{w_0\}$   
3  $reach \leftarrow \text{Initial\_Steer}(\mathcal{S}, \mathcal{T}, R_o, R_e)$   
**for** Max\_iterations **do**  
4      $\mathbf{q}_{\text{rand}} \leftarrow \text{Heuristic\_sampling}(reach, R_o, R_e)$   
5      $\mathbf{q}_{\text{parent}} \leftarrow \text{Best\_Near}(V_{\text{act}}, \mathbf{q}_{\text{rand}}, \delta_{bn})$   
6      $\mathbf{q}_{\text{new}} \leftarrow \text{SteerRew}(\mathbf{q}_{\text{parent}}, \mathbf{q}_{\text{rand}}, \delta_s, \delta_{bn}, R_o)$   
       **if**  $\mathbf{q}_{\text{new}} \neq \emptyset$  **then**  $\text{SteerRew}(\mathbf{q}_{\text{new}}, \mathcal{T}, \delta_s, \delta_{bn}, R_o)$   
8  $\pi^* \leftarrow \text{path\_out}(\mathcal{T}, \delta_s)$

---

The SRRT\* algorithm generates collision-free near asymptotically-optimal path  $\pi^*(\mathcal{S}, \mathcal{T})$  as stated in the following lemma. The proof is followed by the results in [123] and we omit here.

**Lemma 5.1.** *The SRRT\* algorithm is probabilistically complete and asymptotically near optimal if*

$$\frac{\delta_{bn}}{\delta_s} > \left[ 2e \left( 1 + \frac{1}{d} \right) \right]^{\frac{1}{d}}, \quad (5.5)$$

where  $d = 2n$  is the dimension of the configuration space.

The SRRT\* algorithm keeps the RRT\* procedure, while keeping the sparse operation that does not violate the probabilistically complete and asymptotically optimal condition. Thus, it is not necessary to keep all samples as nodes in the data structure, but the lowest-cost ones in the witness areas in the vicinity of the path, so as to get arbitrarily close to  $\pi^*$ . Thus, it is possible for a sparse data structure with a finite set of states to sufficiently represent the whole state space.

---

**Algorithm 6:** Best\_Near

---

**Input :**  $V_{\text{act}}, \mathbf{q}_{\text{rand}}, \delta_{bn}$   
**Output:**  $\mathbf{q}_{\text{parent}}$   
 $\mathcal{Q}_{\text{near}} \leftarrow \text{Near}(V_{\text{act}}, \mathbf{q}_{\text{rand}}, \delta_{bn})$   
**if**  $\mathcal{Q}_{\text{near}} = \emptyset$  **then**  $\mathbf{q}_{\text{parent}} \leftarrow \text{Nearest}(V_{\text{act}}, \mathbf{q}_{\text{rand}})$   
**else**  $\mathbf{q}_{\text{parent}} \leftarrow \arg \min_{\mathbf{q} \in \mathcal{Q}_{\text{near}}} \text{cost}(\mathbf{q})$

---

Algorithm 6 shows the `Best_Near` parent node selection. As illustrated in Figure 5.1, `Near` function returns node-set  $Q_{\text{near}}$  that includes  $q \in \mathcal{B}_2(q_{\text{rand}}, \delta_{bn})$ , and  $q \in V_{\text{act}}$ . Then, the best path cost node from the root  $\mathcal{S}$  is selected as the parent node  $q_{\text{parent}}$ . If there is no node in  $\mathcal{B}_2(q_{\text{rand}}, \delta_{bn})$ , then the nearest node in  $V_{\text{act}}$  from  $q_{\text{rand}}$  is selected as  $q_{\text{parent}}$ .

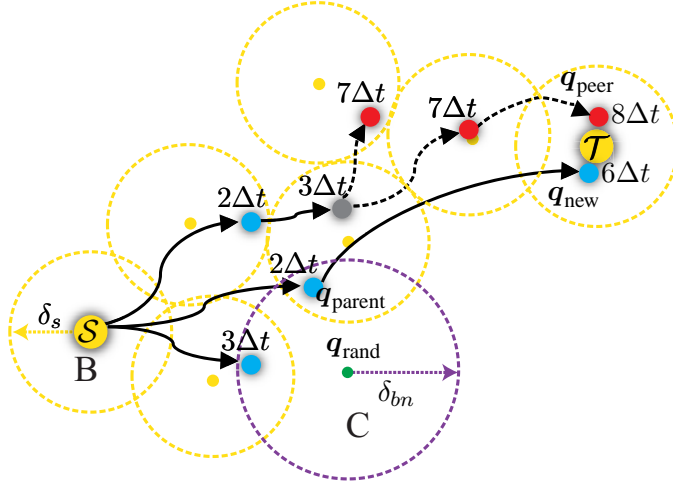


Figure 5.1: An example of `Best_Near` parent node selection and `drain` pruning. A tree structure with witness area  $\mathcal{B}_1(q, \delta_s)$  is centered at the yellow dot with grid length  $\delta_s$ . The nodes of the tree are the shadowed dots (blue, grey and red dots), and the arrow lines indicate the tree edges. The blue dots are witnesses, the grey dot is the inactive node, and the red dots show the nodes that are pruned in `drain`. All nodes  $q \in \mathcal{B}_2(q_{\text{rand}}, \delta_{bn})$  and  $q \in V_{\text{act}}$  are checked to find  $q_{\text{parent}}$ , which node has the lowest-cost ( $2\Delta t$ ) from root  $\mathcal{S}$ . After steering from  $q_{\text{parent}}$ , a new state  $q_{\text{new}}$  is added into tree with cost  $6\Delta t$ . A feasible solution is also generated and  $\text{MinCost}$  is updated as  $6\Delta t$ . Any leaf node is iteratively pruned along the tree path until reaching any witness node with cost less than  $\text{MinCost}$ . In this case, the red nodes, the grey node and the dashed edges are removed.

### 5.4.3 Heuristic sampling

The sampling strategy is explained in Algorithm 7. If there is any feasible solution that has been generated, then the uniform sampling will be conducted. For shortest distance problem, the sampling heuristic in informed  $RRT^*$  [138] can be applied after an initial solution is found. Informed  $RRT^*$  focuses on sampling new nodes inside an ellipsoid which cost is no more than the initial solution. Inspired by [138], a trimming

technique in Section 5.4.4 will prune the tree if the node has cost greater than the initial condition.

---

**Algorithm 7: Heuristic\_sampling**


---

**Input** :  $reach, R_o, R_e$

**Output:**  $\mathbf{q}_{\text{rand}}$

$p \leftarrow \text{rand}(0, 1)$

**if**  $reach$  **or**  $p > 1/|V_{\text{act}}|$  **then**  $\mathbf{q}_{\text{rand}} \leftarrow \text{UniformSample}$

**else**  $\mathbf{q}_{\text{rand}} \leftarrow \mathbf{q}_{\text{collision}} - \alpha \nabla U(\mathbf{q}_{\text{collision}})$

---

If there is no feasible solution, the negative gradient of a potential function is used to generate heuristic sample. The potential function of nanowire  $P_i$  is

$$U_i = \mathbf{e}_i^T \mathbf{e}_i + \mathbf{R}_i^T \mathbf{R}_i, \quad (5.6)$$

where  $\mathbf{e}_i = \mathbf{r}_i - \mathbf{r}_{iT}$ ,

$$\mathbf{R}_i = \frac{\mathbf{d}_i^T \mathbf{d}_i - R_e^2}{\mathbf{d}_i^T \mathbf{d}_i - R_o^2} (\text{sign}(R_e - \mathbf{d}_i) + 1), \quad (5.7)$$

$\mathbf{d}_i = \mathbf{r}_i - \mathbf{r}_j$ ,  $i, j = 1, 2, \dots, n$  and  $j \neq i$  is the distance between the nanowire  $P_i$  to all the other nanowires. The first term in (5.6) captures the attractive potential, while the second term is the repulsive potential when other nanowires are treated as obstacles. Constant  $R_o$  is the radius of the obstacle (i.e., the length of the nanowire) and  $R_e$  is the effective radius of the repulsive potential, namely, distance when nanowire  $P_i$  is affected by nanowire  $P_j$ ,  $i \neq j$ ,  $i, j = 1, \dots, n$ . Note, elements of  $\mathbf{d}_i$  cannot be less than  $R_o$ , otherwise collision will occur. In Algorithm 7, the sampling point  $\mathbf{q}_{\text{rand}}$  has a probability of  $1/|V_{\text{act}}|$  to be in the gradient descent direction of the potential function (5.6).

#### 5.4.4 Steering and rewiring

Algorithm 8 demonstrates how to propagate the sparse-tree structure. Function  $\text{steer}_{\text{wit}}$  ( $\mathbf{q}, \mathbf{q}_d, \delta_s$ ) uses the local planner defined in Section 5.4.1 to steer the states that starting from  $\mathbf{q}$  towards to  $\mathbf{q}_d$ . It stops integration until the states reach another witness

area other than the witness area of  $\mathbf{q}$ , and generates a new state  $\mathbf{q}_{\text{new}}$ . If there is any feasible solution (i.e.,  $\text{reach} = \text{true}$ ), the cost of  $\mathbf{q}_{\text{new}}$  is compared with  $\text{MinCost}$ , the minimum cost of the existing solution. If  $\text{cost}(\mathbf{q}_{\text{new}}) > \text{MinCost}$ , then no more nodes are added to the tree.  $C_{\text{Free}}$  is false if collision occurs using the collision checker, and  $\mathbf{q}_{\text{new}}$  returns the previous states before collision. If there is no collision, and there is no existing witness in the witness area (i.e.,  $w_{\text{new}} = \emptyset$ ), then a `sparse_rewire` procedure updates  $\mathbf{q}_{\text{new}}$  as the best cost nodes in its witness area, connects to its corresponding parents, and prune the tree within the  $\delta_{bn}$  distance of  $\mathbf{q}_{\text{new}}$  while maintain the sparse structure. If there exists other states in the witness area of  $\mathbf{q}_{\text{new}}$  (i.e.,  $w_{\text{new}} \neq \emptyset$ ), and the cost of  $\mathbf{q}_{\text{new}}$  is less than the existing least-cost witness, then the new least-cost node is added to the tree as a witness (an active node), its corresponding witness is updated, and the old least-cost one is moved from active-node set to the inactive-node set. Finally, the `drain` function prunes the tree structure starting from the tree leaves and method `AllLeaf` returns all the leaf nodes of the tree.

Algorithm 9 is similar to the rewiring of RRT\*, which tries to rewire the current node  $\mathbf{q}$  to the existing nodes in  $\mathbf{Q}_{\text{near}}$ . It also checks whether there are any better parents of the current node. But Algorithm 9 has the following differences from the RRT\* algorithm: First, the algorithm finds the best ancestor  $\mathbf{q}_{\text{near}}$  in  $\mathcal{B}_2(\mathbf{q}, \delta_{bn})$  that steers to  $\mathbf{q}_{\text{temp}}$  within witness area  $\mathcal{B}_1(\mathbf{q}, \delta_s)$ . Then the new node  $\mathbf{q}$  is updated as the best cost nodes in its witness area, and added into the tree. Variable *rewit* returns true if there is a collision-free path from  $\mathbf{q}_{\text{near}}$ , the ancestor node of current node, to  $\mathcal{B}_1(\mathbf{q}, \delta_s)$ . Variable *re* marks whether the steer function can steer  $\mathbf{q}_{\text{near}}$  to the exact same (or within a smaller range of) state  $\mathbf{q}$  without collision. Second, the algorithm tries to connect the newly updated  $\mathbf{q}$  to other nodes in  $\mathbf{Q}_{\text{near}}$  that are not ancestor of  $\mathbf{q}$ . If the cost of the new node  $\mathbf{q}_{\text{new}}$  is less than the existing node and *re* is true, then the children of existing node  $\mathbf{q}_{\text{near}}$  are connected to  $\mathbf{q}_{\text{new}}$ , and the cost of the children will be updated. If *re* is false but *rewit* is true, then a new node is added as a witness in the tree, and move  $\mathbf{q}_{\text{near}}$  into inactive set. The least-cost witness  $w_{\text{min}}$ , the active set  $V_{\text{act}}$ , and inactive set  $V_{\text{inact}}$

**Algorithm 8: SteerRew**


---

**Input** :  $q, q_d, \delta_s, \delta_{bn}, R_o$   
**Output**:  $q_{add}$

$iter \leftarrow \text{rand}(1, \text{Max\_iter})$   
**for**  $i = 1$  **to**  $iter$  **do**

$(q_{new}, C_{Free}) \leftarrow \text{steer}_{wit}(q, q_d, \delta_s)$   
**if**  $\text{reach and cost}(q_{new}) > \text{MinCost}$  **then** **break**  
**if**  $C_{Free}$  **then**  

$w_{new} \leftarrow w(q_{new})$   
**if**  $w_{new} = \emptyset$  **then**  

$Q_{near} \leftarrow \text{Near}(V_{act}, q_{new}, \delta_{bn})$   
 $q_{add} \leftarrow \text{sparse\_rewire}(q_{new}, Q_{near}, \delta_s)$

**else**  

$q_{peer} \leftarrow w_{min}(q_{new})$   
**if**  $\text{cost}(q_{new}) < \text{cost}(q_{peer})$  **then**  

$V_{act} \leftarrow V_{act} \setminus \{q_{peer}\}, V_{inact} \leftarrow V_{inact} \cup \{q_{peer}\}$   
 $Q_{near} \leftarrow \text{Near}(V_{act}, q_{new}, \delta_{bn})$   
 $q_{new} \leftarrow \text{sparse\_rewire}(q_{new}, Q_{near}, \delta_s)$

**else break**

**else**  $q_{collision} \leftarrow q_{new}, \text{break}$   
 $q \leftarrow q_{new}$

$Q_{leaf} \leftarrow \text{AllLeaf}, \text{drain}(Q_{leaf})$

---

are updated correspondingly.

Function `drain` illustrated by Algorithm 10 prunes the inactive node set to keep the tree structure sparse [126]. It also prunes the leaf nodes with higher cost than  $\text{MinCost}$ , which by no means has any child to be added to the tree since the cost is already greater than the existing solution. This `drain` heuristic improves the convergence rate and final-solution quality. The `drain` function starts from all the leaves of the tree, and iteratively prunes each path of the tree until reaching any witness node with cost smaller than  $\text{MinCost}$ . Figure 5.1 shows an examples of the pruning process.

## 5.5 Simulation and experimental results

In this section, we first present simulation results and the algorithm analysis, and then show experiments to demonstrate the near time-optimal simultaneous motion control



---

**Algorithm 9:** sparse\_rewire
 

---

**Input** :  $q, Q_{\text{near}}, \delta_s$   
**Output:**  $q_{\text{add}}$

**for each**  $q_{\text{near}}$  **in**  $Q_{\text{near}}$  **and**  $q_{\text{near}}$  **is ancestor of**  $q$  **do**

- $(q_{\text{temp}}, \text{rewit}, re) \leftarrow \text{steer}(q_{\text{near}}, q, \delta_s)$
- if**  $\text{rewit}$  **and**  $\text{cost}(q_{\text{temp}}) < \text{cost}(q)$  **then**
  - $q \leftarrow q_{\text{temp}}, q_{\text{parent}} \leftarrow q_{\text{near}}$

$w_{\min}(q) \leftarrow q, q_{\text{add}} \leftarrow q$   
 $V_{\text{act}} \leftarrow V_{\text{act}} \cup q, E \leftarrow E \cup \overline{q_{\text{parent}} \rightarrow q}$

**for each**  $q_{\text{near}}$  **in**  $Q_{\text{near}}$  **and**  $q_{\text{near}}$  **is not ancestor of**  $q$  **do**

- $(q_{\text{new}}, \text{rewit}, re) \leftarrow \text{steer}(q, q_{\text{near}}, \delta_s)$
- if**  $\text{rewit}$  **and**  $\text{cost}(q_{\text{new}}) < \text{cost}(q_{\text{near}})$  **then**
  - $V_{\text{act}} \leftarrow V_{\text{act}} \setminus \{q_{\text{near}}\}, V_{\text{inact}} \leftarrow V_{\text{inact}} \cup \{q_{\text{near}}\}$
  - $w_{\min}(q_{\text{new}}) \leftarrow q_{\text{new}}, V_{\text{act}} \leftarrow V_{\text{act}} \cup q_{\text{new}}$
  - if**  $re$  **then**
    - $q_p \leftarrow \text{Parent}(q_{\text{near}}), E \leftarrow (E \setminus \overline{q_p \rightarrow q_{\text{near}}})$
    - $E \leftarrow E \cup \overline{q \rightarrow q_{\text{new}}} \text{update\_Tree\_Cost}(q_{\text{new}})$

---



---

**Algorithm 10:** Drain
 

---

**Input** :  $Q_{\text{leaf}}$

**for each**  $q$  **in**  $Q_{\text{leaf}}$  **do**

- while**  $q \in V_{\text{inact}}$  **or**  $\text{cost}(q) > \text{MinCost}$  **do**
  - $q_p \leftarrow \text{Parent}(q), E \leftarrow (E \setminus \overline{q_p \rightarrow q})$
  - $V_{\text{inact}} \leftarrow V_{\text{inact}} \setminus q, V_{\text{act}} \leftarrow V_{\text{act}} \setminus q$
  - $q \leftarrow q_p$

---

and planning of multiple nanowires.

### 5.5.1 Simulation results

We first demonstrate the performance of the SRRT\* algorithm through simulation results. In the simulation, we set  $L = 600 \mu\text{m}$  and  $R = 150 \mu\text{m}$  to match the dimensions of the micro-fluidic device in experiments. For an  $N \times N$  electrode array, we first specify the number of nanowires. We distribute these nanowires in randomly chosen atomic cells. The starting and targeted locations for each nanowire are also randomly

determined in these cells. To eliminate the performance dependency on the simulation specifications and procedures, we conduct 40 runs of each configuration for the same algorithm and then compute the statistics in these simulation runs. The simulation are running on a computer with Intel Core i7-4700 CPU at 2.40 GHz and 4G RAM memory.

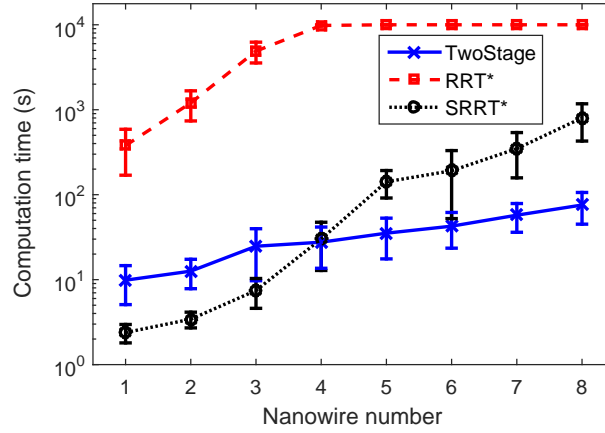


Figure 5.2: Run-time comparison among SRRT\*, TwoStage and RRT\* with different numbers of nanowires in a  $6 \times 6$  electrode array. The last five data points for the RRT\* algorithm are clamped to  $10^4$  s due to reaching the maximum computation time limit.

We conduct simulation testing for different number of nanowires: Figure 5.2 shows the computation times (mean and one standard deviation) of the first time stamp when the results hit the final solution after constraints for the SRRT\* algorithm and the RRT\* algorithm [123], together with TwoStage [80] algorithm for a  $6 \times 6$  ( $N = 6$ ) electrode array. The RRT\* algorithm is implemented by using the same control scheme discussed in Section 4.3. To obtain the results in the figure, a maximum iteration number of 10,000 and a maximum running time of 10,000 s are used. The lower computation times for first reaching the final solution under the SRRT\* and TwoStage algorithms show they perform more efficiently than the RRT\* algorithm. Figure 5.3 shows the corresponding travel-time comparison among the asymptotically optimal-time trajectory using the RRT\* algorithm, proposed SRRT\* algorithm, and the shortest-distance trajectory using TwoStage with different numbers of nanowires in a  $6 \times 6$  electrode array. The RRT\* result is obtained with maximum running time of 50,000 s and maximum

10,000 iterations, while SRRT\* has the same constraints as in the previous results in Figure 5.2. The nanowires' starting and targeting configurations are randomly chosen, but kept same for the compared algorithms. The results show the SRRT\* can converge to the optimal solution much faster than RRT\*, and the traveling time obtained by SRRT\* is more than two times shorter than the shortest-distance trajectory. It is clearly demonstrated that for a small number of nanowires (e.g.,  $n = 2, 3$ ), SRRT\* algorithms can be used in online implementation. However, when the number of nanowires increases, the TwoStage algorithm outperforms the RRT\* and SRRT\* algorithms due to the enforced straight-line heuristic. In particular, when more than five nanowires are routed, the RRT\* algorithm cannot even successfully generate the planning results before reaching the maximum time constraint, while the SRRT\* and the TwoStage algorithms show robust performance.

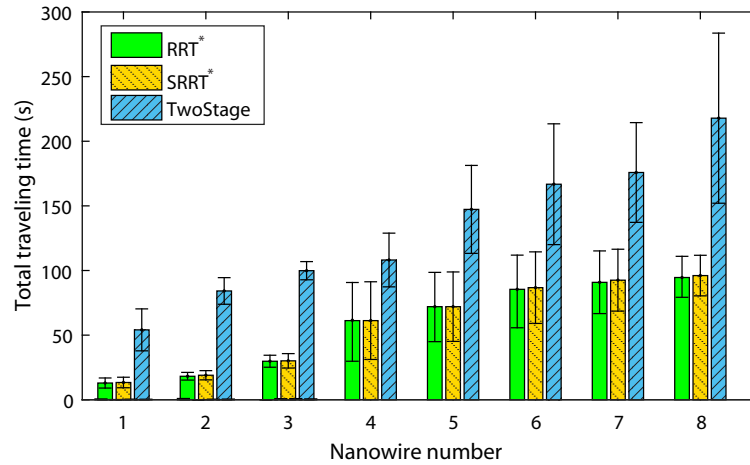


Figure 5.3: Travel-time comparison among the minimum-time RRT\* algorithm, the SRRT\* algorithm, and the TwoStage algorithms with different numbers of nanowires in a  $6 \times 6$  electrode array.

Figure 5.4 further shows the motion-planning trajectory of controlling 4 nanowires in opposite target directions, 8 nanowires in twisted target directions, and 9 nanowires from one atomic cell to different target directions. In [80], the maximum number of nanowires that could be steered at one time is bounded by 8 due to the TwoStage algorithm. The results in Figure 5.4(c) clearly demonstrate that the SRRT\* motion planner is able to handle more than 8 nanowires simultaneously and therefore, it is

more scalable for the motion planning and control of a large number of nanowires.

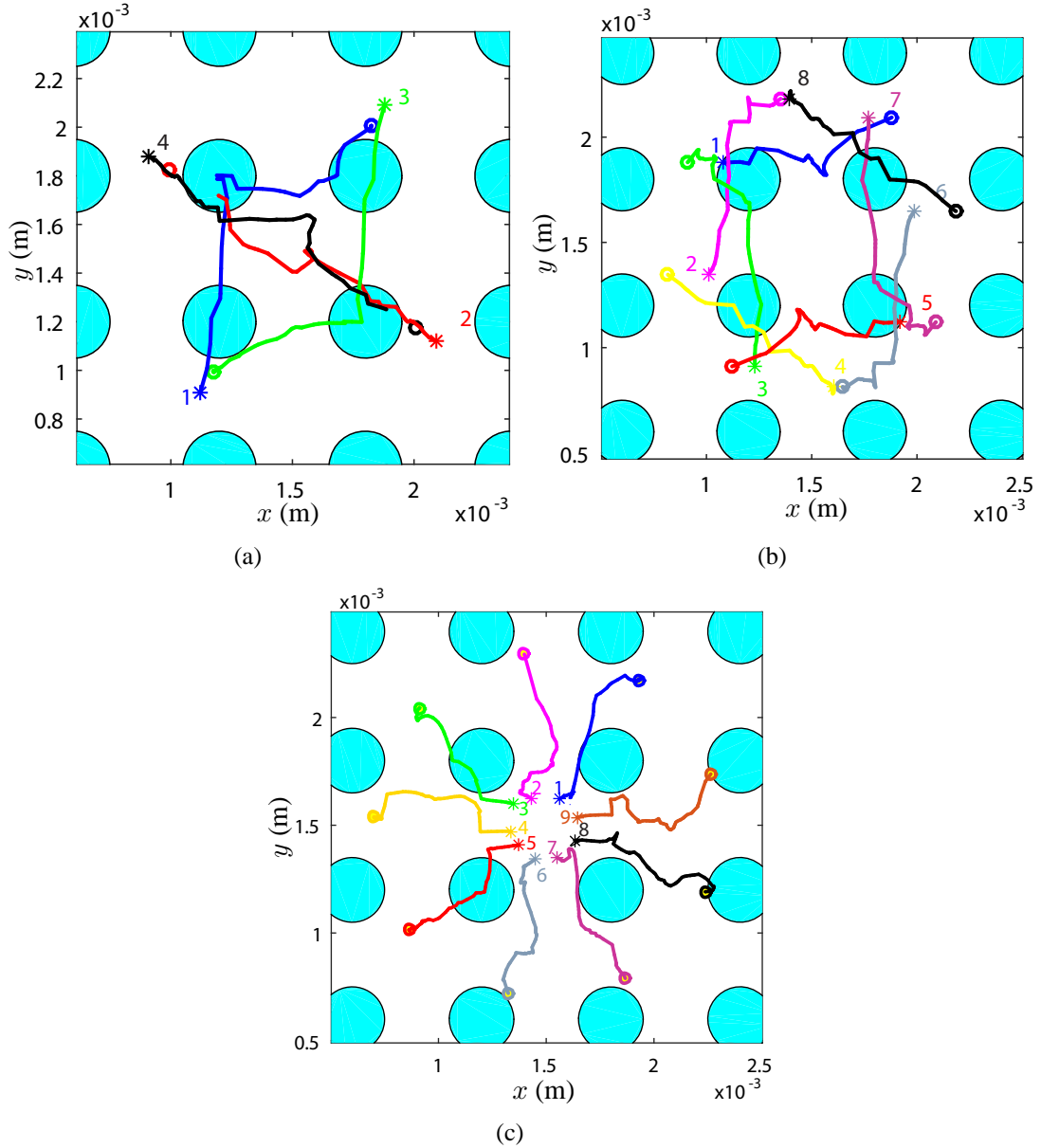


Figure 5.4: Simulated trajectories for motion-planning and control of (a) 4 nanowires in opposite target directions, (b) 8 nanowires in twisted target directions, and (c) 9 nanowires from one atomic cell to different target directions. The “\*” and “o” markers indicate the nanowires initial and final positions, respectively.

### 5.5.2 Experimental results

The experimental setup is the same in Section 4.5, as shown in Figure 3.3. The micro-fluidic device is shown in Figure 4.8(a). Figure 4.8(b) shows a view of the electrodes

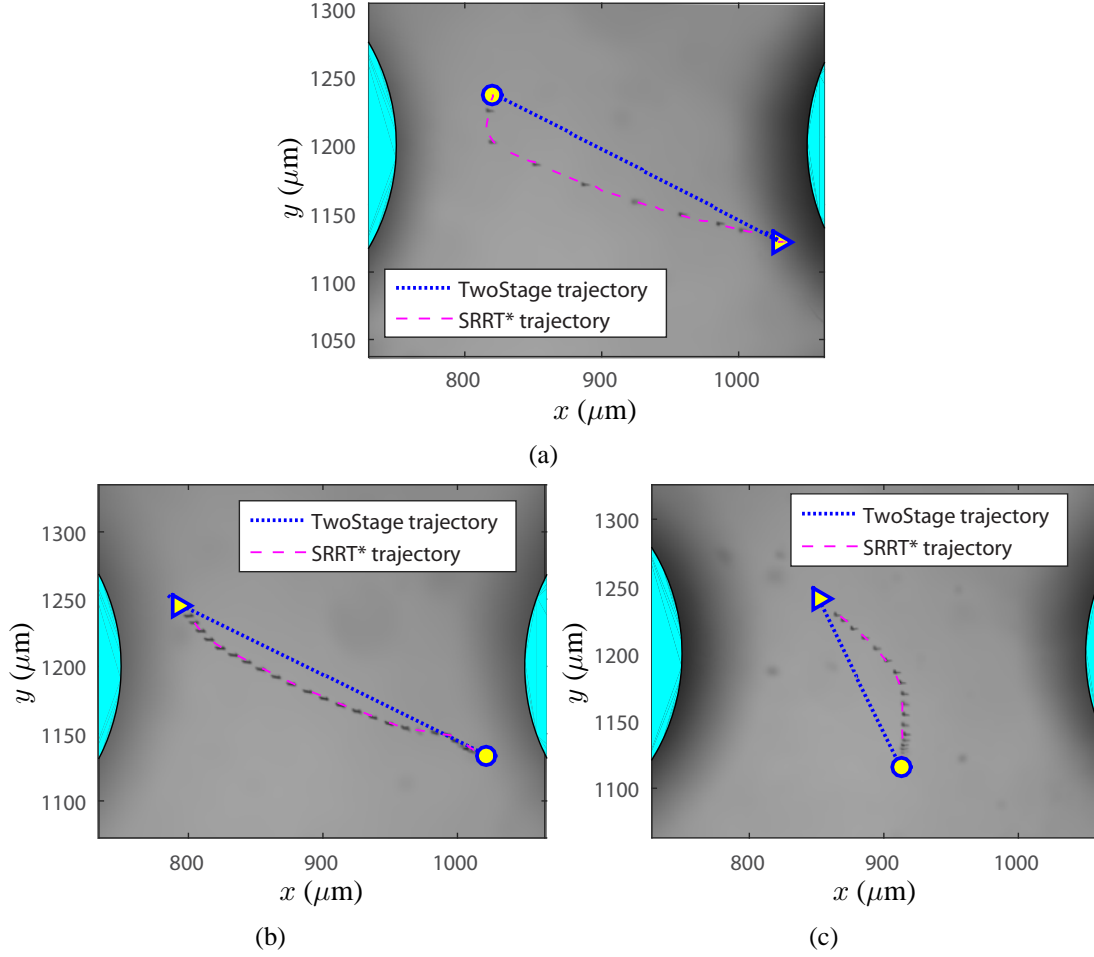


Figure 5.5: Experimental comparison between SRRT\* and TwoStage trajectories for motion planning and control of one nanowire crossing an atomic-cell boundary. The overlaid nanowire trajectories are obtained by using SRRT\* algorithm and overlaying the nanowire images evenly spaced every 5 seconds. The total traveling times are (a) SRRT\* : 40.8s and shortest path: 157.2s. (b) SRRT\* : 137.2s and shortest path: 345.7s. (c) SRRT\* : 89.1s and shortest path: 158.7s. The “▷” and “○” marks indicate the nanowires’ initial and final positions, respectively.

on the bottom surface of the micro-fluidic device with  $4 \times 4$  electrode arrays. The entire device is mounted on a motorized, computer-controlled microscope XY stage (Prior ProScan III) on an inverted microscope (Olympus IX71). Bright-field images are recorded using a  $40\times$  objective. To control the electrode array, an embedded system (NI cRIO 9074) is used with visual feedback of the nanowire positions. We use silicon nanowires suspended in the heavy viscosity mineral oil to perform experiments. The dimensions of the silicon nanowires used are approximately 5 to 18  $\mu\text{m}$  in length and

100 to 200 nm in diameter. Zeta-potential values for each nanowire are estimated at the start of the experiments by applying a constant potential for a few seconds and recording the motion of the nanowires.

We first demonstrate the near time-optimal motion planning by the SRRT\* algorithm. Figure 5.5 shows a series of experimental results of steering one nanowire from a similar starting position to a target location. These nanowire trajectories go across the atomic-cell boundaries. The experiments are conducted by first steering the nanowire from starting to target locations by an online SRRT\* motion planning and control scheme. For comparison purpose, we steer the same nanowire back to the original starting location and then drive the nanowire from the same starting point to the target point using the pre-computed shortest-distance trajectory by the TwoStage algorithm in Chapter 4. The traveling time of the nanowires under these two algorithms are listed in Table 5.1. It is interesting to see that even the traveling distances under the SRRT\* planner are larger than those shortest-distance trajectories under the TwoStage algorithm, the total traveling times are much shorter. It takes around 2-4 times longer under the TwoStage planner than those under the SRRT\* planner.

Table 5.1: Traveling time (s) comparison between the SRRT\* and TwoStage algorithms.

	Figure 5.5(a)	Figure 5.5(b)	Figure 5.5(c)
SRRT*	40.8	137.2	89.1
TwoStage	157.2	345.7	158.7

Figure 5.6 further compares the performance of the SRRT\* and TwoStage planners for steering two nanowires simultaneously. Again, we tried to drive these two nanowires from about the same starting locations to the same target locations. The total traveling time under the SRRT\* planner is 20.4 s, while the time for the shortest-path trajectory under the TwoStage planner is 273.3 s. From Figure 5.6, it is also clearly noted that the shorter traveling time actually takes a much longer traveling distance

than the shortest-distance trajectory. This is because traveling along the straight-line does not achieve the fastest velocity under electric field distribution. These experiments clearly demonstrate the feasibility and performance of the time-optimal motion planning and control for simultaneously steering multiple nanowires.

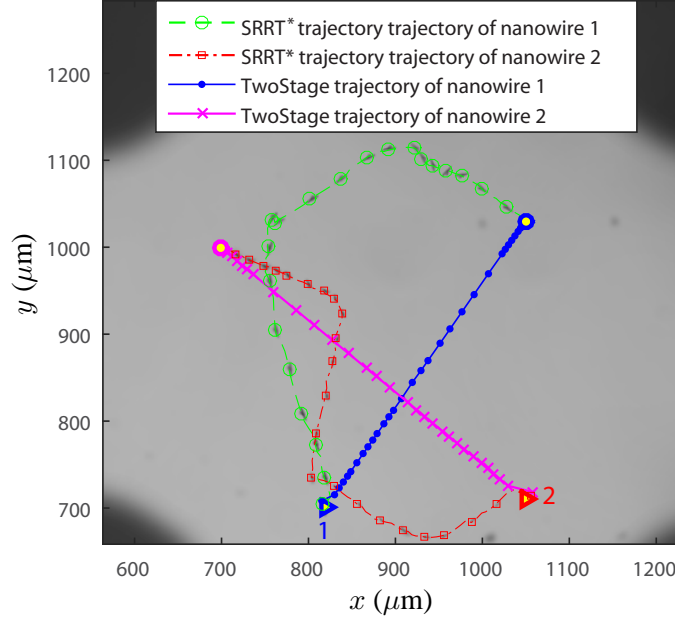


Figure 5.6: Experimental motion-trajectory comparison between the SRRT\* and TwoStage planners for steering two nanowires simultaneously from the same initial and ending locations. The overlaid nanowire trajectories are obtained by using SRRT\* algorithm and overlaying the nanowire images evenly spaced every 1 seconds, and the TwoStage trajectories are marked evenly spaced every 10 seconds. The “▷” and “○” marks indicate the nanowires’ initial and final positions, respectively.

## 5.6 Conclusion and future work

In this chapter, a near-time-optimal motion planning scheme for steering multiple nanowires under electric-field in liquid suspension is developed. The proposed SRRT\* motion-planning algorithm takes advantage of the sparse RRT structure to generate computationally efficient high-quality paths while at the same time trying to maintaining the optimality. The use of the potential fields in the planning also helped quickly generate a feasible solution. Simulation and experimental results demonstrated that

the SRRT\* algorithm reduces the computational complexity significantly when compared with the RRT\* algorithm. We have demonstrated the experimental performance of the proposed online motion-planning and control scheme by steering two nanowires simultaneously in a micro-fluidic device. We are currently working to improve the computational efficiency of the algorithms to cope with more nanowires. A scheme similar to SST\* in [126] might be adopted to enhance the proposed algorithm for online real-time motion-planning and control of more than 4 nanowires simultaneously. We also plan to conduct further extensive experiments as future work.



## Chapter 6

# Automated Characterization, Manipulation, and Assembly of Nanowires

### 6.1 Introduction

1D nano-materials, such as nanowires, nanotubes, and nanorods, have attracted growing interests for the past two decades due to the numerous potentials offered by their nanoscale size and various physical properties. Especially, single-crystalline silicon nanowires (SiNWs) are attractive semiconducting components for solution processed, low-cost printed electronic devices [139]. Those semiconducting 1D nano-materials are used in various application areas, such as chemical and biological sensors [38], memory devices [140], nano-electronics (e.g., field-effect transistors (FETs) [141]), etc.

Nanowire based high performance FETs have been intensely investigated [42, 142–144]. Crystalline silicon nanowire based FETs are reported to have  $10^4$  to  $10^9$  times higher sensitivity than conventional planar FETs [145–147]. A concept of nanowire thin-film transistors (NW-TFTs) has been discussed in [148–150]. A TFT is a special kind of FETs made by depositing thin films of an active semiconductor layer as well as the dielectric layer and metallic contacts over a supporting but non-conducting substrate. Recent studies have shown that high-performance NW-TFTs and high-frequency circuits can be produced from SiNWs on a variety of substrates, including glass [151] and polymers using a solution assembly process. Especially parylene type C films have been used to fabricate FETs as substrates [152], dielectric layers [153] and encapsulation materials [154, 155]. Besides high performance, parylene based organic

transistors have a number of advantages in its highly biocompatible, biostable, flexible packaging, excellent solution processability, completely conformal with uniform and controllable thickness, and pinhole-free coating. With the substrate and dielectric layer, 1D nano-materials are widely used to bridge the source and drain electrodes to fabricate high-performance TFTs. Typically in NW-TFTs fabrication, multiple nanowires are placed in parallel between the source and drain electrodes. Thus, charges travel from source to drain within single crystals, ensuring high carrier mobility [156].

However, it is well known that the nanowires of the same composition, fabricated within the same batch, and even from the same sample, often exhibit various electrical properties, especially the conductivities of the nanowires may have different orders of magnitude. Therefore, it is crucial to characterize the electrical properties of the nanowires and separate those nanowires according to their characteristics before assembling them into electronic devices, such that the assembled electronic devices will exhibit the desired electrical properties. As noted before, the use of DEP and EP to position and sort micro-nanoparticles in fluid suspension has been reported previously in many publications, and the characterization methods of a vast ensemble of nanoparticles via various scalable techniques are widely investigated. When it compares to the probe based characterization methods, the solution-based characterization methods are efficient and less costly. The solution-based characterization techniques are based on DEPs, which emphasize characterizing large quantities of nanowires and nanotubes for separation [157] and assembly [158], lacking precise and quantified measurement and direct relationship of physical properties of individual nanowires.

Therefore, the goal of this chapter is to propose and demonstrate the potential of the intergraded online process: automated characterization, manipulation, and assembly of nanowires (ACMAN). By extending the contactless electro-orientation spectroscopy (EOS) for single nanowire in [70] and applying the motion control, planning, and manipulation strategies proposed previously in this dissertation, multiple SiNWs

can be characterized, separated, steered, and deposited to form a thin film automatically. To evaluate the integrated process, we fabricated and tested proof-of-concept SiNW-based FETs with different electrical conductivities. The contributions of this chapter are listed as follows.

- Integrating solution based automated online characterization, manipulation, and assembly of 1D nanoparticles. The integrated ACMAN system is capable of processing simultaneous multiple nanowires in a completely online and automated manner. The ACMAN system also precisely controls nanowires with electric-field-induced force, plans their optimal trajectories, and automated assembles each nanowire with its desired physical properties at precise locations.
- The integrated ACMAN system is capable of quantifying the direct relationship of physical properties of each individual nanowire precisely.
- Experimentally demonstrate the feasibility of the proposed ACMAN system to build functional nanodevices. Using ACMAN, SiNWs are separated by their electrical conductivities, and further assembled into FETs. The measurement data of the FETs confirm the separation effectiveness and feasibility of the integrated ACMAN process.

The approaches proposed in this chapter address the challenges of integrated characterization, automated manipulation, and assembly of simultaneous multiple nanowires as a completely automated procedure. The designed scheme enables the scalable, automated, and precise manipulating nanowires to build functional nanodevices, interconnects, and other electronically useful components. Although the SiNWs are used as subjects, the ACMAN process is not limited by materials, and it can be used to characterize, manipulate and assemble any other 1D nano-materials.

## 6.2 Automated characterization of multiple nanowires using electro-orientation spectroscopy

The electrical conductivities of nanowires are among the most important properties for controlling many basic functional characteristics of nanodevices. The nanoparticles of the same composition, even within the same batch of samples, may vary by orders of magnitude in electrical properties, and therefore, efficient and automated characterization of nanowires is needed to be addressed in order to make functional nanodevices in industrial scale.

Characterization of nano materials can be achieved by electrical-transport measurements using microfabricated electrodes [159] or SEM based nanoprobe [160]. These testing techniques require ultra-high-vacuum environments, clean rooms, specialized equipment for precisely positioning and probing. Other nano-characterization techniques include atom probe tomography [161, 162], electron holography [163], Kelvin probe force microscopy [164, 165], and scanning photocurrent microscopy [166]. However, all those techniques are laborious, and the characterization procedures are inefficient, costly, and hard to apply to large numbers of measurements.

The solution-based characterization methods are instead efficient and less costly. A very closely related characterization method is DEP based techniques. Motion responses under different DEP frequencies are used to separate [157, 167] and assemble nanowires into functional nanodevices [141, 158]. The DEP-based determination of nanowires electrical properties reported in [141, 158] provides a selection mechanism at high signal frequencies to isolate SiNWs with the highest conductivity and lowest defect density. The fabricated FET device using nanowires collected at high DEP signal frequency range above 10 MHz shows two orders of magnitude higher current, when it compares with the SiNW-base FETs that are collected at lower DEP signal frequencies. However, compared with probe-based measurements, those solution-based methods do not precisely quantify the direct relationship of physical properties of each

individual nanowire. To address this challenge, a contactless and solution-based EOS (CS-EOS) was proposed in [70] to measure the electrical conductivities of nanowires. The CS-EOS is based on nanowire transient alignment motion in AC electric fields of different frequencies. The CS-EOS approach in [70] focuses on characterizing each individual nanowire in fluid suspension using electric fields, which is compatible with the nanowires manipulation techniques proposed in this dissertation. Both methods are solution based and utilizing electric field as the main actuation source. By extending the CS-EOS for multiple nanowires and combining the techniques discussed in previous chapters, we can achieve the automated characterization, manipulation, and assembly of multiple nanowires into functional nanodevices with desired electrical properties.

### 6.2.1 Contactless and solution-based EOS (CS-EOS)

The CS-EOS is built upon the direct optical visualization of the frequency-dependent alignment rates of nanowires when they are suspended in a liquid of known properties and subjected to a spatially uniform AC electric fields of different frequencies [2]. According to Maxwell-Wagner interfacial polarization [168], large frequency dependency contributes to the dielectric response. The rotation alignment rates of nanowires under changing frequencies of AC electric fields vary for the 1D nanomaterials of different electrical properties. In particular, the *crossover frequency* indicates the transition of the alignment rate at low frequencies (fast alignment rate) to that at high frequencies (slow alignment rate), depending on the conductivities and permittivities of the particle and solvent, respectively. The crossover frequency  $\omega_c$  can be expressed as

$$\omega_c = \frac{\sigma_p L_{||} + \sigma_m (1 - L_{||})}{\varepsilon_p L_{||} + \varepsilon_m (1 - L_{||})}, \quad (6.1)$$

where  $\sigma_p$  and  $\sigma_m$  are the conductivities of the particle and medium, respectively. Parameters  $\varepsilon_p$  and  $\varepsilon_m$  are the permittivities of the particle and medium, respectively. Variable  $L_{||}$  in equation (6.1) is the geometric depolarization factor given by

$$L_{||} \approx \frac{\ln 2\beta - 1}{\beta^2}, \quad (6.2)$$

where  $\beta \equiv a/b$  is the aspect ratio of the prolate spheroidal shaped nanowire, and  $a$  and  $b$  are the semi-major and semi-minor axes of the prolate spheroid, respectively. For high aspect-ratio nanowire suspending in a low-conductivity solvent, the crossover frequency  $\omega_c$  simplifies to

$$\omega_c \cong \frac{\sigma_p}{\varepsilon_m(L_{||}^{-1} - 1)}. \quad (6.3)$$

By measuring the rotation alignment rates of the nanowires at different frequencies, crossover frequency  $\omega_c$  can be extracted. The geometric depolarization factor  $L_{||}$  is determined by estimating the dimension of the particle using acquired images. Therefore, using (6.3) the effective electrical conductivity of the nanowire  $\sigma_p$  is estimated with a known permittivity  $\varepsilon_m$  of the medium.

### 6.2.2 Simultaneous multiple-nanowire CS-EOS

When applying electric fields to the liquid suspension, a torque is exerted on the nanowire, under which the nanowire tends to align with the electric field. This effect, called electro-orientation, works for both DC and AC fields, and it is irrespective of the spatial uniformity of the electric field. The CS-EOS mentioned above is based on the electro-orientation principle. Although the electro-orientation does not rely on the spatial uniform electric field, the electric field exerted torques of the nanowires are however influenced by different electric fields, both in strengths and directions [168]. Under non-uniform electric field, nanowires at different locations may experience different electric fields. In planar motions, the exerted torque about the  $x$ -axis that is perpendicular to the plane (see Figure 2.3) can be expressed as

$$|\tau_x| = \pi ab^2 \varepsilon_m E_0^2 \sin(2\theta) \mathbf{Re}[\underline{\kappa}], \quad (6.4)$$

where

$$\underline{\kappa} = \frac{\underline{\varepsilon}_p - \underline{\varepsilon}_m}{3[\underline{\varepsilon}_m + (\underline{\varepsilon}_p - \underline{\varepsilon}_m)L_{||}]}, \quad (6.5)$$

$\underline{\varepsilon}_m$  and  $\underline{\varepsilon}_p$  are the complex permittivity of the fluid and the particle, respectively and  $\varepsilon_m$  is the real part of the fluid permittivity  $\underline{\varepsilon}_m$ .

From (6.4), it is clear that the rotation alignment rate depends on the electric field strength, and the orientation of the nanowire tends to align with the electric field direction. In addition, the induced dipole moment of the particle interacts with the non-uniform field to give rise to a frequency-dependent DEP force. The DEP force is proportional to the polarizability of the particle and the gradient of the field squared, namely,

$$\langle \mathbf{F}_{DEP} \rangle = 2\pi ab^2 \underline{\epsilon}_m \mathbf{Re}[\underline{\kappa}] \nabla E_{rms}^2. \quad (6.6)$$

The DEP force results in translation of the nanowires in the suspension. This motion leads to the inaccurate estimation of the crossover frequency. In order to enable the capability of characterizing multiple nanowires simultaneously using the CS-EOS principle, a pair of parallel electrodes are designed to generate uniformly distributed AC electric fields. Ideally, the uniformly distributed field only generates electro-orientation, i.e., no DEP-induced translation motion. The rotation alignment rate of each nanowire is not affected by the variations of electric fields. Therefore, the extracted conductivities of multiple nanowires by their alignment rates are comparable, which can be utilized as the separation criterion. Another reason for not using the electrical field generated by the electrode array design presented in the previous chapters is that, in real time, it is difficult to calculate the exact electric field at a given location to compensate for the inaccurate CS-EOS measurement due to the electric field-induced orientation and translation.

Therefore, we incorporate a pair of parallel electrodes as shown in Figure 6.1 to characterize nanowires. One pair of parallel electrodes is actuated by AC electric field of different frequencies to extract different alignment rates of each nanowire, while the other pair of parallel electrodes is used to re-orient the nanowires for repeated measurements under different frequencies. In the multiple-nanowire-characterization process, multiple image regions of interest are tracked simultaneously, and each image region of interest contains one nanowire. The dimension and orientation of each nanowire are

experimentally estimated in the time-lapse image series. Then, the maximum alignment rate at each measured frequency is recorded and plotted to observe the crossover frequency. In order to obtain the crossover frequency, we use the least squares method to fit the alignment rate at different frequencies as

$$\Omega^i = \frac{1}{1 + \left(\frac{\omega}{\omega_c^i}\right)^2}, \quad (6.7)$$

where  $\Omega^i$  is normalized alignment rate of the  $i$ th nanowire,  $\omega$  is the different frequencies of the applied electric field, and  $\omega_c^i$  is the fitted cross-over frequency for the  $i$ th nanowire. Finally, the conductivity of each nanowire can be calculated by plugging the crossover frequency into (6.3) and (6.2) with the known medium permittivity  $\varepsilon_m$  and the aspect ratio of the particle  $\beta$ , estimated from the online measurements of the nanowires' dimension.

### 6.3 Automated characterization, manipulation, and assembly of nanowires (ACMAN)

To demonstrate the concept and feasibility of the automated characterization, manipulation, and assembly of nanowires (ACMAN), we combine the multiple nanowires EOS in the previous section with the motion planning, control and manipulation approaches discussed in the previous chapters. Figure 6.1 illustrates the schematic of the complete ACMAN procedure to fabricate SiNW-based functional nanodevices. Three regions are defined in the intergraded design.

- Characterization region: a  $150\ \mu\text{m} \times 150\ \mu\text{m}$  square region in the center marked by the red dash line in Figure 6.1. The nanowires experience uniformly distributed electric field in the characterization region.
- Manipulation region: a 3D workspace among the centers of the outer electrode array. The magenta dash line shows an example in a  $2 \times 2$  electrode array in Figure 6.1.



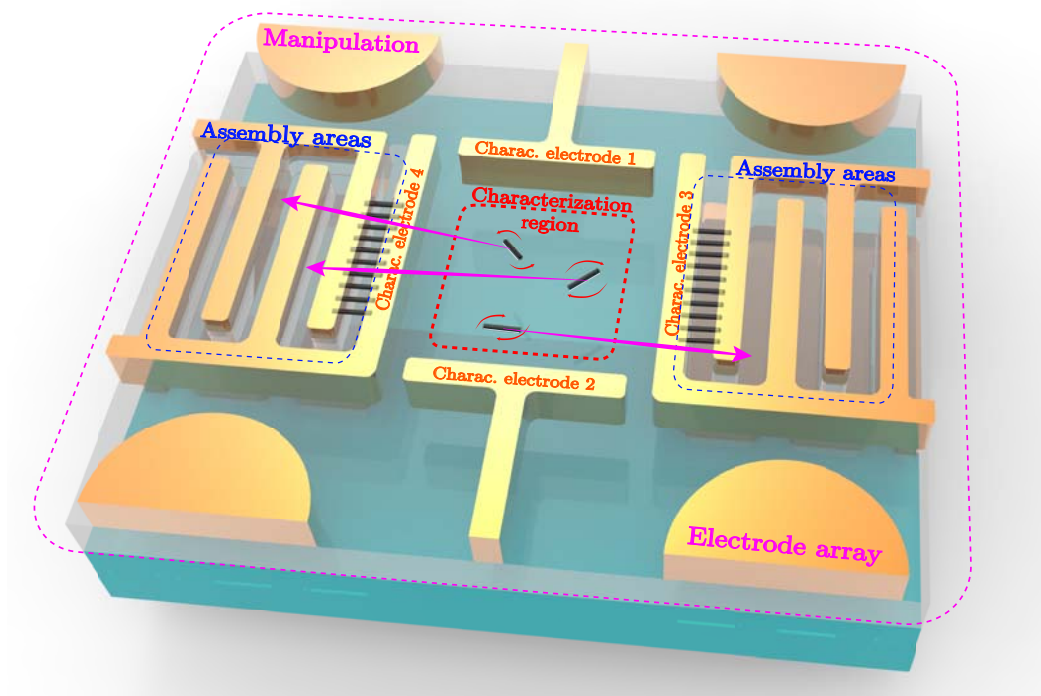


Figure 6.1: The schematic for automated characterization, manipulation, and assembly of SiNWs into FETs with different electric properties. First, nanowires are steered from their starting location to the characterization region (a  $150\ \mu\text{m} \times 150\ \mu\text{m}$  square region in the center marked by the red dash line). Simultaneous multiple-nanowire CS-EOS is used to measure the electrical conductivities of multiple nanowires in the characterization region. Meanwhile, the motion control, planning, and manipulation of nanowires strategies are used to keep the targeted nanowires inside the characterization region with uniform AC electric field. After characterization, those nanowires are separated according to their conductivities, driven to the assembly areas (blue dash line), and finally deposited between the source and drain electrodes to form FET nanodevices.

- Assembly areas: the regions to deposit separated nanowires according to their characteristic measurements. In Figure 6.1, the finger shaped dual electrodes are used as the source and drain electrodes in the FET application. The blue dash lines show the assembly areas for two different FETs.

With this design, we propose the intergraded ACMAN scheme to assemble nanodevices with different electrical conductivities. The intergraded process mainly includes the following four steps.

### 1. Initial manipulation

Nanowires of interest in the manipulation region are spotted and steered from their starting location to the characterization region using the proposed motion control, planning, and manipulation strategies. In this step, only circular electrode array are activated, and other electrodes are not powered on.

## 2. Characterization

Simultaneous multiple-nanowire CS-EOS is used to measure the electrical conductivities of multiple nanowires in the characterization region. To minimize the electric field influence on electro-orientation as discussed in Section 6.2.2, only characterization electrodes (charac. electrodes) shown in Figure (6.1) are activated. In this particular design, either charac. electrodes 1 or 3 is connected to the signal source (AC field), while the corresponding counter charac. electrodes 2 or 4 is switched to ground, respectively. To extract different alignment rates of each nanowire, AC fields with frequency ranging from 1000 Hz to 4 MHz are applied to charac. electrodes 3, while the charac. electrodes 4 is grounded, and all other electrodes are floating. After each alignment under one frequency, a 2000 Hz AC field with the same magnitude is applied to charac. electrodes 1, while the counter charac. electrodes 2 is grounded, and all other electrodes are floating. This 2000 Hz AC field is used to reorient the nanowires for repeated measurements at different frequencies. When the characterization is in process, only characterization electrodes are activated as mentioned above, and all other electrodes are floating. Due to the AC electroosmosis, Brownian motion, imperfect electrode boundary condition caused non-uniform field distribution and flow disturbance, the particles are experiencing unexpected motion and drifting in the characterisation process. Therefore, the motion control, planning, and manipulation of nanowires strategies discussed previously are used to keep the targeted nanowires inside the characterization region. After reposition the nanowires, the characterisation process resumes.

### 3. Separation manipulation

After online characterization, the nanowires are set to different target locations according to the separation criterion, namely, the threshold conductivity  $\sigma_{th}$ . Again, the motion control, planning, and manipulation of nanowires strategies are used to control the nanowire motion horizontally to separate and manipulate those nanowires with preferred conductivities towards different assembly areas. With this particular design, a separating direction is assigned to each nanowire according to their conductivities. Less conductive SiNWs ( $\sigma_p < \sigma_{th}$ ) are moved to the right pair of the assembly electrodes, while higher conductive SiNWs ( $\sigma_p \geq \sigma_{th}$ ) are steered towards the left pair of assembly electrodes.

### 4. Deposition

When the nanowires reach their desired deposit locations, an additional common top electrode, the ITO coverslip on top of the microfluidic channel as shown in Figure 2.1(a), is turned on, while all the other electrodes on the substrate are switched to ground to drive nanowires vertically to reach the device bottom surface. Finally, different AC fields are applied to charac. electrodes 3 and 4, respectively, according to the separation criterion and the counter finger-shaped electrodes are switched to ground. The generated DEP forces capture and attract the nanowires to align cross the finger channel gaps.

In each experiment, a droplet of nanowire suspension is applied to the microfluidic channel. Then the aforementioned steps 1 to 4 are repeated sequentially until the desired number of nanowires are deposited.

## 6.4 Automated assembly of SiNW-based FETs using ACMAN

With the intergraded ACMAN system presented in the previous section, we demonstrate the automated characterization, manipulation, and assembly of SiNWs to form

different FET devices with different electrical conductivities in this section. First, the micro-fabrication of the FET device is briefly discussed. Next, the performance and characteristics of the experimentally assembled nanodevices are measured and evaluated.

#### 6.4.1 Microfluidic device and SiNW FET fabrication

We use photolithography techniques to fabricate the microfluidic device that conducts the whole automated characterization, manipulation, and assembly process. The assembled nanowires with different conductivities on the microfluidic device eventually form the FETs with different characteristics. Figure 6.2 illustrates the fabrication schematic of the SiNW-based bottom-gate FET using photolithography process.

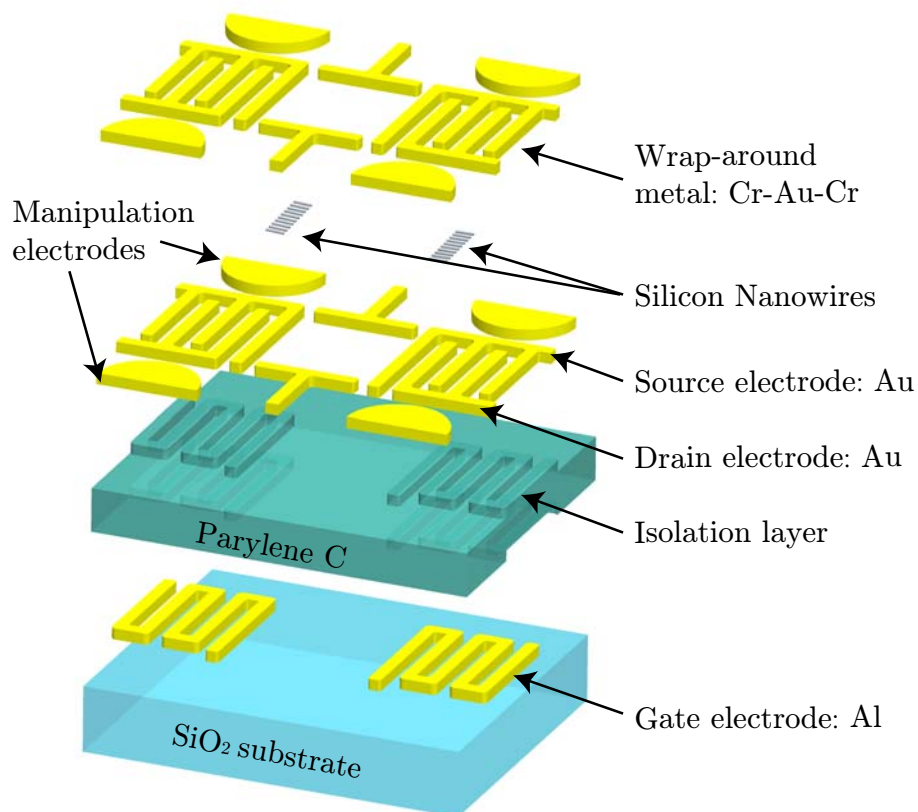


Figure 6.2: Fabrication schematic of the SiNW-based bottom-gate FET using photolithography process.

The FETs are designed to be fabricated on glass wafers ( $\text{SiO}_2$  substrate). A 300 nm-thick aluminum layer with 12  $\mu\text{m}$  width in channel gap is patterned as the bottom gate on the  $\text{SiO}_2$  substrate. Parylene C thin film is used to serve as the isolation layer between the gate and the body of the semiconductor. The thickness of parylene C film is designed as 600 nm. As discussed in Section 6.1, parylene films are biocompatible, biostable with high flexibility and excellent solution processability. The thickness is uniformly controllable, and the coating is conformal and completely pinhole-free at thicknesses greater than 500 nm. On the top of the substrate and dielectric layer, gold electrodes are patterned using photolithographic lift-off step. The gold-electrode structure is 300 nm in thickness including around 10 nm chromium adhesion layer. The gold structure contains finger shaped source/drain metal contact pads and  $2 \times 2$  manipulation electrode array with the center to center displacement  $L = 900 \mu\text{m}$ . The finger shaped gold electrodes in assembly areas are 30  $\mu\text{m}$  in width with 15  $\mu\text{m}$  channel gap. Due to the conformal coating of parylene films, the channel gap is filled with parylene as the same height as the source and drain electrodes. Therefore, the air gap between the SiNWs and the dielectric layer is minimized to enhance the high performance of the FET.

To form the microfluidic device, a 12  $\mu\text{m}$ -thick adhesive spacer (Nitto Dekko Corp) and an ITO top coverslip are placed on the electrodes to form the fluid reservoir. The SiNWs used in the experiments are fabricated using metal-assisted chemical etching from lightly doped/intrinsic ( $3000 - 5000 \Omega\cdot\text{cm}$  in average resistivity or  $3.3 - 2 \times 10^{-2} \Omega^{-1}\text{m}^{-1}$  in bulk conductivity) and heavily doped ( $3 - 5 \Omega\cdot\text{cm}$  in average resistivity or  $20 - 33 \Omega^{-1}\text{m}^{-1}$  in bulk conductivity) n-type silicon wafers. Figure 3.4(b) shows the SEM image of as-grown SiNWs. The produced SiNWs were treated with dry oxygen passivation (950 °C) for 15 min and then vacuum annealed at 350 °C for several hours prior to experiments. Before each experiment, the SiNWs are detached from the aforementioned two types of wafers and suspended in mineral oil to form a mixture of SiNW suspension with a large variation of conductivities. Mineral oil (Drakeol 7 LT Mineral

Oil, Calumet Specialty Products and Partners, L.P.;  $\epsilon_m = 2.0 \times 10^{-11}$  F/m, and viscosity  $\mu_m = 25.9$  cP) are used to suspend the SiNWs because of its low conductivity. Also, the use of mineral oil yields a thick electrical double layer around the particles, which minimizes induced-charge EO (i.e., electro-osmotic) flow at the particle-fluid interface [2]. Then the integrated automated characterization, manipulation, and assembly of nanowires are performed as discussed in Section 6.3. Up to  $\pm 50$  V DC voltages are applied to electrodes array and  $50 \text{ V}_{\text{peak-to-peak}}$  AC fields with various frequencies from 1000 Hz to 4 MHz are used in CS-EOS characterization. SiNWs are separated by threshold conductivity  $\sigma_{th} = 0.2$  S/m to either side of the assembly areas and finally deposited as a thin film of SiNWs to bridge the source and drain electrodes. The selection of threshold value  $\sigma_{th} = 0.2$  S/m are based on the effective measurement range of CS-EOS using mineral-oil-SiNW suspension (from  $10^{-5}$  to 10 S/m) and the measured conductivity distribution over 100 as-produced and passivated SiNWs (ranging from  $10^{-3}$  to 10 S/m with average about 0.2 S/m) [2]. In the final deposition process, two  $50 \text{ V}_{\text{peak-to-peak}}$  AC fields with  $\omega_L = 20$  kHz (attracting SiNWs with conductivities above  $\sigma_L = 0.001$  S/m) and  $\omega_H = 2$  MHz (attracting SiNWs with conductivities higher than  $\sigma_H = 0.15$  S/m) are utilized to trap the nanowires in the less conductive and conductive assembly areas, respectively. Figure 6.3 shows the overlaid nanowire trajectories for simultaneously automated characterization, manipulation, and assembly of two SiNWs by their electrical conductivities. The less conductive ( $\sigma_{LC} = 0.045$  S/m) SiNW is placed between the right pair of contact electrodes, while the higher conductive SiNW ( $\sigma_{HC} \geq 0.46$  S/m) is placed between the left pair of contact electrodes. The star and ellipse marks represent the starting and target locations of each nanowire. The corresponding alignment rates measurement and crossover frequencies extraction are shown in Figure 6.4.

After assembly, the top coverslip and adhesive channel are removed with care. The device is then soaked in hexane for 10 minutes to remove excess of mineral oil, next the substrate is gently rinsed with hexane to remove oil residues, followed by rinsed with

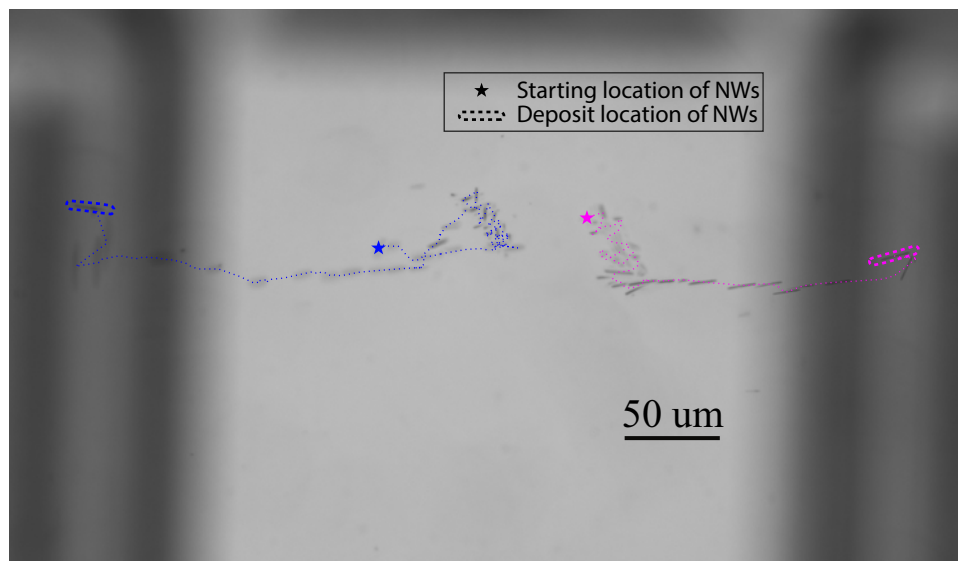


Figure 6.3: Overlaid nanowire trajectories for simultaneously automated characterization, manipulation, and assembly of two SiNWs by their electrical conductivities. The less conductive SiNW ( $\sigma_{LC} = 0.045$  S/m) is placed between the right pair of contact electrodes, while the higher conductive SiNW ( $\sigma_{HC} \geq 0.46$  S/m) is placed between the left pair of contact electrodes. The star and ellipse marks represent the starting and target locations of each nanowire. The figure shows overlaid center-of-mass trajectories of the two simultaneous nanowires.

isopropyl alcohol (IPA) and gently dried under  $N_2$  flow for the clean purpose. All those solvent removal and evaporation processes are handled with great care, not disturbing the nanowires trapped in the device channel.

Finally, a second 350 nm-thick Cr-Au-Cr (100 nm chromium, followed by 150 nm gold, and then 100 nm chromium) layer is sputtered on the top of patterned nanowires with the same pattern as the first gold layer. The top “wrap-around” Cr-Au-Cr layer increases the nanowire-metal contact area and enhances charge carrier injection. Prior to the wrap-around metal deposition, the edges of the SiNWs at the source and drain contact regions are etched in a buffered hydrofluoric acid (BOE) for 3 seconds to remove the native oxide layer of the nanowires, forming clean contact regions of the SiNWs and contact metal. The choice of the contact metals is dictated by both p-type and n type semiconductors since p-type is usually observed in undoped SiNWs while n-type is observed in phosphorus doped semiconducting materials. Gold metal work

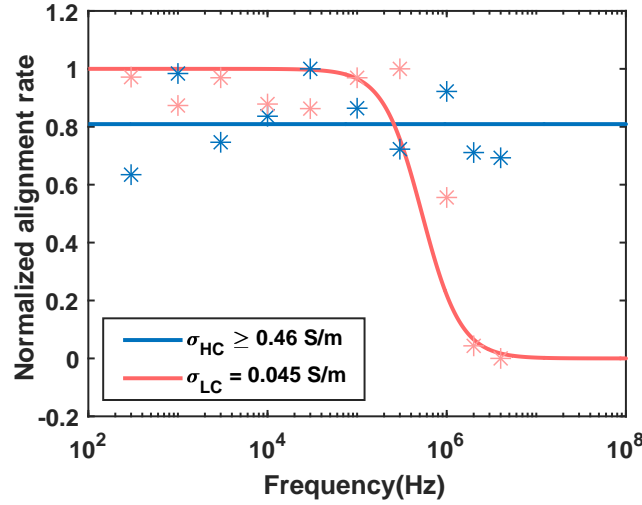


Figure 6.4: Measured alignment rates of two simultaneous SiNWs in Figure 6.3 with respect to applied electric field frequency. The solid lines are curve fit of the form  $\Omega = 1/[1 + (\omega/\omega_c)^2]$ , from which the crossover frequency and hence the nanowire conductivity can be extracted.

functions are closely matched to the valence band edge of silicon to enable near-Ohmic contact for p-type transport, while chromium and aluminum metal reduce the Schottky barrier for n-type transport [169].

In addition, the above-mentioned procedures yield transparent devices with low-temperature fabrication processes. By replacing the SiO<sub>2</sub> substrate with the biocompatible materials such as parylene C, the fabricated micro-fluidic devices can be directly applied in biomedical applications.

The schematic of a bottom-gate SiNW FET is illustrated in Figure 6.1, showing the bottom gate and the top contact wrapping around nanowires. Figure 6.5 shows the overlaid motion trajectories of 14 nanowires and their deposit locations in the experiment using the automated characterization, manipulation of multiple SiNWs, and deposit them between the source and drain electrodes as thin films. Less conductive SiNWs ( $\sigma_p < 0.2$  S/m) are placed between the right pair of contact electrodes, while higher conductive SiNWs ( $\sigma_p \geq 0.2$  S/m) are placed between the left pair of contact electrodes. The star and ellipse marks represent the starting and target locations of each nanowire. Due to the manipulation electrode array has  $2 \times 2$  circular electrodes in



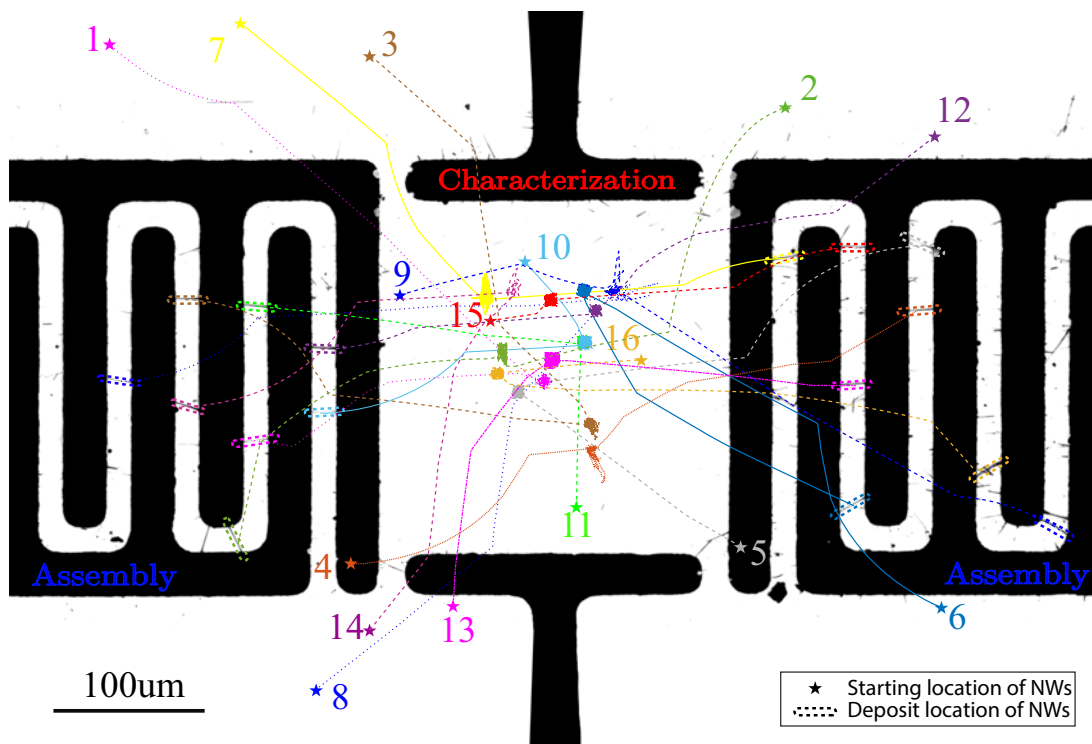


Figure 6.5: Overlaid nanowire motion trajectories in the automated characterization, manipulation, and assembly of SiNWs as thin-film FETs. Less conductive SiNWs ( $\sigma_p < 0.2$  S/m) are placed between the right pair of contact electrodes, while higher conductive SiNWs ( $\sigma_p \geq 0.2$  S/m) are placed between the left pair of contact electrodes. The star and ellipse marks represent the starting and target locations of each nanowire. The figure shows overlaid trajectories of the center of mass of 14 nanowires and their deposit locations.

the current design, the maximum number of nanowires that can be independently and simultaneously controlled in one atomic cell is two according to Section 4.1. In the experiment, one or two nanowires were characterized, steered, and assembled simultaneously in each round.

#### 6.4.2 Characteristics and performance of assembled SiNW FETs

The effectiveness of the proposed ACMAN design for separation of SiNWs according to their electric conductivities is evaluated by the characteristics and performance of assembled SiNW FETs. Followed by the fabrication process in Section 6.4.1, four assembled devices are evaluated and each device contains two SiNW FETs, where one

side is assembled using less conductive SiNWs with  $\sigma_p < \sigma_{th}$  while the other side is assembled using conductive SiNWs with  $\sigma_p \geq \sigma_{th}$ , where  $\sigma_{th} = 0.2$  S/m.

The current-voltage characteristics of the assembled SiNW transistors are measured using an HP 4140B Picoammeter semiconductor analyzer system. The transfer characteristics of Devices Charact. 1 to 4 are shown in Figures 6.6 - 6.9, respectively.

Device Charact. 1 contains total 24 SiNWs using the intergraded ACMAN process, where 12 nanowires (NWs) were characterized, selected and deposited on each side according to their conductivities. However, the resulting FETs remained 10 NWs on each side after the wrap-around electrode fabrication by the metal lift-off process. Both FETs of device Charact. 1 show N-type characteristics. The FET constructed by conductive NWs shows two orders of magnitude higher current in the device on-state than the FET with less conductive NWs as shown in Figure 6.6(a). Figure 6.6(b) plots the measured conductivity distribution of the separated and deposited 24 SiNWs using simultaneous multiple-nanowire CS-EOS. The red dash-line represents the separation threshold  $\sigma_{th} = 0.2$  S/m. In the experiment, one or two NWs were characterized, separated, and deposited at one time due to the electrode array dimension. Figures 6.6(c) and 6.6(d) illustrate the output characteristics of the FETs in less conductive and conductive sides, respectively. The output characteristics show an almost two-order difference between the two FETs. This result is consistent with the transfer characteristic and the conductivity distribution measurements.

Similarly, Device Charact. 3 deposited total 20 SiNWs, where 10 NWs were selected and deposited on each side according to their conductivities. After the wrap-around electrode fabrication, 3 NWs on each side were kept in the channel gap. The FET constructed by conductive NWs shows N-type characteristics, while less conductive NWs formed FET demonstrates P-type characteristics. The resulting on-current in the device on-state is more than two orders of magnitude higher than the less conductive NWs constructed FET as shown in Figure 6.8(a). Figure 6.8(b) shows the

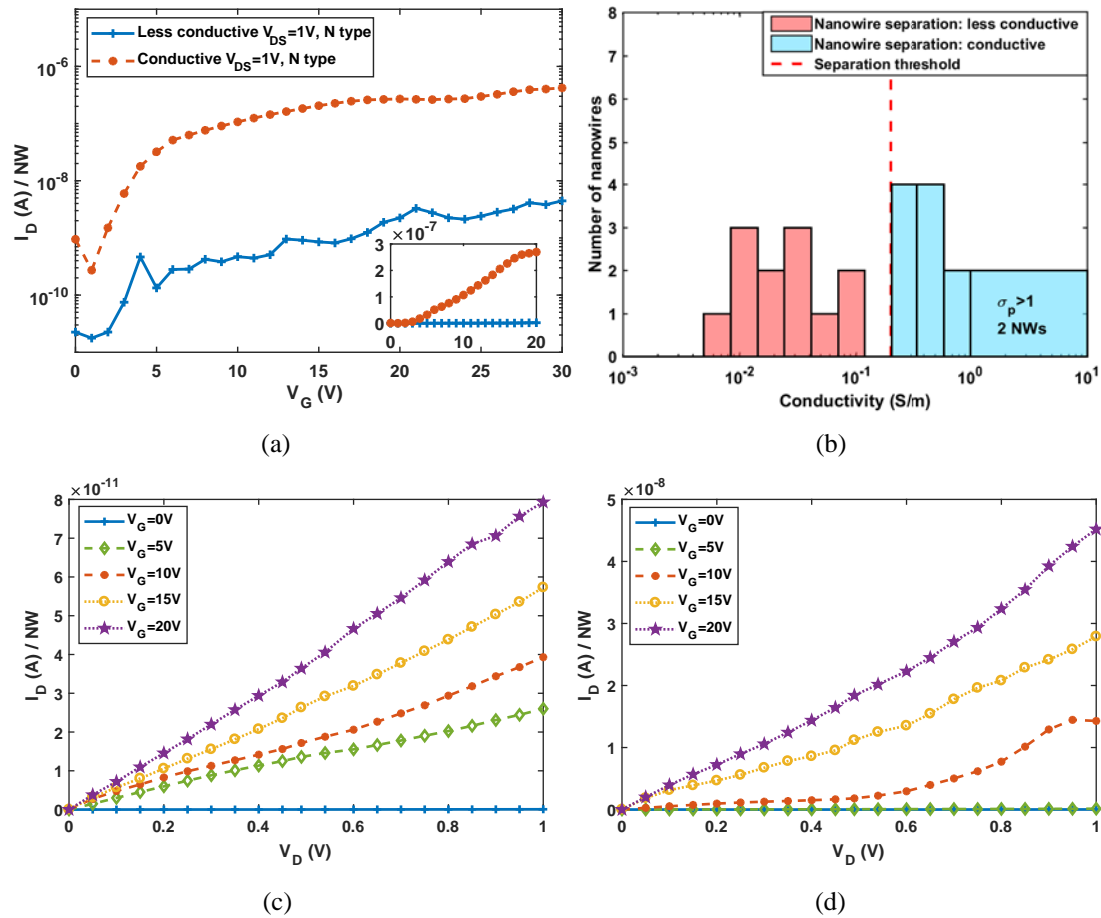


Figure 6.6: Device Charact. 1: A proof-of-concept demonstration of the integrated automated characterization, manipulation, and assembly of 24 SiNWs as FET devices. 12 nanowires (NWs) were characterized and deposited on each side. After the wrap-around electrode fabrication, the resulting FETs have 10 NWs on each side, showing N-type characteristics. (a) Transfer characteristics in logarithmic scale showing the drain current per nanowire at source-to-drain voltage  $V_{DS} = 1$  V for the two N type FETs after separation. (inset) The transfer characteristics in linear scale. (b) Measured conductivity distribution against the number of characterized nanowires by CS-EOS. (c) Output characteristics of the FETs showing the drain current per nanowire in less conductive side at gate voltage  $V_G = 0$  to 20 V in 5 V steps. (d) Output characteristics of the FETs showing the drain current per nanowire in conductive side at  $V_G = 0$  to 20 V in 5 V steps.

measured conductivity distribution of the separated and deposited 20 SiNWs using simultaneous multiple-nanowire CS-EOS. Figures 6.8(c) and 6.8(d) illustrate the output characteristics of the FETs in less conductive and conductive side, respectively. As shown in Figures 6.7 and 6.9, Devices Charact. 2 and Charact. 4's characteristics also

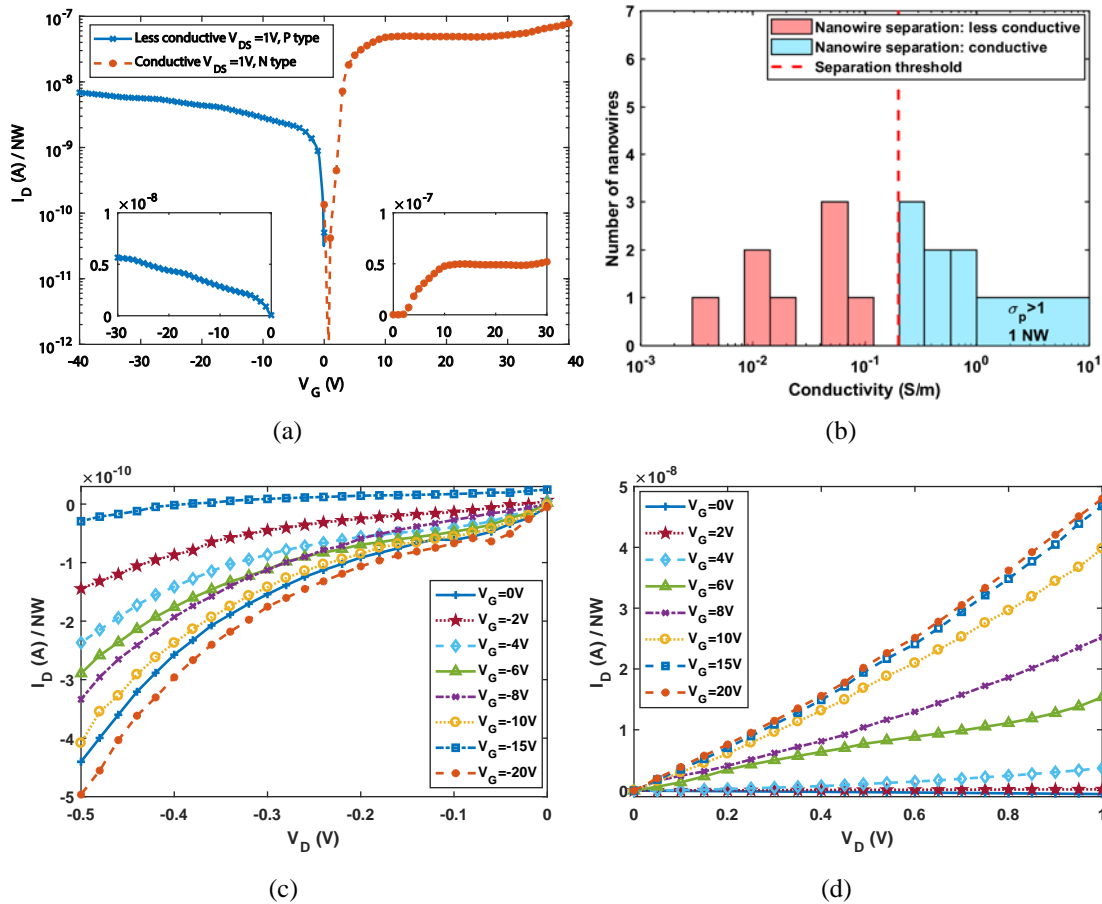


Figure 6.7: Device Charact. 2: A proof-of-concept demonstration of the integrated automated characterization, manipulation, and assembly of 16 SiNWs as FET devices. 8 NWs were characterized and deposited on each side. After the wrap-around electrode fabrication, the resulting FETs have 3 NWs on each side. The FET assembled with less conductive SiNWs shows P-type characteristics while the FET assembled with conductive SiNWs shows N-type characteristics. (a) Transfer characteristics in logarithmic scale showing the drain current per nanowire at  $V_{DS} = 1$  V for the P type and N type FETs after separation. (inset) The transfer characteristics in linear scale. (b) Measured conductivity distribution against the number of characterized nanowires by CS-EOS. (c) Output characteristics of the FETs showing the drain current per nanowire in less conductive side at  $V_G = 0$  to  $-20$  V. (d) Output characteristics of the FETs showing the drain current per nanowire in conductive side at  $V_G = 0$  to  $20$  V.

confirm the effectiveness of the intergraded ACMAN scheme and yield conductive SiNW-based FETs with at least one order of magnitude higher on-current as compared to the less conductive SiNW-based FETs. The corresponding output characteristics and the conductivity distribution measurements substantiate similar conclusion.

Figure 6.10 illustrates the characteristic of the FET device fabricated using the DEP assembly scheme proposed in [139, 141]. SiNWs were collected at different DEP frequencies. 2 MHz and 20 kHz frequencies and 50 V<sub>peak-to-peak</sub> AC fields are used to fabricate the conductive and less conductive FETs, respectively, which are the same fields as used in the deposition step to trap nanowires for Device Charact. 1 to 4 in the ACMAN scheme.. After the wrapping electrode fabrication, the resulting DEP only FETs have 3 NWs on each side, both showing P-type characteristics.

The on-current ( $I_{on}$ ) comparisons of the different FETs among those four ACMAN-based devices and the DEP only device are presented in Figure 6.12. From the on-current ratio of the higher conductive (HC) to less conductive (LC) SiNW-FETs, the separated HC SiNW FETs show at least one order of magnitude higher on-current, and up to more than three orders of magnitude higher on-current. Whereas, the DEP only device demonstrates 3.8 higher current magnitude of HC FET to the LC FET.

To further quantitatively evaluate the performance of FETs, the sub-threshold swing (s-s), NW trap density ( $N_{trap}$ ), and device mobility are calculated for both less conductive and conductive FETs in each device. Figure 6.11 presents the graphical estimation of the sub-threshold swing (s-s), on/off current ( $I_{ON/OFF}$ ) and transconductance  $g_m$  using the less conductive FET measurement data of Device Charact. 3 as shown in Figure 6.8(a). The s-s (V/dec) describes the amount of gate voltage required to increase drain current by one order of magnitude in the sub-threshold region. The transfer characteristics of the SiNW FETs in logarithmic scale shown in Figures 6.6 (a) - 6.9 (a) and 6.10 are used for the extraction of s-s using equation (6.8) for the assembled ACMAN based and DEP-only based devices, respectively. The smaller s-s, the quicker or sharper increasing of drain current. This sub-threshold behavior also indicates the difference in defect/trap states in the NWs or at the NW/dielectric interface. A higher density of traps results in a less steep current increase, as more trap states need to be filled. In other words,  $N_{trap}$  expresses the level of defects. Equation (6.9) shows the

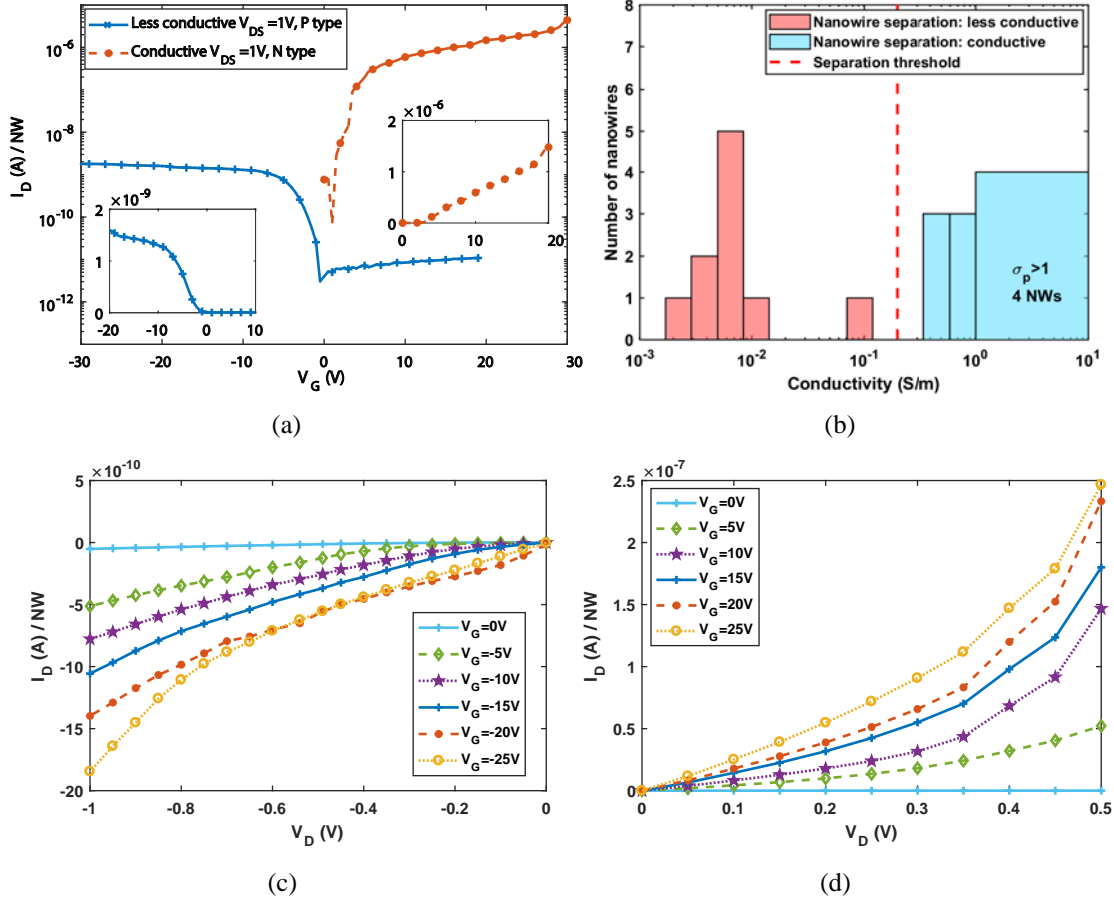


Figure 6.8: Device Charact. 3: A proof-of-concept demonstration of the integrated automated characterization, manipulation, and assembly of 20 SiNWs as FET devices. 10 NWs were characterized and deposited on each side. After the wrap-around electrode fabrication, the resulting FETs have 3 NWs on each side. The FET assembled with less conductive SiNWs shows P-type characteristics while the FET assembled with conductive SiNWs shows N-type characteristics. (a) Transfer characteristics in logarithmic scale showing the drain current per nanowire at  $V_{DS} = 1$  V for the P type and N type FETs after separation. (inset) The transfer characteristics in linear scale. (b) Measured conductivity distribution against the number of characterized nanowires by CS-EOS. (c) Output characteristics of the FETs showing the drain current per nanowire in less conductive side at  $V_G = 0$  to  $-25$  V in  $-5$  V steps. (d) Output characteristics of the FETs showing the drain current per nanowire in conductive side at  $V_G = 0$  to  $25$  V in  $5$  V steps.

relationship between the  $N_{\text{trap}}$  and s-s.

$$s - s = \frac{\Delta V_G}{\Delta \log I_{DS}}, \quad (6.8)$$

$$N_{\text{trap}} = \left[ \frac{q(s - s) \log(e)}{kT} - 1 \right] \frac{C_{\text{NW}}}{2\pi n r L_d q}, \quad (6.9)$$

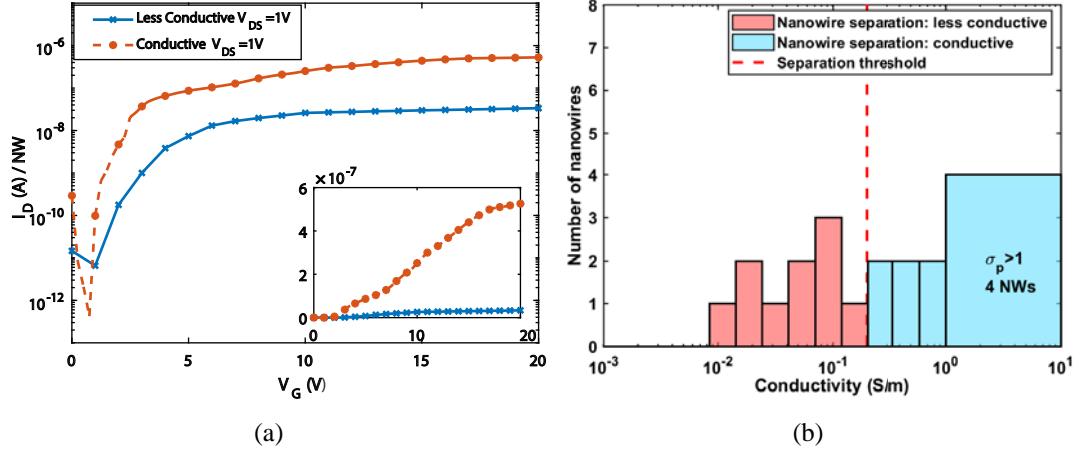


Figure 6.9: Device Charact. 4: A proof-of-concept demonstration of the integrated automated characterization, manipulation, and assembly of 20 SiNWs as FET devices. 10 NWs were characterized and deposited on each side. After the wrap-around electrode fabrication, 9 NWs remain on the less-conductive-side FET, and the conductive-side FET has 7 NWs left, both showing N-type characteristics. (a) Transfer characteristics in logarithmic scale showing the drain current per nanowire at  $V_{DS} = 1$  V for the two N type FETs after separation. (inset) The transfer characteristics in linear scale. (b) Measured conductivity distribution against the number of characterized nanowires by CS-EOS.

where  $q$  is the elementary charge,  $k$  is the Boltzmanns constant,  $T$  is absolute temperature,  $n$  is the total number of NWs across the channel gap,  $r$  is the NW radius (vary from 25 - 150 nm [2]),  $L_d$  is the channel gap width (15  $\mu$ m), and  $C_{NW}$  is the total gate capacitance. Figure 6.13 shows the s-s and  $N_{trap}$  data extracted from transfer characteristics plots. The FETs constructed by conductive SiNWs separated by ACMAN scheme demonstrate consistent smaller value in s-s and trap densities.

The carrier mobility is another performance metric to describe how quickly the carrier can move through a semiconductor. For NW-based FETs, the cylinder-on-plate model [170] is used to calculate the mobility ( $\mu$ ) from the linear regime transfer characteristic. This model considers the finite number of NWs in the channel, as well as the electrostatic fringing effect of the gate field acting on the aligned NWs. The mobility and gate capacitance are calculated respectively as

$$\mu = \frac{L_d^2 g_m}{C_{NW} V_{SD}}, \quad (6.10)$$

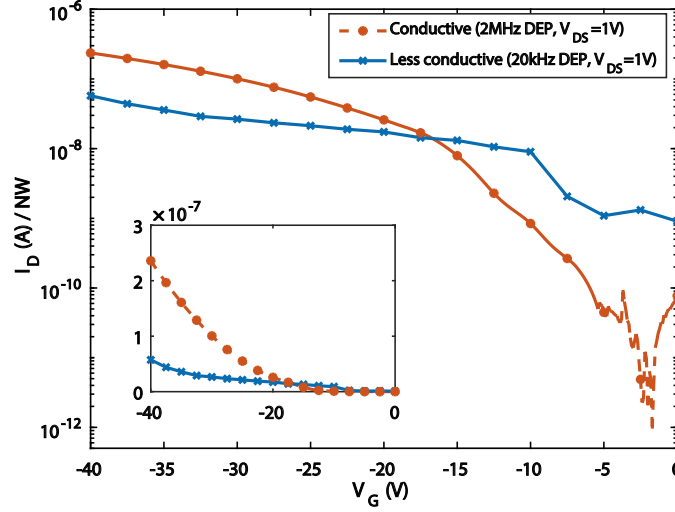


Figure 6.10: Device DEP only: SiNWs were collected at different DEP frequencies. 2 MHz and 20 kHz frequencies and 50 V<sub>peak-to-peak</sub> AC fields are used to fabricate the conductive and less conductive FETs, respectively, which are the same fields as used in the deposition step to trap nanowires for Device Charact. 1 to 4 in the ACMAN scheme. After the wrapping electrode fabrication, the resulting DEP only FETs have 3 NWs on each side, both showing P-type characteristics.

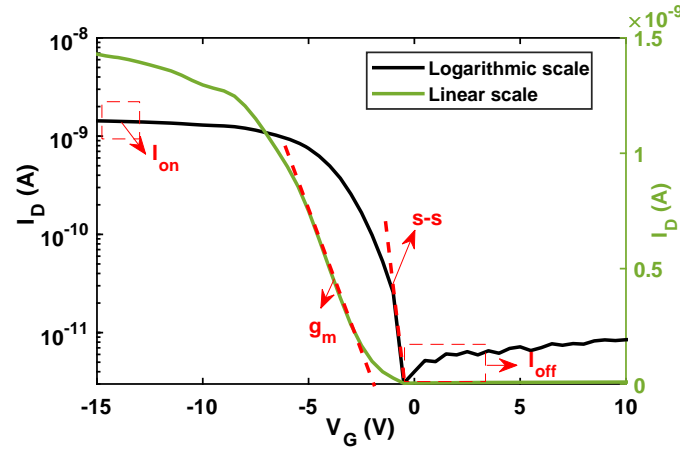


Figure 6.11: Graphical presentation of the sub-threshold swing (s-s), on/off current ( $I_{ON/OFF}$ ) and transconductance  $g_m$  using the less conductive FET measurement data of Device Charact. 3 as shown in Figure 6.8(a).

$$C_{NW} = \frac{2\pi\epsilon_0\epsilon_{\text{par}}L_d n}{\cosh^{-1}\left(\frac{r+d}{r}\right)}, \quad (6.11)$$

where  $n$  is the total number of NWs across the channel gap,  $r$  is the NW radius (vary from 25 - 150 nm [2]),  $L_d$  is the channel gap width (15  $\mu\text{m}$ ),  $\epsilon_0$  is the absolute permittivity,  $\epsilon_{\text{par}}$  is the dielectric constant of parylene C (3.15) and  $d$  is the thickness of the



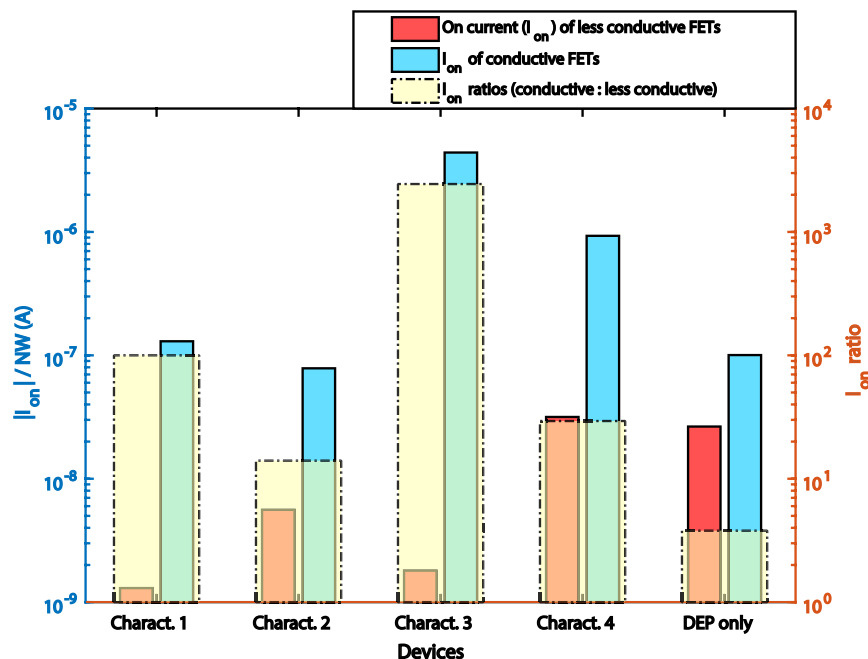


Figure 6.12: The on-current (the absolute value  $|I_{on}|$ ) comparison of the FET Devices Charact. 1 to 4. and the DEP only assembled devices.

gate dielectric layer (600 nm). The transconductance  $g_m = \frac{\partial I_{DS}}{\partial V_G}$  is found by using the transfer characteristics of the SiNW FETs in linear scale shown in Figure 6.6 (a) - 6.9 (a) and 6.10. A graphical presentation of  $g_m$  can be found in Figure 6.11.

Figure 6.14 compares the carrier mobility of the FETs on each device. The error bar represents the uncertainties in nanowire diameters and variations of the dielectric layer thickness. It is clear that the mobility of the FET with the higher conductivity NWs is greater than the FET with less conductive NWs on each ACMAN based device. The DEP only method fails to assemble higher mobility device with the higher DEP frequency, which is contradictory to the argument in [141]. In [141], DEP aligned nanowires in the high frequency range demonstrate higher mobility values, as compared to the lower frequency range.

Table 6.1 summarizes the performance comparison of the FETs fabricated using ACMAN scheme (Device Charac.1 to 4) and DEP only method. In the table, HC stands for the FETs that are assembled by the selected higher conductive nanowires (HC FETs), and LC represents the FETs that are fabricated using the separated less

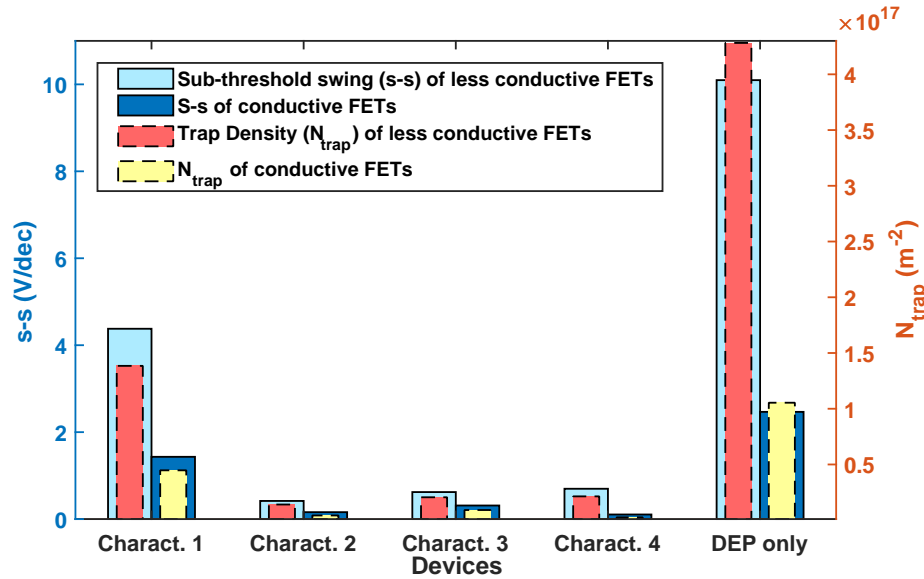


Figure 6.13: The sub-threshold swing (s-s) and traps density ( $N_{\text{trap}}$ ) for Device Charact. 1 to 4 and the DEP only assembled devices. The transfer characteristics of the SiNW FETs shown in Figures 6.6 (a) to 6.9 (a) and 6.10 are used for the extraction of s-s of the assembled devices, respectively.

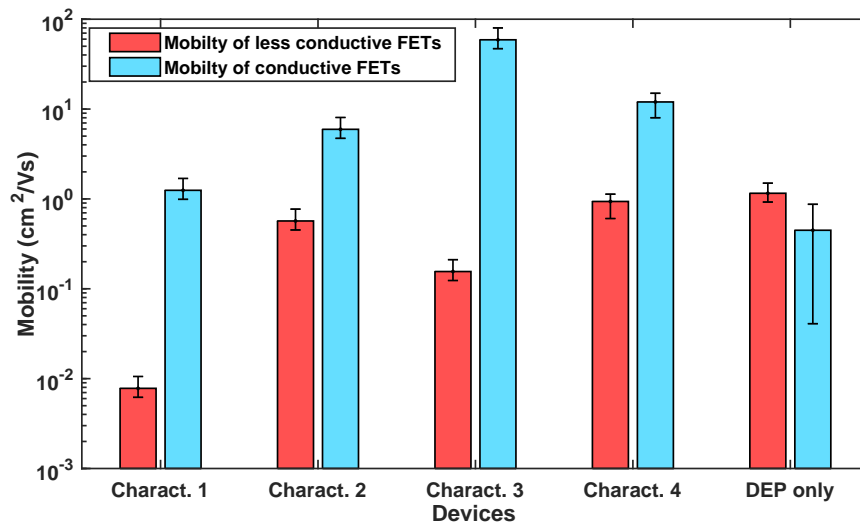


Figure 6.14: Mobility comparison for Device Charact. 1 to 4 and the DEP only assembled devices.

conductive nanowires (LC FETs).  $R_{\text{H/L}}$  denotes the ratio of the HC FET characteristics to LC FET characteristics. According to the performance measurements, the FET devices based on the integrated ACMAN scheme have demonstrated excellent performance and characteristics, yielding high on-current (ranging from 0.1 to 4.4  $\mu\text{A}$  per

Table 6.1: Performance comparisons for the FETs fabricated using the ACMAN process and DEP only method.

		$I_{on}/NW(A)$	s-s(V/dec)	$N_{trap}(m^{-2})$	$\mu (cm^2/Vs)$	NW No.	Type
Device Charac. 1	HC	$1.3 \times 10^{-7}$	1.43	$2.8 \times 10^{16}$	$9.9 \pm 2.2 \times 10^{-1}$	10	N
	LC	$1.3 \times 10^{-9}$	4.38	$8.7 \times 10^{16}$	$6.2 \pm 1.4 \times 10^{-3}$	10	N
	$R_{H/L}$	100	33%	0.32	$\sim 160$	same	same
Device Charac. 2	HC	$7.9 \times 10^{-8}$	0.16	$2.7 \times 10^{15}$	$4.7 \pm 1.1$	3	N
	LC	$5.6 \times 10^{-9}$	-0.42	$-8.9 \times 10^{15}$	$-4.5 \pm 1.0 \times 10^{-1}$	3	P
Device Charac. 3	HC	$4.4 \times 10^{-6}$	0.31	$5.8 \times 10^{15}$	$4.7 \pm 1.1 \times 10$	3	N
	LC	$1.8 \times 10^{-9}$	-0.62	$-1.3 \times 10^{16}$	$-1.2 \pm 0.3 \times 10^{-1}$	3	P
Device Charac. 4	HC	$9.3 \times 10^{-7}$	0.11	$1.6 \times 10^{15}$	$9.0 \pm 2.0$	7	N
	LC	$3.2 \times 10^{-8}$	0.70	$1.3 \times 10^{16}$	$7.5 \pm 1.7 \times 10^{-1}$	9	N
	$R_{H/L}$	29	16%	0.12	$\sim 12$	less	same
DEP only	HC	$1.0 \times 10^{-7}$	-2.47	$-5.0 \times 10^{16}$	$-3.2 \pm 0.7 \times 10^{-1}$	2	P
	LC	$2.6 \times 10^{-8}$	-10.10	$-2.0 \times 10^{17}$	$-8.1 \pm 1.9 \times 10^{-1}$	3	P
	$R_{H/L}$	3.8	24%	0.25	$\sim 0.4$	less	same

nanowire), small sub-threshold swing (less than 1 V/dec) and high device mobility (greater than 1  $cm^2/Vs$ ) for separated conductive SiNWs built FETs. The ratios  $R_{H/L}$  demonstrate the significantly improved performance of the separated higher conductive SiNW FETs to the less conductive FETs by ACMAN scheme, with two orders of magnitude higher on-current per nanowire, 16% to 33% lower sub-threshold swing, and up to 160 times higher mobility values. Therefore, the ACMAN strategy can discriminate, separate nanowires, and assemble nanowires based FETs with different characteristics.

The overall performance of the ACMAN fabricated FETs is consistent with the devices data in [139, 141], where SiNW are collected at various DEP frequencies and further assembled into FETs. In [141], DEP aligned NWs in the high frequency range (10 MHz and 20 MHz) are considered as high quality, as compared to the lower frequency range (30 Hz, 300 kHz). The characteristics of the ACMAN fabricated less

conductive FETs are consistent with the measurement results using lower frequencies induced DEP in [141]. Meanwhile, the ACMAN based conductive FETs show superior on-current per nanowire and sub-threshold swing than the high frequencies collected FETs in [141]. The conductive FETs in this work show at least  $0.1 \mu\text{A}$  order on-current and less than  $1.5 \text{ V/dec}$  sub-threshold swing, and the high quality FETs in [141] demonstrate at most  $0.1 \mu\text{A}$  order on-current and greater than  $2.1 \text{ V/dec}$  sub-threshold swing. The average trap densities and mobilities of FETs using the integrated ACMAN scheme do not show superior performances than those in [139, 141] due to the fact that using metal-assisted chemical etching fabricated SiNWs have more defects and impurities than the CVD-grown SiNWs used in [139, 141].

## 6.5 Summary

In this chapter, we presented the integrated ACMAN process of automated characterizing, manipulating, and assembling of nanowires into functional nanodevices. Firstly, we extended the CS-EOS to characterize the simultaneous multiple nanowires. Secondly, the integrated process incorporated the proposed strategies of motion control, planning, and manipulation of nanowires in the characterization and separation of nanowires with preferred conductivities, and further, deposited them at different locations to form functional nanodevice with different electrical properties. Proof-of-concept SiNW-based FET devices were fabricated and assembled by separating various SiNWs according to their electrical conductivities. Finally, the characteristics measurements of separated higher conductive SiNW-based FETs show superior performance comparing with the less conductive counterpart, which confirmed the separation and assembly performance of the proposed integrated ACMAN scheme.

## Chapter 7

### Conclusions and Future Work

#### 7.1 Conclusions

In this dissertation, we presented a novel scheme for motion control, planning, and manipulation of nanowires under electric-fields in fluid suspension. We thoroughly investigated and analyzed different aspects of EP-based nanowire manipulation, which is based on nanowires dynamic model in dilute suspension with the micro-fluidic device containing a set of controllable electrodes. The micro-fluidic device allows effectively controlling individual nanowires sequentially and multiple nanowires simultaneously while compensating the flow disturbances. We proposed difference planning strategies, such as sampling based (RRT\* variations), graph based (A\* variations), network flow based (MCMF), and heuristic based motion planning algorithms to generate collision-free motion trajectories for efficient and effective nanowire manipulation. The comparisons among the proposed algorithms and the existing algorithms showed that the proposed algorithms reduced the computational complexity significantly and effectively obtained the shortest distance, or near-time-optimal trajectories.

The EP-based motion control and planning scheme of individual nanowires took advantages of the symmetry properties of the electric field generated by the electrode arrays. A superposition approach was developed to efficiently compute the electric-field distribution for any given set of powered-“on” electrodes. The EP driving force on the particles was modeled and the vision-based feedback control compensated for unmodeled particle dynamics. The path-following control design guaranteed the nanowire motion performance to track a given trajectory. The attractive property of the motion

control design lied in online velocity tuning for high path-following performance and proven converging tracking errors. The feedback control also compensated for the motion disturbances due to the un-modeled EO-induced flow motion.

Given the fact that the nanowire motion-planning problem is NP hard, we proposed two heuristic algorithms based on the reduced search areas. We compared the heuristic algorithms with the other existing motion planning algorithms such as RRT and  $A^*$ . The results showed that the heuristic algorithms significantly reduced the computational complexity while maintained comparable performance with those of the RRT,  $A^*$ , and other algorithms. Extensive experimental results confirmed the analysis and the design of the nanowire motion control, planning, and manipulation. Using an additional common top electrode, a nanowire manipulation scheme was also presented to steer the individual nanowires horizontally to the desired positions, and vertically deposit them onto the device bottom surface to form a certain geometric pattern sequentially. We presented extensive experimental results to validate and demonstrate the performances of proposed control and planning algorithms.

In order to achieve simultaneous multiple-nanowire motion control, planning, and manipulation, we first proposed a motion-control algorithm to independently control multiple nano-wires to follow desired trajectories. The motion-control algorithm was designed to simultaneously steer multiple nanowires under controlled EP forces with the exponentially decaying tracking errors. A two-stage motion-planning algorithm was proposed and demonstrated to minimize the total-traveling distances for multiple nanowires in 2D space. The motion-planning algorithm was built on the network-flow MCMF problem to generate the feasible atomic-cell areas for each nanowire. The algorithm also incorporated the simultaneous motion-control capacity limits. The nanowires' roadmap in the reduced area was then constructed to determine the obstacle-avoiding optimal path. Simulation results demonstrated that the two-stage algorithm

significantly reduces the computational complexity when compared with the state-of-art RRT\* algorithm. Finally, we have also demonstrated the performance of the proposed motion-planning and control schemes with extensive experiments to illustrate the automated manipulation of simultaneous multiple nanowires in a micro-fluidic device.

For efficient manipulation of simultaneous multiple nanowires in liquid suspension, we proposed a time-optimal motion planning algorithm SRRT\*. It took advantages of the sparse RRT structure to generate computationally efficient high-quality paths while maintaining the near-optimal performance. The use of the potential fields in the planning algorithm also helped quickly generate a feasible solution. Simulation and experimental results demonstrated that the SRRT\* algorithm reduces the computational complexity when it compares with the RRT\* algorithm. We demonstrated the experimental performance of the proposed online motion-planning and control scheme to efficiently steer two nanowires simultaneously with 10 times faster than the straight-line trajectories.

The proposed motion control, motion planning, and manipulation of nanowires using electric-fields in fluid suspension serves as an enabling technique of the automated manufacturing of functional nanodevices. In the last part of this dissertation, we integrated automated online characterization, manipulation, and assembly of nanowires to fabricate SiNW based FET nanodevices with selectable electrical conductivities. We extended CS-EOS with the proposed motion control, planning, and manipulation strategies to enable characterizing and manipulating the simultaneous multiple nanowires. These nanowires were then deposited at different locations to form functional nanodevice with different electrical properties. Proof-of-concept SiNW-based thin-film FET devices were assembled by nanowires' electrical conductivities. The measurement results confirmed the effectiveness and feasibility of the integrated characterization, manipulation, and assembly process. The designed scheme provided a foundation for the scalable, automated, and precise manipulating nanowires to build

functional nanodevices, and providing an appealingly simple and effective mean to hold and position microscopic objects.

## 7.2 Future work

As the future extensions of this dissertation, we plan to further develop the “smart” electric tweezers to manipulate nano-particles with the capability to automatically characterize, sort, and position nanowires for micro-/nano-electronics and biomedical applications. With the enabling techniques of precisely and efficiently manipulation of simultaneous multiple nano-particles with independent motions, applications of electric tweezers include nanoelectronics assembly, manufacturing functional nano-devices, nano-neuron interface, bio-sensors, cell characterization and sorting, probing the responses of cells to mechanical and biochemical stimuli, etc. Here we summarize a few on going work to further improve the electric-field based nanomanipulation.

1. On the subject of the micro-/nano-electronics application, we are currently fabricating the SiNW-based FETs with DEP based self-assembly method using the same device design proposed in Section 6.4. More comparison of the characteristics and performance of the assembled SiNW-based FET devices will be evaluated to quantitatively study the pros and cons of the CS-EOS based and DEP based assembly. Improved fabrication process with dry etching technique to reduce the number of lost deposited nanowires in the photolithography process will be conducted. More measurement and testing results of assembling large numbers of simultaneous nanowires will be discussed to further investigate the performance of the integrated automated characterization, manipulation, and assembly scheme.
2. As to the functional nanodevices for biomedical applications, we are working on patterned micro/nano-tubes based axonal guidance, neural circuitry, and neural computing. In order to communicate with the correct targets, neurons send



out axons to follow very precise paths in the nervous system. Axonal guidance concerns the process on how axons manage to find their way so accurately to reach the targets. Microchannels have been used to guide the growth of axons [171, 172]. In [173], microtubules loaded with nerve growth factor (NGF) have been demonstrated to release and deliver drugs to enhance the growth of axons. Lipid tubes filled with NGF have shown a great potential to guide the axon's growth inside the tubes. Therefore, manipulating the position of the tubes could enable the artificial manipulation of the axonal growth. With the nanomanipulation techniques developed in this dissertation, we are working on manipulating connections among target neurons with precisely controlled and patterned micro/nano-tubes to achieve automated axonal guidance and, finally, form desired neural circuitry or rebuild neural system. Figure 7.1 illustrates the schematic of the patterned micro/nano-tubes based axonal guidance. The lipid tubes are manipulated to form desired patterns, and conductive micro/nanowires are used as bio-sensor to detect the action potential propagation. Furthermore, it has been reported that the action potential propagation in myelinated neurons is 100 times faster than in unmyelinated neurons because of saltatory conduction. Therefore, by varying materials of the tubes, we plan to mimic the myelin that surrounds the axon. Those myelin-like tubes could function as electrically insulating layer to increase the speed of the nerve impulse and reduce energy expenditure over the axon membrane. The manipulation of the myelin-like tubes could be an appealing and potential tool to treat and even possibly cure the axonal degeneration diseases, such as ALS.

3. In device and system design aspect, in order to test the large-scale motion planning algorithms, design and fabricate multi-layer electrodes to form large dimensional electrode arrays in the micro-fluidic devices is also an ongoing work.
4. To achieve real-time online replanning for multiple nanowires, we are currently

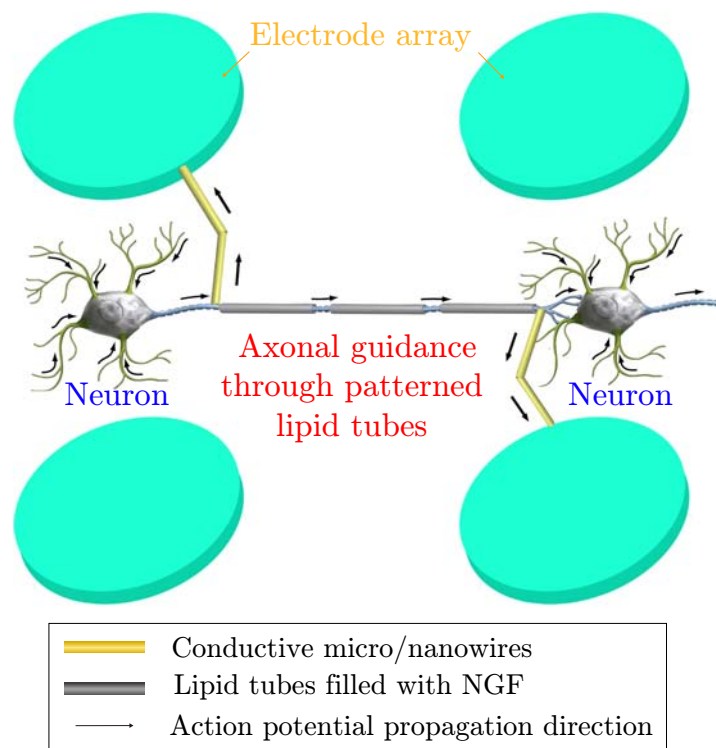


Figure 7.1: Schematic of the patterned micro/nano-tubes based axonal guidance.

working on improving the computational efficiency of the simultaneous multiple-nanowire motion planning algorithms to achieve online replanning coping with large numbers of nanowires. The scheme similar to SST\* in [126] might be adopted to enhance the proposed algorithm for online motion-planning and control. More extensive experiments will be conducted to demonstrate the online motion planning and control of multiple nanowires simultaneously in the future work.

5. Fundamentally, we plan to understand the more precise motion model of particles in various scale and take higher order terms into modeling phase. Since the proposed methods do not limit to actuation, we also intend to extend the techniques to many other bio-compatible actuation, such as magnetic fields to incorporate with the Magnetic Resonance Imaging (MRI) for in vivo scans.

## References

- [1] D. L. Fan, F. Q. Zhu, R. C. Cammarata, and C. L. Chien, “Electric tweezers,” *Nano Today*, vol. 6, pp. 339–354, 2011.
- [2] C. Akin, “Electro-orientation spectroscopy as a facile way to characterize and sort electrical properties of nanowires/nanotubes,” Ph.D. dissertation, Dept. Mech. Aero. Eng., Rutgers University, New Brunswick, NJ, 2016.
- [3] Y. Li, J. X. F. Qian, and C. Lieber, “Nanowire electronic and optoelectronic devices,” *Mater. Today*, vol. 9, pp. 18–27, 2006.
- [4] W. Lu and C. Lieber, “Nanoelectronics from the bottom up,” *Nat. Mater.*, vol. 6, pp. 841–850, 2007.
- [5] J. Hu, T. W. Odom, and C. M. Lieber, “Chemistry and physics in one dimension: synthesis and properties of nanowires and nanotubes,” *Acc. Chem. Res.*, vol. 32, no. 5, pp. 435–445, 1999.
- [6] A. Y. Kasumovand, R. Deblock, M. Kociak, B. Reulet, H. Bouchiat, I. I. Khodosh, Y. B. Gorbatov, V. T. Volkov, C. Journet, and M. Burghard, “Supercurrents through single-walled carbon nanotubes,” *Science*, vol. 284, no. 5419, p. 1508, 1999.
- [7] P. G. Collins and P. Avouris, “Nanotubes for electronics,” *Sci. Amer.*, vol. 283, no. 3, pp. 62–69, 2000.
- [8] Y. Cui and C. M. Lieber, “Functional nanoscale electronic devices assembled using silicon nanowire building blocks,” *Science*, vol. 291, no. 5505, p. 851, 2001.
- [9] X. Duan, Y. Huang, Y. Cui, J. Wang, and C. M. Lieber, “Indium phosphide nanowires as building blocks for nanoscale electronic and optoelectronic devices,” *Nature*, vol. 409, no. 6816, pp. 66–69, 2001.
- [10] Y. Huang and B. Rubinsky, “Microfabricated electroporation chip for single cell membrane permeabilization,” *Sens Actuators A Phys.*, vol. 89, pp. 242–249, 2001.
- [11] P. Jarillo-Herrero, J. A. V. Dam, and L. P. Kouwenhoven, “Quantum supercurrent transistors in carbon nanotubes,” *Nature*, vol. 439, no. 7079, pp. 953–956, 2006.

- [12] M. A. Foster, A. C. Turner, M. Lipson, and A. L. Gaeta, “Nonlinear optics in photonic nanowires,” *Opt. Express*, vol. 16, pp. 1300–1320, 2008.
- [13] M. H. Huang, S. Mao, H. Feick, H. Yan, Y. Wu, H. Kind, E. Weber, R. Russo, and P. Yang, “Room temperature ultraviolet nanowire nanolasers,” *Science*, vol. 292, no. 5523, p. 1897, 2001.
- [14] S. Berber, Y. K. Kwon, and D. Tomanek, “Unusually high thermal conductivity of carbon nanotubes,” *Phy. Rev. Lett.*, vol. 84, p. 4613, 2000.
- [15] P. Kim, L. Shi, A. Majumdar, and P. L. McEuen, “Thermal transport measurements of individual multiwalled nanotubes,” *Phy. Rev. Lett.*, vol. 87, p. 215502, 2001.
- [16] N. Li, J. Hou, and L. Sha, “Design and analysis of an MST-based topology control algorithm,” in *Proc. INFOCOM*, 2003, pp. 1702–1712.
- [17] L. Sun, Y. Hao, C. L. Chien, and P. C. Searson, “Tuning the properties of magnetic nanowires,” *IBM J. Res. Devel*, vol. 49, pp. 79–102, 2005.
- [18] T. M. Whitney, P. C. S. J. S. Jiang, , and C. L. Chien, “Fabrication and magnetic properties of arrays of metallic nanowires,” *Science*, vol. 261, pp. 1316–1319, 1993.
- [19] P. S. E.W. Wong and C. Lieber, “Nanobeam mechanics: elasticity, strength and toughness of nanorods and nanotubes,” *Science*, vol. 277, pp. 1971–1975, 1997.
- [20] J. P. Lu, “Elastic properties of carbon nanotubes and nanoropes,” *Phy. Rev. Lett.*, vol. 79, no. 7, pp. 1297–1300, 1997.
- [21] A. Krishnan, E. Dujardin, T. W. Ebbesen, P. N. Yianilos, and M. M. J. Treacy, “Youngs modulus of single-walled nanotubes,” *Phys. Rev., B*, vol. 58, no. 20, pp. 14 013–14 019, 1998.
- [22] J. P. Salvetat, G. A. D. Briggs, J. M. Bonard, R. R. Bacsá, A. J. Kulik, T. Stockli, N. A. Burnham, and L. Forro, “Elastic and shear moduli of single-walled carbon nanotube ropes,” *Phy. Rev. Lett.*, vol. 82, no. 5, pp. 944–947, 1999.
- [23] J. Y. Huang, S. Chen, Z. Q. Wang, K. Kempa, Y. M. Wang, S. H. Jo, G. Chen, M. S. Dresselhaus, and Z. F. Ren, “Superplastic carbon nanotubes,” *Nature*, vol. 439, no. 7074, p. 281, 2006.
- [24] W. Lu and C. M. Lieber, “Nanoelectronics from the bottom up,” *Nat. Mater.*, vol. 6, no. 11, pp. 841–850, 2007.
- [25] C. Thelander, P. Agarwal, S. Brongersma, J. Eymery, L.-F. Feiner, A. Forchel, M. Scheffler, W. Riess, B. Ohlsson, U. Gösele *et al.*, “Nanowire-based one-dimensional electronics,” *Mater. Today*, vol. 9, no. 10, pp. 28–35, 2006.

- [26] J. Goldberger, A. I. Hochbaum, R. Fan, and P. Yang, "Silicon vertically integrated nanowire field effect transistors," *Nano Lett.*, vol. 6, no. 5, pp. 973–977, 2006.
- [27] Y. Li, F. Qian, J. Xiang, and C. M. Lieber, "Nanowire electronic and optoelectronic devices," *Mater. Today*, vol. 9, no. 10, pp. 18–27, 2006.
- [28] J. Wang, M. S. Gudiksen, X. Duan, Y. Cui, and C. M. Lieber, "Highly polarized photoluminescence and photodetection from single indium phosphide nanowires," *Science*, vol. 293, no. 5534, pp. 1455–1457, 2001.
- [29] R. Yan, D. Gargas, and P. Yang, "Nanowire photonics," *Nat. Photon*, vol. 3, no. 10, pp. 569–576, 2009.
- [30] L.-F. Cui, R. Ruffo, C. K. Chan, H. Peng, and Y. Cui, "Crystalline-amorphous core-shell silicon nanowires for high capacity and high current battery electrodes," *Nano Lett.*, vol. 9, no. 1, pp. 491–495, 2008.
- [31] C. K. Chan, X. F. Zhang, and Y. Cui, "High capacity li ion battery anodes using ge nanowires," *Nano Lett.*, vol. 8, no. 1, pp. 307–309, 2008.
- [32] H. Kim and J. Cho, "Superior lithium electroactive mesoporous si@carbon core-shell nanowires for lithium battery anode material," *Nano Lett.*, vol. 8, no. 11, pp. 3688–3691, 2008.
- [33] M. Law, L. E. Greene, J. C. Johnson, R. Saykally, and P. Yang, "Nanowire dye-sensitized solar cells," *Nat. Mater.*, vol. 4, no. 6, pp. 455–459, 2005.
- [34] J. B. Baxter and E. S. Aydil, "Nanowire-based dye-sensitized solar cells," *Appl. Phys. Lett.*, vol. 86, no. 5, p. 053114, 2005.
- [35] E. C. Garnett, M. L. Brongersma, Y. Cui, and M. D. McGehee, "Nanowire solar cells," *Annu. Rev. Mater. Res.*, vol. 41, pp. 269–295, 2011.
- [36] F. Patolsky and C. M. Lieber, "Nanowire nanosensors," *Mater. Today*, vol. 8, no. 4, pp. 20–28, 2005.
- [37] E. Snow, F. Perkins, E. Houser, S. Badescu, and T. Reinecke, "Chemical detection with a single-walled carbon nanotube capacitor," *Science*, vol. 307, no. 5717, pp. 1942–1945, 2005.
- [38] Y. Cui, Q. Wei, H. Park, and C. M. Lieber, "Nanowire nanosensors for highly sensitive and selective detection of biological and chemical species," *Science*, vol. 293, no. 5533, pp. 1289–1292, 2001.
- [39] F. Patolsky, B. P. Timko, G. Yu, Y. Fang, A. B. Greytak, G. Zheng, and C. M. Lieber, "Detection, stimulation, and inhibition of neuronal signals with high-density nanowire transistor arrays," *Science*, vol. 313, no. 5790, pp. 1100–1104, 2006.

- [40] Y. Huang, X. Duan, Y. Cui, L. J. Lauhon, K.-H. Kim, and C. M. Lieber, “Logic gates and computation from assembled nanowire building blocks,” *Science*, vol. 294, no. 5545, pp. 1313–1317, 2001.
- [41] B. Piccione, C.-H. Cho, L. K. Van Vugt, and R. Agarwal, “All-optical active switching in individual semiconductor nanowires,” *Nat. Nanotechnol.*, vol. 7, no. 10, pp. 640–645, 2012.
- [42] Y. Cui, Z. Zhong, D. Wang, W. U. Wang, and C. M. Lieber, “High performance silicon nanowire field effect transistors,” *Nano Lett.*, vol. 3, no. 2, pp. 149–152, 2003.
- [43] Q. Cao, S.-J. Han, J. Tersoff, A. D. Franklin, Y. Zhu, Z. Zhang, G. S. Tulevski, J. Tang, and W. Haensch, “End-bonded contacts for carbon nanotube transistors with low, size-independent resistance,” *Science*, vol. 350, no. 6256, pp. 68–72, 2015.
- [44] D. Fan, Z. Yi, R. Cheong, F. Q. Zhu, R. C. Cammarata, C. L. Chien, and A. Levchenko, “Subcellular-resolution delivery of a cytokine through precisely manipulated nanowires,” *Nat. Nanotechnol.*, vol. 5, pp. 545–551, 2010.
- [45] K. Kim, X. Xu, J. Guo, and D. Fan, “Ultrahigh-speed rotating nanoelectromechanical system devices assembled from nanoscale building blocks,” *Nature communications*, vol. 5, p. 3632, 2014.
- [46] L. Dong and B. J. Nelson, “Tutorial-robotics in the small part ii: nanorobotics,” *IEEE Robot. Autom. Mag.*, vol. 14, no. 3, pp. 111–121, 2007.
- [47] T. Fukuda, M. Nakajima, M. R. Ahmad, Y. Shen, and M. Kojima, “Micro-and nanomechatronics,” *IEEE Ind. Electron. Mag.*, vol. 4, no. 4, pp. 13–22, 2010.
- [48] P. Iqbal, J. A. Preece, and P. M. Mendes, “Nanotechnology: The “top-down” and “bottom-up” approaches,” *Supramol. Chem.: Mol. Nanomater.*, 2012.
- [49] S. Mazerolle, J.-M. Breguet, A. Steinecker, J. Agnus, R. Perez, J. Michler *et al.*, “Nanomanipulation in a scanning electron microscope,” *J. Mater. Process. Technol.*, vol. 167, no. 2, pp. 371–382, 2005.
- [50] Y. Xia, P. Yang, Y. Sun, Y. Wu, B. Mayers, B. Gates, Y. Yin, F. Kim, and H. Yan, “One-dimensional nanostructures: synthesis, characterization, and applications,” *Advanced Mater.*, vol. 15, no. 5, pp. 353–389, 2003.
- [51] G. M. Whitesides and B. Grzybowski, “Self-assembly at all scales,” *Science*, vol. 295, no. 5564, pp. 2418–2421, 2002.
- [52] Y. Xia, J. A. Rogers, K. E. Paul, and G. M. Whitesides, “Unconventional methods for fabricating and patterning nanostructures,” *Chemical reviews*, vol. 99, no. 7, pp. 1823–1848, 1999.

- [53] M. F. De Volder, S. H. Tawfick, R. H. Baughman, and A. J. Hart, "Carbon nanotubes: present and future commercial applications," *Science*, vol. 339, no. 6119, pp. 535–539, 2013.
- [54] C. Shi, D. K. Luu, Q. Yang, J. Liu, J. Chen, C. Ru, S. Xie, J. Luo, J. Ge, and Y. Sun, "Recent advances in nanorobotic manipulation inside scanning electron microscopes," *Microsystems & Nanoengineering*, vol. 2, 2016.
- [55] A. G. Rinzler, "Materials processing: Sorting out carbon nanotube electronics," *Nat. Nanotech*, vol. 1, no. 1, p. 17, 2006.
- [56] Y. Wang, D. Maspoch, S. Zou, G. C. Schatz, R. E. Smalley, and C. A. Mirkin, "Controlling the shape, orientation, and linkage of carbon nanotube features with nano affinity templates," *Proc. Nat. Acad. Sci.*, vol. 103, no. 7, p. 2026, 2006.
- [57] N. Xi and W. J. Li, "Recent development in nanoscale manipulation and assembly," *IEEE Trans. Automat. Sci. Eng.*, vol. 3, no. 3, pp. 194–198, 2006.
- [58] S. J. Koh, "Strategies for controlled placement of nanoscale building blocks," *Nanoscale Res. Lett.*, vol. 2, no. 11, pp. 519–545, 2007.
- [59] Q. Cao and J. A. Rogers, "Ultrathin films of single-walled carbon nanotubes for electronics and sensors: A review of fundamental and applied aspects," *Adv. Mater.*, vol. 21, no. 1, pp. 29–53, 2009.
- [60] D. Fan, Z. Yin, R. Cheong, F. Q. Zhu, R. C. Cammarata, C. L. Chien, and A. Levchenko, "Subcellular-resolution delivery of a cytokine through precisely manipulated nanowires," *Nat. Nanotech*, vol. 5, pp. 545–551, 2010.
- [61] A. J. Hilmer and M. S. Strano, "Nanobiotechnology: Nanowires have cells in their sights," *Nat. Nanotech*, vol. 5, no. 7, pp. 481–482, 2010.
- [62] L. Dong, F. Arai, and T. Fukuda, "Destructive constructions of nanostructures with carbon nanotubes through nanorobotic manipulation," *IEEE/ASME Trans. Mechatronics*, vol. 9, no. 2, pp. 350–357, 2004.
- [63] T. Fukuda, A. Fumihito, and M. Nakajima, *Micro-Nanorobotic Manipulation Systems and Their Applications*, New York, NY, 2013.
- [64] S. Mekid, S. Bashmal, and H. M. Ouakad, "Nanoscale manipulators: Review of conceptual designs through recent patents," *Recent Pat. Nanotechnol.*, vol. 10, no. 1, pp. 44–58, 2016.
- [65] D. G. Grier, "A revolution in optical manipulation," *Nature*, vol. 424, no. 6950, pp. 810–816, 2003.
- [66] C. Gosse and V. Croquette, "Magnetic tweezers: micromanipulation and force measurement at the molecular level," *Biophys. J.*, vol. 82, no. 6, pp. 3314–3329, 2002.

- [67] A. Bancaud, N. C. e Silva, M. Barbi, G. Wagner, J.-F. Allemand, J. Mozziconacci, C. Lavelle, V. Croquette, J.-M. Victor, A. Prunell *et al.*, “Structural plasticity of single chromatin fibers revealed by torsional manipulation,” *Nat. Struct. Mol. Biol.*, vol. 13, no. 5, pp. 444–450, 2006.
- [68] A. Celedon, I. M. Nodelman, B. Wildt, R. Dewan, P. Searson, D. Wirtz, G. D. Bowman, and S. X. Sun, “Magnetic tweezers measurement of single molecule torque,” *Nano Lett.*, vol. 9, no. 4, pp. 1720–1725, 2009.
- [69] R. Probst, Z. Cummins, C. Ropp, E. Eaks, and B. Shapiro, “Flow control of small objects on chip: Manipulating live cells, quantum dots, and nanowires,” *IEEE Control Syst. Mag.*, vol. 32, no. 2, pp. 26–53, 2012.
- [70] C. Akin, J. Yi, L. C. Feldman, C. Durand, A.-P. Li, M. A. Filler, and J. W. Shan, “Contactless determination of electrical conductivity of one-dimensional nanomaterials by solution-based electro-orientation spectroscopy,” *ACS Nano*, vol. 9, no. 5, pp. 5405–5412, 2015.
- [71] C. Akin, L. C. Feldman, C. Durand, S. M. Hus, A.-P. Li, H. Y. Hui, M. A. Filler, J. Yi, and J. W. Shan., “High-throughput electrical measurement and microfluidic sorting of semiconductor nanowires,” *Lab Chip*, vol. 16, pp. 2126–2134, 2016.
- [72] H. Chen, N. Xi, and G. Li, “CAD-guided automated nanoassembly using atomic force microscopy-based nonrobotics,” *IEEE Trans. Automat. Sci. Eng.*, vol. 3, no. 3, pp. 208–217, 2006.
- [73] X. Ye, Y. Zhang, C. Ru, J. Luo, S. Xie, and Y. Sun, “Automated pick-place of silicon nanowires,” *IEEE Trans. Automat. Sci. Eng.*, vol. 10, no. 3, pp. 554–561, 2013.
- [74] P. R. C. Gascoyne and J. V. Vykoukal, “Dielectrophoresis-based sample handling in general-purpose programmable diagnostic instruments,” *Proc. IEEE*, vol. 92, no. 1, pp. 22–42, 2004.
- [75] R. Hunter, *Foundations of Colloid Science*. Oxford, UK: Oxford University Press, 1989.
- [76] K. Yu, J. Yi, and J. Shan, “Motion control, planning and manipulation of nanowires under electric-fields in fluid suspension,” *IEEE Trans. Automat. Sci. Eng.*, vol. 12, no. 1, pp. 37–49, 2015.
- [77] —, “Simultaneous multiple-nanowire motion control, planning, and manipulation under electric fields in fluid suspension,” *IEEE Trans. Automat. Sci. Eng.*, 2017, in press.
- [78] K. Yu, X. Lu, J. Yi, and J. Shan, “Electrophoresis-based motion planning and control of nanowires in suspended fluids,” in *Proc. IEEE Conf. Automat. Sci. Eng.*, Madison, WI, 2013, pp. 831–836.



- [79] K. Yu, J. Yi, and J. Shan, "Motion control and manipulation of nanowires under electric-fields in fluid suspension," in *Proc. IEEE/ASME Int. Conf. Adv. Intell. Mechatronics*, Besancon, France, 2014, pp. 366–371.
- [80] —, "Motion planning and manipulation of multiple nanowires simultaneously under electric-fields in fluid suspension," in *Proc. IEEE Conf. Automat. Sci. Eng.*, Gothenburg, Sweden, 2015, pp. 489–494.
- [81] —, "Time-optimal simultaneous motion planning and manipulation of multiple nanowires under electric-fields in fluid suspension," in *Proc. IEEE Conf. Automat. Sci. Eng.*, Dallas, TX, 2016, pp. 954–959.
- [82] J. Voldman, "Dielectrophoretic traps for cell manipulation," in *BioMEMS and Biomedical Nanotechnology, Vol IV: Biomolecular Sensing, Processing and Analysis*, R. Bashir, S. Wereley, and M. Ferrari, Eds. New York, NY: Springer, 2006, pp. 159–186.
- [83] R. Pethig, "Review article – Dielectrophoresis: Status of the theory, technology, and applications," *Biomicrofluidics*, vol. 4, 2010, Paper #022811.
- [84] J. Voldman, "Electrical forces for microscale cell manipulation," *Annu. Rev. Biomed. Eng.*, vol. 8, pp. 425–454, 2006.
- [85] C. Yu, J. Vykoukal, D. M. Vykoukal, J. A. Schwartz, L. Shi, and P. R. C. Gascoyne, "A threedimensional dielectrophoretic particle focusing channel for microcytometry applications," *J. Microelectromech. Syst.*, vol. 14, no. 3, pp. 480–487, 2005.
- [86] B. M. Taff and J. Voldman, "A scalable addressable positive-dielectrophoretic cell-sorting array," *Anal. Chem.*, vol. 77, pp. 7976–7983, 2005.
- [87] A. E. Cohen and W. E. Moerner, "Method for trapping and manipulating nanoscale objects in solution," *Appl. Phys. Lett.*, vol. 86, 2005, Paper 093109.
- [88] A. E. Cohen, "Control of nanoparticles with arbitrary two-dimensional force fields," *Phys. Rev. Lett.*, vol. 94, 2005, Paper 118102.
- [89] T. P. Hunt and R. M. Westervelt, "Dielectrophoresis tweezers for single cell manipulation," *Biomed. Microdevices*, vol. 8, pp. 227–230, 2006.
- [90] J. G. Kralj, M. T. W. Lis, M. A. Schmidt, and K. F. Jensen, "Continuous dielectrophoretic size-based particle sorting," *Anal. Chem.*, vol. 78, pp. 5019–5025, 2006.
- [91] L. Wang, L. Flanagan, and A. P. Lee, "Side-wall vertical electrodes for lateral field microfluidic applications," *J. Microelectromech. Syst.*, vol. 16, no. 2, pp. 454–461, 2007.

- [92] S.-W. Lee, H. Li, and R. Bashir, “Dielectrophoretic tweezers for examining particle-surface interactions within microfluidic devices,” *Appl. Phys. Lett.*, vol. 90, 2007, Paper 223902.
- [93] C. H. Kua, Y. C. Lam, I. Rodriguez, C. Yang, and K. Youcef-Toumi, “Cell motion model for moving dielectrophoresis,” *Anal. Chem.*, vol. 80, pp. 5454–5461, 2008.
- [94] L. Wang, J. Lu, S. A. Monuki, L. Flanagan, and A. P. Lee, “Dual frequency dielectrophoresis with interdigitated sidewall electrodes for microfluidic flow-through separation of beads and cells,” *Ecolog. Psychol.*, vol. 30, pp. 782–791, 2009.
- [95] H. Cui, J. Voldman, X. He, and K. Lim, “Separation of particles by pulsed dielectrophoresis,” *Lab Chip*, vol. 9, no. 16, pp. 2306–2312, 2009.
- [96] S. P. Desai, M. D. Vahey, and J. Voldman, “Electrically addressable vesicles: Tools for dielectrophoresis metrology,” *Langmuir*, vol. 25, pp. 3867–3875, 2009.
- [97] D. L. Fan, F. Q. Zhu, R. C. Cammarata, and C. L. Chien, “Manipulation of nanowires in suspension by ac electric fields,” *Appl. Phys. Lett.*, vol. 85, no. 18, pp. 4175–4177, 2004.
- [98] ———, “Controllable high-speed rotation of nanowires,” *Phy. Rev. Lett.*, vol. 94, 2005, Paper 247208.
- [99] B. Edwards, N. Engheta, and S. Evoy, “Theory of simultaneous control of orientation and translational motion of nanorods using positive dielectrophoretic forces,” *J. Appl. Phys.*, vol. 98, 2007, Paper 124314.
- [100] D. L. Fan, F. Q. Zhu, R. C. Cammarata, and C. L. Chien, “Efficiency of assembling of nanowires in suspension by ac electric fields,” *Appl. Phys. Lett.*, vol. 89, 2006, Paper 223115.
- [101] B. Edwards, T. S. Mayer, and R. B. Bhiladvala, “Synchronous electrorotation of nanowires in fluid,” *Nano Lett.*, vol. 6, no. 4, pp. 626–632, 2006.
- [102] B. Edwards, N. Engheta, and S. Evoy, “Electric tweezers: Experimental study of positive dielectrophoresis-based positioning and orientation of a nanorod,” *J. Appl. Phys.*, vol. 102, 2007, Paper 024913.
- [103] D. L. Fan, R. C. Cammarata, and C. L. Chien, “Precision transport and assembling of nanowires in suspension by electric fields,” *Appl. Phys. Lett.*, vol. 92, 2008, Paper 093115.
- [104] S. Kumar, Z. Peng, H. Shin, Z. L. Wang, and P. J. Hesketh, “AC dielectrophoresis of Tin oxide nanobelts suspended in ethanol: Manipulation and visualization,” *Anal. Chem.*, vol. 82, pp. 2204–2212, 2010.

- [105] P. D. Mathai, P. T. Carmichael, B. A. Shapiro, and J. A. Liddle, “Simultaneous positioning and orientation of single nano-wires using flow control,” *RSC Adv.*, vol. 3, pp. 2677–2682, 2013.
- [106] S. Chaudhary and B. Shapiro, “Arbitrary steering of multiple particles independently in an electro-osmotically driven microfluidic system,” *IEEE Trans. Contr. Syst. Technol.*, vol. 14, no. 4, pp. 669–680, 2006.
- [107] S. LaValle, *Planning Algorithms*. New York, NY: Cambridge University Press, 2006, also available at <http://planning.cs.uiuc.edu/>.
- [108] E. J. Griffith, S. Akella, and M. K. Goldberg, “Performance characterization of a reconfigurable planar-array digital microfluidic system,” *IEEE Trans. Comput.-Aided Design Integr. Circuits Syst.*, vol. 25, no. 2, pp. 345–357, 2006.
- [109] K. F. Böhringer, “Modeling and controlling parallel tasks in droplet-based microfluidic systems,” *IEEE Trans. Comput.-Aided Design Integr. Circuits Syst.*, vol. 25, no. 2, pp. 334–344, 2006.
- [110] P.-H. Yuh, C.-L. Yang, and Y.-W. Chang, “BioRoute: A network-flow-based routing algorithm for the synthesis of digital microfluidic biochips,” *IEEE Trans. Comput.-Aided Design Integr. Circuits Syst.*, vol. 27, no. 11, pp. 1928–1941, 2008.
- [111] T. Xu, K. Chalrabarty, and V. K. Pamula, “Defect-tolerant design and optimization of a digital microfluidic biochip for protein crystallization,” *IEEE Trans. Comput.-Aided Design Integr. Circuits Syst.*, vol. 29, no. 4, pp. 552–565, 2010.
- [112] M. Peasgood, C. M. Clark, and J. McPhee, “A complete and scalable strategy for coordinating multiple robots within roadmaps,” *IEEE Trans. Robotics*, vol. 24, no. 2, pp. 283–292, 2008.
- [113] A. A. Furtuna, “Minimum time kinematic trajectories for self-propelled rigid bodies in the unobstructed plane,” Ph.D. dissertation, Dept. Comp. Sci., Dartmouth College, Hanover, NH, 2011.
- [114] J. Peng and S. Akella, “Coordinating multiple robots with kinodynamic constraints along specific paths,” *Int. J. Robot. Res.*, vol. 24, no. 4, pp. 295–310, 2005.
- [115] S. Akella and S. Hutchinson, “Coordinating the motions of multiple robots with specified trajectories,” in *Proc. IEEE Int. Conf. Robot. Autom.*, 2002, pp. 624–631.
- [116] J. Yu and S. M. LaValle, “Multi-agent path planning and network flow,” in *Algorithmic Foundations of Robotics X*, 2013, pp. 157–173.
- [117] J. Yu and S. LaValle, “Planning optimal paths for multiple robots on graphs,” in *Proc. IEEE Int. Conf. Robot. Autom.*, 2013, pp. 3612–3617.

- [118] J. Canny, A. Rege, and J. Reif, “An exact algorithm for kinodynamic planning in the plane,” *Discr. Comput. Geometry*, vol. 6, pp. 461–484, 1991.
- [119] D. E. Chang, N. Petit, and P. Rouchon, “Time-optimal control of a particle in a dielectrophoretic system,” *IEEE Trans. Automat. Contr.*, vol. 51, no. 7, pp. 1100–1114, 2006.
- [120] H. Simha, R. N. Banavar, and D. E. Chang, “Aspects of time-optimal control of a particle in a dielectrophoretic system,” in *Proc. IEEE Conf. Decision Control and European Control Conf.*, Dec 2011, pp. 278–283.
- [121] J. Barraquand and J. C. Latombe, “Nonholonomic multibody mobile robots: controllability and motion planning in the presence of obstacles,” *Algorithmica*, vol. 10, no. 2-4, pp. 121–155, 1993.
- [122] T. Ju, S. Liu, J. Yang, and D. Sun, “Rapidly exploring random tree algorithm-based path planning for robot-aided optical manipulation of biological cells,” *IEEE Trans. Automat. Sci. Eng.*, vol. 11, no. 3, pp. 649–657, 2014.
- [123] S. Karaman and E. Frazzoli, “Sampling-based algorithms for optimal motion planning,” *Int. J. Robot. Res.*, vol. 30, no. 7, pp. 846–894, 2011.
- [124] A. Dobson and K. E. Bekris, “Sparse roadmap spanners for asymptotically near-optimal motion planning,” *Int. J. Robot. Res.*, vol. 33, no. 1, pp. 18–47, 2014.
- [125] R. Tedrake, “LQR-trees: Feedback motion planning on sparse randomized trees,” in *Proc. Robotics: Sci. Syst.*, Seattle, USA, June 2009.
- [126] Y. Li, Z. Littlefield, and K. E. Bekris, “Asymptotically optimal sampling-based kinodynamic planning,” *Int. J. Robot. Res.*, 2016, in press.
- [127] P. Y. Li and R. Horowitz, “Passive velocity field control (PVFC): Part II – Application to contour following,” *IEEE Trans. Automat. Contr.*, vol. 46, no. 9, pp. 1360–1371, 2001.
- [128] Y. Zhang and J. Yi, “Velocity field-based maneuver regulation of autonomous motorcycles,” in *Proc. IFAC Symp. Mechatronic Syst.*, Cambridge, MA, 2010, pp. 385–392.
- [129] J. Happel and H. Brenner, *Low Reynolds Number Hydrodynamics*. Hague, Netherlands: Martinus Nijhoff Publishers, 1983.
- [130] F. M. Zimmermann and J. W. Shan, “Rotational friction constant of single-wall carbon nanotubes in liquid suspension,” *Appl. Phys. Lett.*, vol. 94, p. 053107, 2009.
- [131] R. G. Larson, *The Structure and Rheology of Complex Fluids*. Oxford, UK: Oxford University Press, 1999.

- [132] R. J. Castellano, C. Akin, G. Giraldo, S. Kim, F. Fornasiero, and J. W. Shan, "Electrokinetics of scalable, electric-field-assisted fabrication of vertically aligned carbon-nanotube/polymer composites," *J. Appl. Phys.*, vol. 117, no. 21, p. 214306, 2015.
- [133] Y. Solomentsev and J. L. Anderson, "Electrophoretic transport of spheroidal colloids in nonhomogeneous electric fields," *Ind. & Eng. Chem. Res.*, vol. 34, no. 10, pp. 3231–3238, 1995.
- [134] M. Tanelli, M. Corno, and S. Saveresi, *Modelling, Simulation and Control of Two-wheeled Vehicles*, New York, NY, 2014.
- [135] G. Wagner and H. Choset, "M\*: A complete multirobot path planning algorithm with performance bounds," in *Proc. IEEE/RSJ Int. Conf. Intell. Robot. Syst.*, San Francisco, CA, USA, 2011, pp. 3260–3267.
- [136] P. Šůcha, M. Kutil, M. Sojka, and Z. Hanzálek, "Torsche scheduling toolbox for matlab," in *IEEE Comp. Aided Control Syst. Design Symp.*, Munich, Germany, 2006, pp. 1181–1186.
- [137] "GNU Linear Programming Kit, Version 4.6," <http://www.gnu.org/software/glpk/glpk.html>.
- [138] J. D. Gammell, S. S. Srinivasa, and T. D. Barfoot, "Informed rrt\*: Optimal sampling-based path planning focused via direct sampling of an admissible ellipsoidal heuristic," in *Proc. IEEE/RSJ Int. Conf. Intell. Robot. Syst.*, Chicago, IL, 2014, pp. 2997–3004.
- [139] M. Constantinou, G. P. Rigas, F. A. Castro, V. Stolojan, K. F. Hoettges, M. P. Hughes, E. Adkins, B. A. Korgel, and M. Shkunov, "Simultaneous tunable selection and self-assembly of si nanowires from heterogeneous feedstock," *ACS Nano*, vol. 10, no. 4, pp. 4384–4394, 2016.
- [140] Y. Sun, H. Yu, N. Singh, K. Leong, E. Gnani, G. Bacarani, G. Lo, and D. Kwong, "Vertical-si-nanowire-based nonvolatile memory devices with improved performance and reduced process complexity," *IEEE Trans. Electron Devices*, vol. 58, no. 5, pp. 1329–1335, 2011.
- [141] M. Constantinou, K. F. Hoettges, S. Krylyuk, M. B. Katz, A. Davydov, G. P. Rigas, V. Stolojan, M. P. Hughes, and M. Shkunov, "Rapid determination of nanowires electrical properties using a dielectrophoresis-well based system," *Appl. Phys. Lett.*, vol. 110, no. 13, p. 133103, 2017.
- [142] S. Rosenblatt, Y. Yaish, J. Park, J. Gore, V. Sazonova, and P. L. McEuen, "High performance electrolyte gated carbon nanotube transistors," *Nano Lett.*, vol. 2, no. 8, pp. 869–872, 2002.
- [143] D. R. Khanal and J. Wu, "Gate coupling and charge distribution in nanowire field effect transistors," *Nano Lett.*, vol. 7, no. 9, pp. 2778–2783, 2007.

- [144] H. Zhu, Q. Li, H. Yuan, H. Baumgart, D. E. Ioannou, and C. A. Richter, "Self-aligned multi-channel silicon nanowire field-effect transistors," *Solid State Electron.*, vol. 78, pp. 92–96, 2012.
- [145] W. Sant, M. Pourciel-Gouzy, J. Launay, T. D. Conto, R. Colin, A. Martinez, and P. Temple-Boyer, "Development of a creatinine-sensitive sensor for medical analysis," *Sens. Actuators B Chem.*, vol. 103, no. 1C2, pp. 260 – 264, 2004.
- [146] A. Soldatkin, J. Montoriol, W. Sant, C. Martelet, and N. Jaffrezic-Renault, "A novel urea sensitive biosensor with extended dynamic range based on recombinant urease and {ISFETs}," *Biosens. Bioelectron.*, vol. 19, no. 2, pp. 131 – 135, 2003.
- [147] M. J. Schoning and A. Poghossian, "Recent advances in biologically sensitive field-effect transistors (biofets)," *Analyst*, vol. 127, pp. 1137–1151, 2002.
- [148] X. Duan, C. Niu, V. Sahi, J. Chen, J. W. Parce, S. Empedocles, and J. L. Goldman, "High-performance thin-film transistors using semiconductor nanowires and nanoribbons," *Nature*, vol. 425, no. 6955, pp. 274–278, 2003.
- [149] E. N. Dattoli, Q. Wan, W. Guo, Y. Chen, X. Pan, and W. Lu, "Fully transparent thin-film transistor devices based on  $\text{SnO}_2$  nanowires," *Nano Lett.*, vol. 7, no. 8, pp. 2463–2469, 2007.
- [150] Q. Cao, M. Xia, C. Kocabas, M. Shim, J. A. Rogers, and S. V. Rotkin, "Gate capacitance coupling of singled-walled carbon nanotube thin-film transistors," *Appl. Phys. Lett.*, vol. 90, no. 2, p. 023516, 2007.
- [151] R. S. Friedman, M. C. McAlpine, D. S. Ricketts, D. Ham, and C. M. Lieber, "Nanotechnology: High-speed integrated nanowire circuits," *Nature*, vol. 434, no. 7037, pp. 1085–1085, 2005.
- [152] I. Tsydel, T. Marszalek, J. Ulanski, A. Nosal, and M. Gazicki-Lipman, "Applications of parylene films in the manufacture of organic field-effect transistors," *Surf. Coat. Technol.*, vol. 290, pp. 21–27, 2016.
- [153] Y. Kubozono, S. Haas, W. L. Kalb, P. Joris, F. Meng, A. Fujiwara, and B. Batlogg, "High-performance  $\text{p-Si}$  thin-film field-effect transistors with parylene gate insulator," *Appl. Phys. Lett.*, vol. 93, no. 3, p. 272, 2008.
- [154] S. Selvarasah, X. Li, A. Busnaina, and M. R. Dokmeci, "Parylene-c passivated carbon nanotube flexible transistors," *Appl. Phys. Lett.*, vol. 97, no. 15, p. 153120, 2010.
- [155] C. Hassler, R. P. von Metzen, P. Ruther, and T. Stieglitz, "Characterization of parylene c as an encapsulation material for implanted neural prostheses," *J. Biomed. Mater. Res. Part B Appl. Biomater.*, vol. 93, no. 1, pp. 266–274, 2010.

- [156] X. Duan, “Nanowire thin-film transistors: a new avenue to high-performance macroelectronics,” *IEEE Trans. Electron Dev.*, vol. 55, no. 11, pp. 3056–3062, 2008.
- [157] D. H. Shin, J.-E. Kim, H. C. Shim, J.-W. Song, J.-H. Yoon, J. Kim, S. Jeong, J. Kang, S. Baik, and C.-S. Han, “Continuous extraction of highly pure metallic single-walled carbon nanotubes in a microfluidic channel,” *Nano Lett.*, vol. 8, no. 12, pp. 4380–4385, 2008.
- [158] M. Constantinou, G. P. Rigas, F. A. Castro, V. Stolojan, K. F. Hoettges, M. P. Hughes, E. Adkins, B. A. Korgel, and M. Shkunov, “Simultaneous tunable selection and self-assembly of si nanowires from heterogeneous feedstock,” *ACS nano*, vol. 10, no. 4, pp. 4384–4394, 2016.
- [159] W. Gu, H. Choi, and K. Kim, “Universal approach to accurate resistivity measurement for a single nanowire: Theory and application,” *Appl. Phys. Lett.*, vol. 89, no. 25, p. 253102, 2006.
- [160] T.-H. Kim, Z. Wang, J. F. Wendelken, H. H. Weitering, W. Li, and A.-P. Li, “A cryogenic quadrupole scanning tunneling microscope system with fabrication capability for nanotransport research,” *Rev. Sci. Instrum.*, vol. 78, no. 12, p. 123701, 2007.
- [161] D. E. Perea, J. E. Allen, S. J. May, B. W. Wessels, D. N. Seidman, and L. J. Lauhon, “Three-dimensional nanoscale composition mapping of semiconductor nanowires,” *Nano Lett.*, vol. 6, no. 2, pp. 181–185, 2006.
- [162] D. E. Perea, E. R. Hemesath, E. J. Schwalbach, J. L. Lensch-Falk, P. W. Voorhees, and L. J. Lauhon, “Direct measurement of dopant distribution in an individual vapour–liquid–solid nanowire,” *Nat. Nanotechnol.*, vol. 4, no. 5, pp. 315–319, 2009.
- [163] M. McCartney, M. Gribelyuk, J. Li, P. Ronsheim, J. McMurray, and D. J. Smith, “Quantitative analysis of one-dimensional dopant profile by electron holography,” *Appl. Phys. Lett.*, vol. 80, no. 17, pp. 3213–3215, 2002.
- [164] I. Amit, U. Givan, J. G. Connell, D. F. Paul, J. S. Hammond, L. J. Lauhon, and Y. Rosenwaks, “Spatially resolved correlation of active and total doping concentrations in vls grown nanowires,” *Nano Lett.*, vol. 13, no. 6, pp. 2598–2604, 2013.
- [165] E. Koren, Y. Rosenwaks, J. Allen, E. Hemesath, and L. Lauhon, “Nonuniform doping distribution along silicon nanowires measured by kelvin probe force microscopy and scanning photocurrent microscopy,” *Appl. Phys. Lett.*, vol. 95, no. 9, p. 092105, 2009.
- [166] J. E. Allen, D. E. Perea, E. R. Hemesath, and L. J. Lauhon, “Nonuniform nanowire doping profiles revealed by quantitative scanning photocurrent microscopy,” *Adv. Mater.*, vol. 21, no. 30, pp. 3067–3072, 2009.

- [167] R. Krupke, F. Hennrich, H. v. Löhneysen, and M. M. Kappes, “Separation of metallic from semiconducting single-walled carbon nanotubes,” *Science*, vol. 301, no. 5631, pp. 344–347, 2003.
- [168] T. B. Jones, *Electromechanics of Particles*. Cambridge, UK: Cambridge University Press, 2005.
- [169] S. M. Sze and K. K. Ng, *Physics of semiconductor devices*. John Wiley & sons, 2006.
- [170] O. Wunnicke, “Gate capacitance of back-gated nanowire field-effect transistors,” *Appl. Phys. Lett.*, vol. 89, no. 8, Paper 083102.
- [171] J. Park, H. Koito, J. Li, and A. Han, “Microfluidic compartmentalized co-culture platform for cns axon myelination research,” *Biomed. Microdevices*, vol. 11, no. 6, p. 1145, 2009.
- [172] J. Park, S. Kim, S. I. Park, Y. Choe, J. Li, and A. Han, “A microchip for quantitative analysis of cns axon growth under localized biomolecular treatments,” *J. Neurosci. Methods*, vol. 221, pp. 166–174, 2014.
- [173] N. J. Meilander, X. Yu, N. P. Ziats, and R. V. Bellamkonda, “Lipid-based microtubular drug delivery vehicles,” *J. Control. Release*, vol. 71, no. 1, pp. 141–152, 2001.